Calcium-permeable AMPA receptors in layer 5 interneurons of the mouse visual cortex

Julia Vanessa Oyrer

Department of Neuroscience, Physiology and Pharmacology

University College London

December 2014

This thesis is submitted for the degree of Doctor of Philosophy

Abstract

Cortical sensory processing is widely studied in the visual cortex. Such processing depends on specific neuronal connectivity, and the reliable activation of inhibitory interneurons. Excitatory connections onto both excitatory and inhibitory neurons exhibit synaptic plasticity thought to underlie circuit refinement and function. The mechanisms of induction and expression of short- and long-term plasticity can differ between neurons and depend on synapse-specific differences in molecular machinery. Compared to synapses onto principal cells, less is known about plasticity at synapses onto inhibitory neurons. In part, this reflects difficulties of classifying these diverse cells. Mechanistically, postsynaptic N-methyl-D-aspartate-type glutamate receptors are necessary for most forms of plasticity. However, in the hippocampus, postsynaptic amino-3-hydroxy-5-methyl-4-isoxazole propionic acid-type glutamate receptors (AMPARs) of the calcium-permeable (CP-) subtype are thought to underlie a form of non-Hebbian plasticity. I sought to examine the expression of CP-AMPARs at synapses onto the two major classes of inhibitory interneuron in layer 5 of the mouse visual cortex, Basket cells (BCs) and Martinotti cells (MCs). I made patch-clamp recordings from cells in acute brain slices from wild-type and transgenic animals. Interneurons were distinguished using laser scanning two-photon microscopy to characterize their defining patterns of axonal arborisation, and voltage recording to determine their characteristic firing properties. To examine synaptic AMPARs, I recorded miniature excitatory postsynaptic currents, determined their kinetic properties, their rectification due to voltage-dependent block by intracellular polyamines, and their sensitivity to the selective blocker of CP-AMPARs, 1-naphthyl acetyl spermine. I also used antibody labelling to examine the presence of the GluA2 subunit in the two interneuron classes. Although MCs proved less amenable to voltage-clamp recording than did BCs, my findings indicate the presence of CP-AMPARs in BCs but not in MCs, suggesting distinct activation of these two inhibitory inputs to Pyramidal cells. I conclude by discussing the likely influence of differential CP-AMPAR expression on the dynamics of the cortical network.

Declaration

I, Julia Vanessa Oyrer, confirm that the work presented in this thesis is my own. Where information has been derived from other sources, I confirm that this has been indicated in the thesis.

Signed:

December 15, 2014

Acknowledgements

I would like to express my sincere gratitude to Professor Mark Farrant for his commitment, patience and encouragement throughout my PhD training.

I am also indebted to Dr Jesper Sjöström for accepting me into his lab and for the continued support he has provided from Montreal.

I would like to thank the members of the Cull-Candy and Farrant laboratory and the Sjöström laboratory who offered invaluable advice and generous assistance. In particular I would like to thank Professor Stuart Cull-Candy, Dr Marzieh Zonouzi, Dr Cécile Bats, Dr Andrew Macaskill, Dr Rebecca Jones, Dr Ian Coombs, Dr Tommy McGee, Dr Valentina Pendolino, Dr Massimiliano Renzi, Dr Mark Rigby, Dr Steve Sullivan, Karolina Krol, Sarah Pearce and Dorota Studniarczyk in London, and Dr Alexandre Moreau, Dr Dale Elgar, Dr Kate Buchanan, Dr Therese Abrahamsson, Dr Rui Costa, Andrew Chung, Elvis Cela, Erica Gregor, Arne Blackman and Txomin Lalanne in London and Montreal, who have all played a significant role in my training.

Beyond the lab, I would like to thank Professor Thomas Mrsic-Flogel, Dr Sonja Hofer, Professor Alasdair Gibb, Dr Paola Pedarzani, Dr Gilad Silberberg and all the members of the Mrsic-Flogel lab for the care they offered throughout my PhD.

Finally I would like to thank my parents Rudolf and Lieselotte Oyrer, my family and Tim Sissons for their unconditional support.

My PhD was funded by a UCL Impact Studentship.

Contents

List of Figures

List of Tables

Chapter 1

Introduction

Motivation

The nature of signalling at different synapses supports the specific function of the microcircuit in which the synapses participate and thus the information processing of the circuit as a whole. Accordingly, it is important to understand the differences between synapses that influence their function. In this thesis I describe experiments designed to address the expression of AMPA-type glutamate receptors – specifically CP-AMPARs – at excitatory synapses onto the two major classes of inhibitory interneurons (INs) in layer 5 of the mouse visual cortex, Basket cells (BCs) and Martinotti cells (MCs).

The visual cortex is widely studied as a model of sensory processing. As with other brain regions, its function depends on its specific neuronal connectivity, the balance of excitation and inhibition, and thus the appropriate recruitment of INs. Importantly, excitatory connections onto both excitatory and inhibitory neurons exhibit synaptic plasticity – short- or long-term changes in the efficacy of transmission which greatly influence the function of the circuit. The mechanisms by which plasticity is both induced and expressed differ between neurons and synapses, and depend on differences in the molecular machinery of the synapse. Compared to synapses onto principal cells (pyramidal cells; PCs), less is known about plasticity at synapses onto INs. In part, this reflects the difficulties in classifying these diverse cells. Mechanistically, postsynaptic *N*-methyl-D-aspartate-type glutamate receptors (NMDARs) are necessary for

most forms of long-term plasticity. However, in the hippocampus, postsynaptic AMPARs of the calcium-permeable subtype are thought to underlie a form of non-Hebbian plasticity.

In following chapters I describe experiments in which I made patch-clamp recordings from cells in acute brain slices from wild-type and transgenic mice. To distinguish INs, I used laser scanning two-photon microscopy to characterize their defining patterns of axonal arborisation, and voltage recording to determine their characteristic firing properties. To examine synaptic AMPARs, I recorded miniature excitatory postsynaptic currents (mEPSCs), determined their kinetic properties, their rectification due to voltage-dependent block by intracellular spermine, and their sensitivity to the selective blocker of CP-AMPARs, 1-naphthyl acetyl spermine (Naspm). I also used antibody labelling to examine the presence of the GluA2 subunit in the two IN classes. In this chapter, after a general introduction to synaptic transmission, I introduce the visual cortex, its function, its microcircuits and the role of INs and plasticity at their excitatory inputs, before discussing the distinction between AMPAR subtypes.

1.1 Chemical synaptic transmission

The central nervous systems of vertebrates contain billions of electrically excitable cells organised in interconnected networks. Communication between these neurons underlies the normal functioning of the nervous system. Although neurons may be connected electrically, via gap junctions (Fukuda and Kosaka, 2000; Galarreta and Hestrin, 1999; MacVicar and Dudek, 1980), most fast information transfer between them is mediated chemically by the release of neurotransmitters at specialised contacts termed ‘synapses’. This term was first employed by the physiologist Charles Sherrington, when he proposed that if neurons were independent elements, as described by Santiago Ramón y Cajal, then information must be passed between them at ‘junctions’ (see Bennett, 1999).

Chemical synapses consist of a presynaptic element packed with neurotransmitter-containing vesicles, some of which are located immediately adjacent to the presynap-

tic membrane. When an action potential invades this presynaptic bouton, the depolarization causes voltage-gated Ca^{2+} channels to open briefly, resulting in a rapid and short-lived rise in the local Ca^{2+} concentration. The binding of Ca^{2+} to a Ca^{2+} sensor induces the fusion of synaptic vesicles with the presynaptic plasma membrane. At most synapses, vesicles fuse after a delay of less than a millisecond, producing a synchronous release of neurotransmitter (Kaeser and Regehr, 2014; Kochubey et al., 2011).

The neurotransmitter is released into the synaptic cleft between the pre- and postsynaptic membrane specialisations. As the release event and the subsequent diffusion of the neurotransmitter are both rapid, the neurotransmitter time course in the synaptic cleft is typically very brief (<<1 ms) (Barberis et al., 2011; Clements, 1996; Overstreet et al., 2002; Rusakov et al., 2011). In the case of rapid synaptic communication (mediated by neurotransmitters such as glutamate, GABA, glycine, acetylcholine and 5-hydroxytryptamine), the receptors clustered in the postsynaptic membrane are ligand-gated ion channels (Smart and Paoletti, 2012). The brief pulse of neurotransmitter activates these receptors and causes a transient increase in the conductance of the postsynaptic membrane, generating current flow. The postsynaptic currents typically have a very rapid rising phase and a slower multi-exponential decay that reflects receptor deactivation following the removal of the neurotransmitter (Farrant and Kaila, 2007; Jonas and Spruston, 1994).

1.2 Excitatory and inhibitory signalling

The flow of current that results from the change in postsynaptic conductance is determined by the relative values of the membrane potential (V_{m}) and the net equilibrium potential of the ionic species that permeate the synaptic ion channels (E_{syn}). The synaptic current (I_{syn}) is given by $I_{\mathrm{syn}} = g_{\mathrm{syn}}(t)[V_{\mathrm{m}}–E_{\mathrm{syn}}]$ where g_{syn} is the time varying synaptic conductance. The difference between the resting membrane potential and the reversal potential of the synaptic current (E_{syn}) is the 'driving force' and can have either a positive or a negative sign.

Postsynaptic currents are described as being either excitatory or inhibitory. Excitatory

postsynaptic currents (EPSCs) result in the postsynaptic membrane becoming more electrically positive (depolarised) and underlie excitatory postsynaptic potentials (EPSPs) that increase the probability of action potential firing. Inhibitory postsynaptic currents (IPSCs) cause the postsynaptic cell to become more negative (hyperpolarised) and underlie inhibitory postsynaptic potentials (IPSPs) that decrease the probability of an action potential. EPSPs and IPSPs outlast the conductance changes and decay with durations that are determined largely by the membrane time constant, τ_m (Hille, 2001). Receptors that allow the entry of sodium and/or calcium ions are excitatory and produce a depolarization of the postsynaptic membrane, whereas receptors that increase chloride or potassium conductance are typically inhibitory and produce a hyperpolarization. This simple description ignores the issue of shunting, where the conductance itself reduces the depolarization produced by an excitatory current, and the subtleties that arise from temporal and spatial interactions between synaptic events (Gulledge and Stuart, 2003).

The amino acids glutamate and GABA (γ-aminobutyric acid) are ubiquitous in the central nervous system (CNS) and mediate fast excitatory and inhibitory signalling, respectively. Thus, the predominant mechanism for fast excitatory synaptic transmission in the mammalian CNS is the depolarisation of the postsynaptic membrane brought about by the activation of various classes of ionotropic glutamate receptors (iGluRs) (see section 1.3) (Traynelis et al., 2010). These receptors gate channels that produce mixed cation conductances, with reversal potentials of ~0 mV. Activation of excitatory synaptic conductances will move the postsynaptic membrane potential towards and above spike threshold, triggering action potentials. Conversely, GABA-mediated inhibitory synaptic transmission involves the activation of mixed chloride and bicarbonate conductances that often reverse at membrane potentials more hyperpolarised than resting membrane potential and generally at potentials more hyperpolarised than spike threshold. Thus, activation of inhibitory synapses reduces the likelihood of action potential generation.

This thesis is concerned with AMPARs in neocortical INs. Before discussing cortical circuitry, IN diversity and the potential role of different AMPAR subtypes in IN recruitment, I first describe ionotropic glutamate receptors.

1.3 Ionotropic glutamate receptors

Glutamate activates three main classes of iGluRs named after their selective agonists NMDA, AMPA, and kainate (Smart and Paoletti, 2012); in addition glutamate also activates metabotropic (G-protein coupled) receptors. Finally, a group of orphan subunits with sequence similarity to iGluRs, the δ receptors, exist but no glutamate binding has been identified (Ady et al., 2014; Kakegawa et al., 2007). At most glutamatergic synapses the EPSC is carried by AMPA- and NMDA receptors, mediating the fast- (ms) and slow-components (100s ms), respectively (Silver et al., 1992; Spruston et al., 1995), while kainate receptors, although found at some synapses, have a more modulatory role in the regulation of neurotransmitter release (Contractor et al., 2011; Lerma, 2006; Smart and Paoletti, 2012).

At glutamatergic synapses the presence of NMDA, AMPA or kainate receptors can be determined through the use of selective antagonists, specifically the use of the selective NMDA receptor antagonist D-(-)-2-amino-5-phosphonopentanoic acid (D-AP5), the AMPA-/kainate receptor competitive antagonists 6-cyano-/-7-nitroquinoxaline-/-2,3-/-dione (CNQX) and 2,3-diox-6-nitro-1,2,3,4-/-terahydrobenzo[f]quinox/-aline-7-sulphonamide (NBQX), or the more selective non-competitive AMPA receptor antagonist 1-(4-aminophenyl)-3-methylcarbamyl-4-methyl-3,4-dihydro-7,8-methylenedioxy-5H-2,3-benzodiazepine hydrochloride (GYKI 53655) (Contractor et al., 2011; Traynelis et al., 2010).

1.3.1 Genes and subunit composition

The mammalian iGluR family is formed from 18 genes that encode subunit proteins that coassemble to form tetrameric ligand-gated ion channels (Traynelis et al., 2010). The subunits are grouped according to their sequence homology: there are four AMPAR subunits (GluA1-4, also known as GluR1-4), seven NMDAR subunits (GluN1; GluN2A-D; GluN3A-B), five kainate receptor subunits (GluK1-5, also known as GluR5-7) and two δ subunits (GluD1-2), each arising from their corresponding genes *GRIA1-4*, *GRIN1, GRIN2A-D, GRIN3A-B, GRIK1-5A* and *GRID1-2*). Gener-

ally, functional iGluRs are formed only from subunits of the same family, either as homomers (identical subunits) or heteromers (combination of different subunits) (Jonas and Burnashev, 1995; Traynelis et al., 2010). iGluRs are formed in the endoplasmic reticulum (ER) by a dimer of iGluR subunits pairing up with another dimer to form the typical dimer-of-dimers structure (Ayalon and Stern-Bach, 2001).

All iGluR subunits have a broadly similar structure, with four modular domains: the extracellular amino-terminal domain (ATD; also known as the N-terminal domain or NTD), the extracellular ligand-biniding domain (LBD), the transmembrane domain (TMD; with four hydrophobic regions M1-4, of which M1, M3 and M4 are membrane spanning helices and M2 forms a re-entrant loop) and the intracellular carboxyl-terminal domain (CTD) (Meyerson et al., 2014; Sobolevsky et al., 2009). Together these domains from each of the subunits form functioning receptors containing agonist binding sites, an ion permeation pathway, and gating elements that regulate the opening and closing of the ion channel pore (Traynelis et al., 2010). In the following paragraphs, I describe in more detail those aspects of the structure and function of AMPARs that are relevant to my thesis.

1.3.2 AMPA receptor heterogeneity

AMPAR subunit heterogeneity is effectively increased beyond that resulting from gene multiplicity, as the mRNAs encoding each type of subunit undergo post-transcriptional modification produced by alternative splicing and RNA editing (Cull-Candy et al., 2006; Sukumaran et al., 2012). Thus, all subunits have alternative 'flip/fop' splice variants (Salussolia and Wollmuth, 2012), while subunits GluA2-4 display R/G mRNA editing at a site between M3 and M4 (Lomeli et al., 1994). However, most significant is the RNA editing of the GluA2 subunit, in which an uncharged glutamine residue (Q) present at a position adjacent to the M2 helix in the pore lining is replaced by a positively charged arginine residue (R) (Sommer et al., 1991). This Q/R editing occurs in almost 100% of GluA2 subunits and is responsible for key changes in receptor function.

Receptors lacking GluA2 are Ca^{2+} permeable (Jonas et al., 1994) with a relatively

high single-channel conductance (Swanson et al., 1997), and exhibit inwardly rectifying current-voltage relationships due to their voltage-dependent block by endogenous intracellular polyamines (Bowie and Mayer, 1995; Kamboj et al., 1995; Koh et al., 1995a). Conversely, receptors containing edited GluA2 subunits – through the introduction of a positively charged residue close to the pore – no longer allow the permeation of Ca^{2+} (Jonas et al., 1994). Such channels exhibit linear current-voltage relationships (Bowie and Mayer, 1995; Jonas et al., 1994; Kamboj et al., 1995; Koh et al., 1995a) and a reduced single-channel conductance (Swanson et al., 1997). Interestingly, this editing at the GluA2 Q/R site influences AMPAR subunit assembly; in the presence of other subunits, GluA2 subunits preferentially form heterotetramers as the presence of the charged arginine in the channel pore disfavours the assembly of GluA2 subunits adjacent to one another (Greger et al., 2003). The structure of an AMPAR subunit and an assembled receptor is illustrated in Figure 1.1.

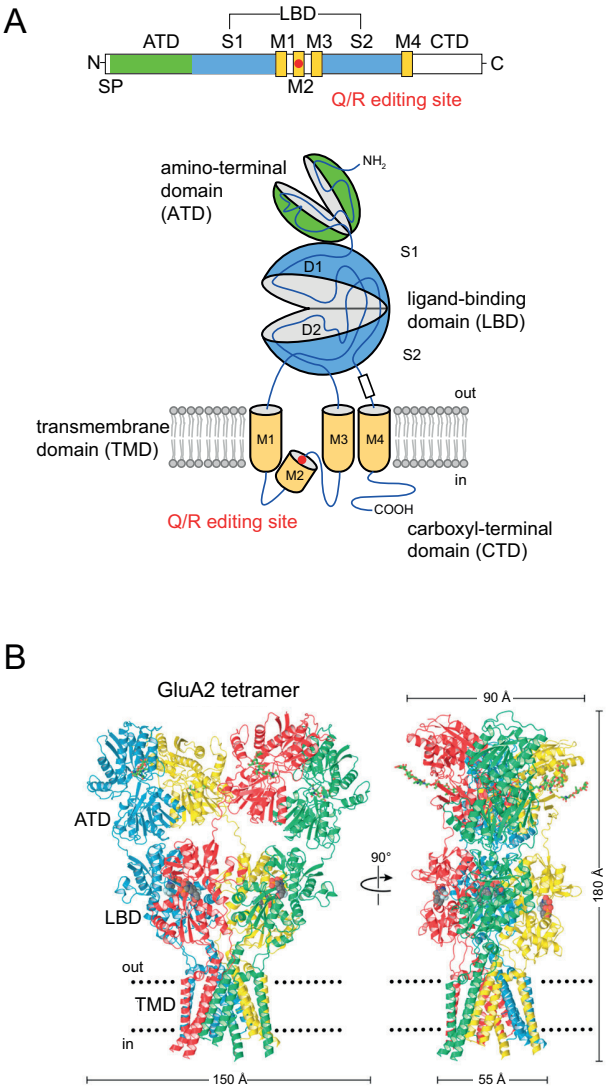

Figure 1.1: **Structure and domain organization of the AMPA receptor**. (**A**) Cartoon illustrating a linear representation of the subunit polypeptide chain and a schematic illustration of the topology of an individual subunit. Each subunit has (i) two large extracellular domains – the ATD (green) and the LBD (blue), (ii) a TMD (orange), part of which forms the ion channel pore, and (iii) an intracellular CTD. The LBD is composed of two segments termed S1 and S2. The TMD contains three membrane-spanning helices (M1, M3, and M4) and a re-entrant loop (M2). SP denotes signal peptide. The Q/R editing site of GluA2 is illustrated by a red circle. (**B**) Crystal structure at 3.6 Å of the membrane-spanning tetrameric GluA2 AMPA receptor (PDB code 3KG2; Sobolevsky et al. 2009) with each subunit in a different colour. Adapted from Fleming and England (2010) and Traynelis et al. (2010)

Ca^{2+} permeability and voltage-dependence

The entry of Ca^{2+} clearly distinguishes CP- from Ca^{2+} impermeable (CI-) AMPARs. Of note, although significant, the magnitude of Ca^{2+} entry through CP-AMPARs is less than that seen with NMDARs. Thus, for the most CP-AMPARs ~4% of the total inward current is carried by Ca^{2+} ions while for typical NMDA receptors the corresponding value is ~15% (Burnashev et al., 1995; Schneggenburger, 1996). For example, recombinant GluR1 homomers exhibit a $P_{Ca}/P_{Na,K}$ ratio of 2.3, compared with 3–17 for NMDARs (depending on their exact subunit composition) and <0.1 for Ca^{2+} impermeable GluR1/2 heteromers (Dingledine et al., 1999; Traynelis et al., 2010). Kainate receptors may also exhibit a limited Ca^{2+} permeability when assembled from edited GluK1 and GluK2 subunits (Traynelis et al., 2010).

Due to their block by extracellular Mg^{2+}, NMDARs require membrane depolarization to allow ion flow (Ascher and Nowak, 1988; Burnashev et al., 1992; Mayer and Westbrook, 1987; Nowak et al., 1984). This strong voltage-dependence means that NMDARs have the ability to act as detectors of coincident pre- and postsynaptic activity, a feature that is key to associative learning (Bliss et al., 1993) (see section 1.7). The resulting Ca^{2+} entry is thought to trigger the activation of various intracellular cascades essential for the induction of synaptic plasticity (see section 1.7). CP-AMPARs on the other hand are blocked by intracellular polyamines, such as spermine and spermidine, at depolarised voltages and have their greatest conductance at hyperpolarised voltages (Bowie and Mayer, 1995; Washburn et al., 1997). See Figure 1.2.

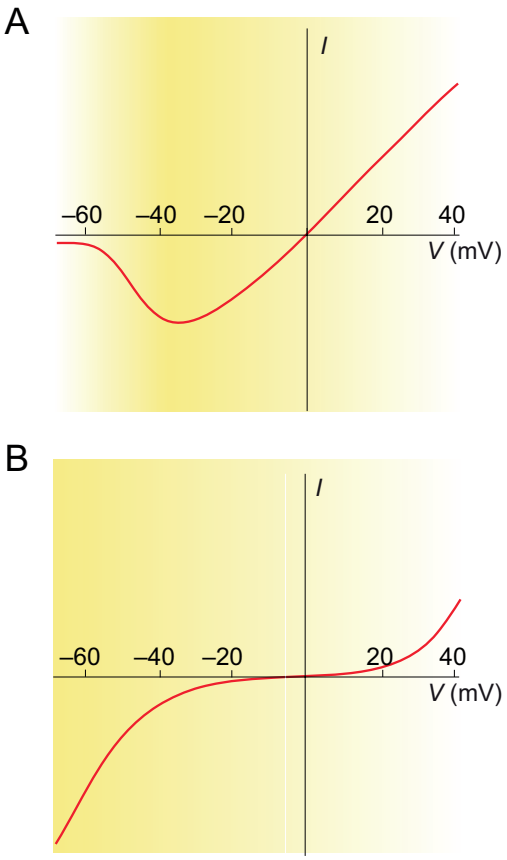

Figure 1.2: **Current-voltage relationships (*I-V*) of NMDA- and AMPA receptor-mediated currents.** (**A**) Voltage dependence of NMDAR-mediated current in the presence of extracellular Mg^{2+}. (**B**) Voltage dependence of CP-AMPAR-mediated current. In both cases the yellow shading indicates the magnitude of Ca^{2+}entry, which requires postsynaptic depolarisation for NMDARs but for AMPARs is greatest when the postsynpatic membrane is at resting potential or hyperpolarised. Figure adapted from Kullmann and Lamsa (2007).

AMPAR auxillary subunits

Although the subunit composition of AMPARs determines their biophysical and pharmacological properties, these are also strongly influenced by the presence of various auxiliary subunits that regulate receptor trafficking and gating. In recent years, multiple AMPAR auxiliary subunits have been identified. These are the transmembrane AMPAR regulatory proteins (TARPs) (Chen et al., 2000; Priel et al., 2005; Tomita et al., 2004, 2005), cornichons (Schwenk et al., 2009), cystine-knot AMPAR modulating protein 44 (CKAMP44) (Von Engelhardt et al., 2010), and germ-cell-specific gene 1-like (GSG1L) (Schwenk et al., 2012; Shanks et al., 2012). The best characterized of these proteins are the TARPs, which form stable complexes with both homo- and heteromeric AMPARs. Six TARP isoforms have been described – γ-2 (stargazin), γ-3, γ-4, γ-5, γ-7, and γ-8, with distinct developmental and spatial patterns of expression in the CNS (Fukaya et al., 2005; Schwenk et al., 2014). Many studies have characterised their differential modulation of the trafficking, synaptic targeting, gating and pharmacology of AMPARs (reviewed in Jackson and Nicoll (2011) and Straub and Tomita (2012)). Importantly, TARPs generally slow AMPAR deactivation and desensitization (Nicoll et al., 2006) and increase AMPAR single-channel conductance (Soto et al., 2007; Tomita et al., 2005), attenuate the block of CP-AMPARs by intracellular polyamines and increase their Ca^{2+} permeability (Coombs et al., 2012; Kott et al., 2009).

Detection of CP-AMPARs

Given the important distinction between GluA2-containing CI- and GluA2-lacking CP-AMPARs, various functional approaches have been adopted to determine their presence at synapses. Two methods are most widely used; the assessment of polyamine-dependent rectification (for example Bats et al. 2012; Matta et al. 2013; Mattison et al. 2014; Studniarczyk et al. 2013) and the use of CP-AMPAR-selective toxins such as philanthotoxin-433 (PhTx) (Osswald et al., 2007; Washburn and Dingledine, 1996), Joro spider toxin (JSTX) (Blaschke et al., 1993), argiotoxin (Strømgaard and Mellor, 2004) and Naspm (Blaschke et al., 1993; Koike et al., 1997; Washburn and Dingledine, 1996).

1.4 Neocortical circuits

In a rapidly changing world our senses are constantly providing new information. Appropriate behavioural choices require that the brain must identify relevant features from this enormous input. In mammals, the neocortex plays a key role in this process. As with other brain areas, its normal function depends on the appropriate balance of excitatory and inhibitory activity. How this activity is orchestrated in the neocortex is determined by the organization of its functional subunits, the neocortical microcircuits.

In the neocortex most (~80%) neurons are projecting excitatory PCs and ~20% are GABA-releasing INs (DeFelipe and Fariñas, 1992; Markram et al., 2004). These cells are arranged in six layers (L1-L6). INs are present in all layers, PCs are found in layers L2 to L6 and excitatory spinate stellate cells (SSCs) are found only in layer L4 (Grillner et al., 2005; Silberberg et al., 2005). A simplified view of the sensory neocortex is that sensory input from the primary thalamus targets all cortical layers but predominantly L4 and the L5-L6 border, while contextual inputs from higher-order cortex and thalamus most densely target L1, L5 and L6, but not L4 (Constantinople and Bruno, 2013; Petreanu et al., 2009; Thomson and Lamy, 2007). PCs and SSCs in L4 project most strongly to more superficial layers (L2/3) (Petreanu et al., 2009; Thomson and Lamy, 2007). PCs in L2/3 project to higher order and contralateral cortices as well as L5 (Callaway, 2004; Douglas and Martin, 2004; Feldmeyer, 2012). L5 projects locally to L2/3 and L6, and distally to a wide range of subcortical targets as well as other cortical regions and the contralateral cortex (Harris and Mrsic-Flogel, 2013; Silberberg et al., 2005; Thomson and Lamy, 2007). The projection of L6 is mainly back to L4 of the cortex but also to the thalamus (Briggman et al., 2011; Feldmeyer, 2012). This neocortical circuit is illustrated in Figure 1.3A. Although generally accepted, a recent study challenges this view by showing that thalamocortical inputs strongly innervate L5 as well as L4, suggesting two seperate parallel processing systems (Constantinople and Bruno, 2013).

Although there are subtle differences between the layers of the neocortex (Gabbott and Somogyi, 1986; Gonchar and Burkhalter, 1997), the overall balance between the numbers of PCs and INs is relatively consistent across species (for example when con-

sidering the visual cortex of monkey (Jones, 1993), cat (Gabbott and Somogyi, 1986), rat (Gonchar and Burkhalter, 1997; Meinecke and Peters, 1987) and mouse (Gonchar et al., 2007)). The relative number and anatomical organization of excitatory- and inhibitory inputs (asymmetrical and symmetrical synapses) onto PCs is also conserved (DeFelipe et al., 2002). While asymmetrical synapses constitute 80-90% of all synapses and arise from other cortical regions or layers, thalamocortical inputs as well as local axon collaterals of PCs and SSCs, the percentage of symmetrical synapses varies between 10-20% and its main source are GABAergic INs (DeFelipe et al., 2002). Excitatory inputs contact only the dendrites, while inhibitory inputs terminate on the dendrites, the axon initial segment and the soma (Markram et al., 2004). Thus, the overall proportions of excitatory and inhibitory neurons as well as the patterns of anatomical connections repeat themselves in a relatively stereotyped manner.

The probability of connections between neighbouring PCs is often low, indicating that PCs are connected to only a small fraction of their neighbouring cells (Markram et al., 1997a,b; Sjöström et al., 2001; Thomson et al., 1993). Nevertheless, careful analysis of the connections between PCs has revealed that these are highly non-random, with bidirectional connections between pairs of PCs, and patterns of mutual interconnection among larger assemblies of neurons occuring more frequently than would be expected by chance (Perin et al., 2011; Song et al., 2005). Such non-uniform connectivity is seen both within and between layers. In general, PCs are more likely to be reciprocally connected if they receive common intra- or inter-laminar input (Otsuka and Kawaguchi, 2011; Yoshimura et al., 2005). Importantly, this local synaptic connectivity is echoed in functional specificity. Thus, in the mouse visual cortex, the probability that nearby PCs are connected is higher for neurons that respond to similar visual features (Ko et al., 2011). Overall it seems likely that, rather than being composed of repeating stereoptypical microcircuits, each cortical area contains multiple interlaced subnetworks of strongly interconnected PCs within a sea of weakly connected PCs. While PC–PC connectivity is specific, that between PCs and INs seems to be non-specific (Fino and Yuste, 2011; Harris and Mrsic-Flogel, 2013; Packer and Yuste, 2011).

Unlike PCs, neocortical INs (at least the parvalbumin- (PV) and somatostatin-expressing

(SOM) classes) exhibit a high density of connectivity to nearby PCs (Fino and Yuste, 2011; Packer and Yuste, 2011), while forming connections to distinct subcellular locations (Ascoli, 2008; Karube et al., 2004; Somogyi et al., 1998). Additionally, INs connect to other INs and show a remarkable degree of cell-type target specificity (DeFelipe et al., 2002; Pi et al., 2013; Pfeffer et al., 2013). While PV-expressing INs, for example, preferentially inhibit each other (Pfeffer et al., 2013), other populations such as vasoactive intestinal peptide (VIP)- or SOM-expressing INs avoid inhibiting each other but strongly inhibit other IN populations (Pfeffer et al., 2013; Pi et al., 2013). This overall neocortical circuit is illustrated in Figure 1.3B.

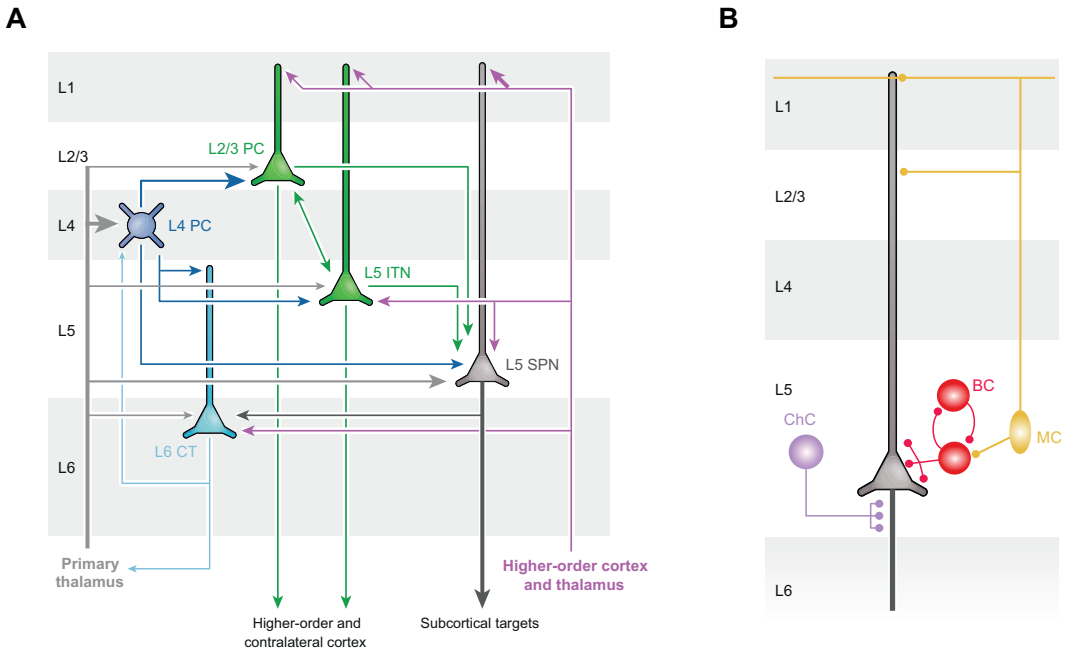

Figure 1.3: **Cortical connections.** (**A**) Connectivity between major cortical principal cell classes and their input pathways. The line thickness indicated the strength of individual pathways. In L5, intratelencephalic neurons (ITNs) are commonly found in the upper L5, projecting to L2/3 and to the ipsi- and contralateral cortex but, as their name suggests, not outside the telencephalon. Subcerebral projection neurons (SPNs), on the other hand, give little local output but provide output to higher-order thalamus, the ipsilateral striatum and subcerebral motor centers. Corticothalamic cells (CTs) in L6 project to L4 as well as the thalamus. (**B**) Synaptic inputs to a PC (grey) made by three different types of L5 INs. BCs (red) inhibit each other and target the soma and proximal dendrites of PCs. Chandelier cells (ChCs) target the axon initial segment of PCs. MCs target the distal (tuft) dendrites of PCs and inhibit other INs such as BCs. Not shown are other IN types of L5 such as bitufted or bipolar cells. Modified from Harris and Mrsic-Flogel (2013).

1.5 The visual cortex

The neocortex is subdivided into areas distinguished by their afferent and efferent connections, their functional properties, as well as by their neurochemical characteristics. The visual cortex is located at the most occipital part of the brain and processes constantly changing natural scenes.

Visual processing begins in the retina, and the output – from the retinal ganglion cells – passes via the optic nerve to the optic chiasm and then to the lateral geniculate nucleus (LGN) located in the dorsal thalamus. In the mouse, with a relatively small field of binocular vision, the majority of fibers cross over to the contralateral hemisphere (Hübener, 2003). The LGN provides direct input to the primary visual cortex (V1), which in turn passes on visual information to higher areas of the visual cortex (V2-V6). The majority of thalamocortical projection from the LGN to V1 arrives in L4 and also in superficial layers (Hofer et al., 2006). Cells in V1 show selectivity in their responses to specific visual features and display characteristics that include direction-selectivity and orientation- or frequency tuning (Atallah et al., 2012; Runyan et al., 2010). As described in later chapters, I made recordings from INs in slices of mouse V1.

1.6 Cortical IN diversity

Understanding IN function is important for the understanding of the circuit as a whole. As alluded to above, inhibitory INs are heterogeneous and this adds substantial complexity to the neocortical microcircuits. Many different studies have been carried out in the quest to characterise IN types, which are distinguishable by their morphology (especially their axonal arborisation), by their electrophysiological properties, and by their molecular makeup (Ascoli, 2008; Markram et al., 2004).

The classification of neurons based on their morphology could be considered to have begun in earnest in the early 20th century, when Ramón y Cajal produced detailed drawings of diverse neuronal morphologies based on Golgi's silver staining technique

(Ramon y Cajal, 1911). Subsequently, methods to trace and reconstruct complex neuronal morphologies have become routine, with the number of published IN reconstructions dramatically increasing towards the end of the 1990s (Halavi et al., 2012; Parekh and Ascoli, 2013). INs exhibit great variety in their somatic, dendritic and axonal morphologies, and can be most easily distinguished on the basis of their axonal aborization and targeting domains (DeFelipe, 1997; Somogyi et al., 1998). A variety of axon-, soma-, proximal dendrite-, and distal dendrite-targeting INs have been described (Markram et al., 2004). Figure 1.4 illustrates how the importance of axonal morphology to distinguish IN cell types was recognized by Ramón y Cajal (Ramon y Cajal, 1911), and how this remains the best neuronal characteristic by which to identify cell classes (Markram et al., 2004).

INs display distinct firing patterns and the identification of IN types on the basis of physiological criteria has been refined over the last couple of decades. Initially, INs were described as fast spiking (McCormick et al., 1985), but later studies introduced additional terms to describe diverse firing behaviour, including burst spiking or regular spiking (Kawaguchi and Kubota, 1997). Most recently, the electrophysiological classification of INs has been based on both their initial response to current injection (burst, delayed or continuous firing) and their steady-state response to current injection (fast spiking, non-adapting non-fast spiking, adapting, irregular spiking, intrinsic burst firing or accelerating firing) (Ascoli, 2008).

INs also contain different molecular markers and distinct groups of INs can be classified based on their molecular expression of specific calcium-binding proteins such as PV, calbindin (CB), calretinin (CR) as well as neuropeptides such as SOM, VIP, neuropeptide Y (NPY) and cholecystokinin (CCK) (Cauli et al., 1997; Demeulemeester et al., 1991; Markram et al., 2004; Ascoli, 2008). The groups of INs identified in this way can be further characterised by, for example, expression patterns of ion channels, transcription factors, neurotransmitter receptors and by their place of origin in the medial ganglionic eminence (MGE), the lateral and dorsocaudal ganglionic eminence (CGE) or preoptic area (POA) (Markram et al., 2004).

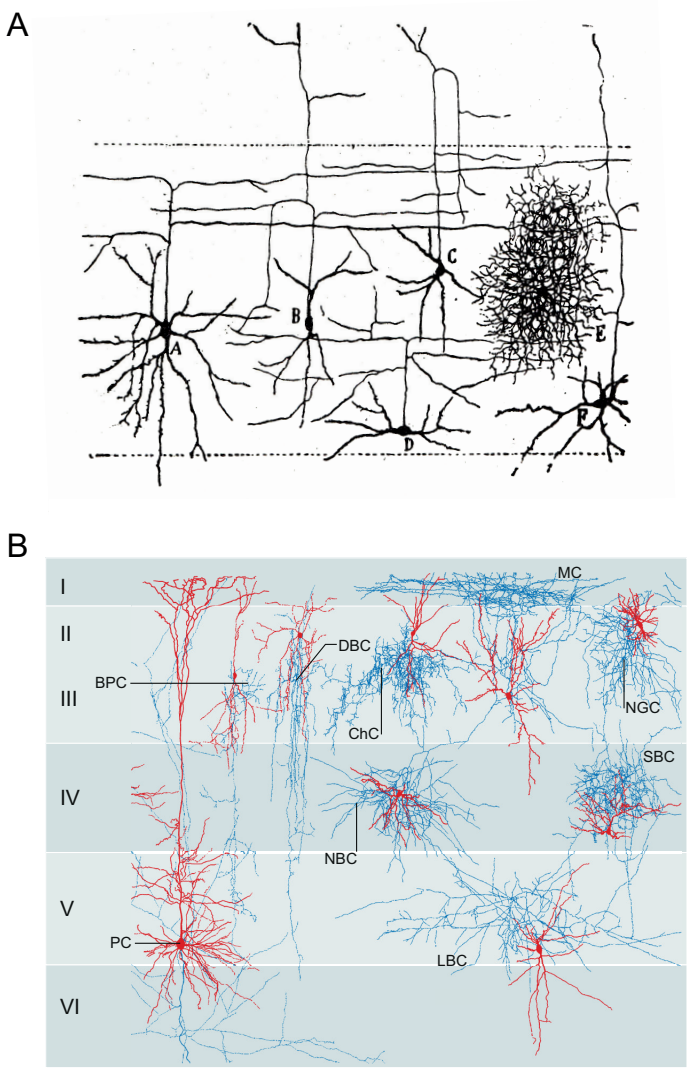

Figure 1.4: **Diversity of axonal arborisation of neocortical INs.** (**A**) A drawing by Ramón y Cajal (based on the Golgi method) of "cells with a short axons" from layer 4 of the motor cortex of a 1 month old human. A and D are "cells with an ascending axon issuing tangential branches extending through layer 4"; B and C are "cells with an arcuate axon furnishing branches to layer 3"; E "arachniform cell"; F "neuron sending its axon to the plexiform layer" Ramon y Cajal (1911). (**B**) Reconstructions of several classes of different neocortical INs. Axons in blue, dendrites in red. A pyramidal cell (PC) in L5 is shown for comparison. Cells illustrated are: a bipolar cell (BPC), a chandelier cell (ChC), a double bouquet cell (DBC), a large basket cell (LBC), a small basket cell (SBC), a nest basket cell (NBC), a Martinotti cell (MC) and a neurogliaform cell (NGC). Figures adapted from Ramon y Cajal (1911) and Huang et al. (2007).

The above introduced classification approaches are not sufficient in isolation. For example, electrophysiologically identified INs can display a variety of molecular markers (Cauli et al., 1997) and two INs with the same firing pattern may have different morphologies (Karube et al., 2004). Additionally, efforts to classify IN types have lead to controversy regarding the entire question of classification and cast doubt on the idea that the variability in IN features within a class is necessarily smaller than the differences between classes. Thus, certain studies suggest a large number of IN classes (Gupta et al., 2000) while others suggest that there are no clear classes, rather a contiunuum (Parra et al., 1998). The efforts to form a complete classification of IN types has been additionally hindered by the lack of consensus in selecting classification schemes (and the naming of IN types). Extensive efforts from leading groups in the field to standardise IN classification has resulted in the so-called 'Petilla classification' (Ascoli, 2008; DeFelipe et al., 2013).

Importantly, the Petilla classification identifies BCs and MCs as two clearly defined and mutually exclusive cortical IN types; in the following subsections I describe these cells in more detail.

1.6.1 Basket cells

The largest group of cortical INs is formed by BCs, which in L5, for example, make up around 50% of all INs (Gonchar et al., 2007; Markram et al., 2004). BCs typically exhibit a 'fast spiking' (FS) firing behaviour with narrow action potentials, strong spike afterhyperpolarisation, little or no spike accommodation and maintained high firing frequencies, with various differences such as 'stuttering' or 'bursting' patterns (Gupta et al., 2000; Markram et al., 2004; Wang et al., 2002). PV-expressing fast spiking cells include both BCs and ChCs (Kawaguchi and Kubota, 1997; Woodruff et al., 2009; Ascoli, 2008). However, not all fast spiking BCs express PV (Wang et al., 2002). Nevertheless, BCs are typically associated with fast spiking behaviour and PV expression. BCs are morphologically typified by an axon with many horizontally and vertically projecting axon collaterals radiating in all directions (Somogyi et al., 1983; Wang et al., 2002). They express comparatively low dendritic spine density

(Kawaguchi et al., 2006) and exhibit some variation in morphology, reflected in their size ('large', 'small', 'nest') and the extent of neurite arborisation – remaining within the layer or extending to other layers (Gupta et al., 2000; Kawaguchi and Kubota, 1997; Wang et al., 2002). In keeping with their morphology, BCs contact the somatic and proximal dendritic region of PCs; their name 'basket cell' reflecting the basket-like aborisation on and around PC somata (Kätzel et al., 2011; Somogyi et al., 1983, 1998; Wang et al., 2002).

BCs receive long-range excitatory input from the thalamus (Cruikshank et al., 2007, 2010; Gabernet et al., 2005) and excitatory input from local PCs (Wang et al., 2002). Excitatory synapses onto BCs are depressing (Buchanan et al., 2012; Silberberg and Markram, 2007). BCs are involved in both feedback and feedforward inhibiton depending on their input, with cortical BCs in L5 involved in a frequency-independent disynaptic inhibition (FIDI) microcircuit (Silberberg and Markram, 2007) and, in V1, form extensive recurrent connections with PCs of the same layer (Hofer et al., 2011; Yoshimura and Callaway, 2005). Of note, in the mouse primary visual cortex, BCs have been shown to receive inhibition from other BCs and MCs (Pfeffer et al., 2013).

BCs are characterized by their temporally precise excitation, giving them a role in rapidly converting excitatory input to inhibitory output (Jonas et al., 2004). Synchronous activity of BCs generates gamma oscillations in cortical networks (Cardin et al., 2009) and in the visual cortex they modulate spiking responses of PCs to visual stimuli, influencing gain control during visual processing (Atallah et al., 2012). The important role of BCs in the stabilization of the cortical network is apparent when one considers that loss of inhibition mediated by BCs leads to severe generalized epilepsy (for example Rossignol et al. 2013) while more subtle BC dysfunction contributes to psychiatric disorders including schizophrenia (Lewis et al., 2005).

1.6.2 Martinotti cells

MCs were first described by Carlo Martinotti (Martinotti, 1889; see Wang et al., 2004) and subsequently named by Ramón y Cajal (Ramon y Cajal, 1911). In the cortex, MCs

are found in L2 to L6 and make up the second largest group of INs; in L5 for example, they constitute roughly 30% of INs (Markram et al., 2004; Wang et al., 2004). In response to depolarizing step currents MCs exhibit low threshold, non-fast spiking behaviour and almost always show spike accommodation (Silberberg and Markram, 2007; Wang et al., 2004). On an molecular level, MCs express SOM but not PV (Kawaguchi and Kubota, 1996; Markram et al., 2004; Wahle, 1993). Morphologically, MCs have very characterisitic axon collaterals that ascend to L1 where they can extend horizontally for millimeters (DeFelipe, 2002; Kawaguchi and Kubota, 1997; Wang et al., 2004), a dendritic tree significantly smaller than the axonal tree and an ovoid shaped soma (Karube et al., 2004; Kawaguchi and Kubota, 1996; Silberberg and Markram, 2007; Wang et al., 2004). MC axons are unusal for INs in that they exhibit spines (Kawaguchi et al., 2006). MCs preferentially target distal apical and tufted dendrites of PCs (Kawaguchi and Kubota, 1997; Silberberg and Markram, 2007; Somogyi et al., 1998).

MCs are driven primarily by intra- and translaminar PCs (Berger et al., 2009; Kapfer et al., 2007; Silberberg and Markram, 2007) while receiving little thalamic drive (Cruikshank et al., 2010). In the mouse primary visual cortex, Pfeffer et al. (2013) have shown that MCs receive little if any inhibition from BCs, but receive some inhibition from VIP-expressing INs. MCs can be activated by repeated action potentials in single PCs as a consequence of exhibiting strong facilitating excitatory inputs. In turn they provide strong feedback inhibition onto neighbouring PCs (Kapfer et al., 2007), resulting in strongly frequency-dependent disynaptic inhibition (FDDI) in L5 (Kapfer et al., 2007; Silberberg and Markram, 2007; Berger et al., 2009). By virtue of their unique anatomical and synaptic features, MCs are well suited to control dendritic integration of synaptic inputs onto PCs. The distinctive targetting of PC distal dendritic tufts in L1 suggests that MCs are not involved in gain control of firing but in the modulation of dendritic excitability (Silberberg and Markram, 2007). Unlike BCs, which are thought to be transiently activated when network activity is low, MCs (because they receive facillitating excitatory input) are thought to be activated preferentially during periods of increased network activity, providing feedback inhibition that increases with increased rate and duration of PC discharge (Kapfer et al., 2007; Silberberg and Markram, 2007).

1.7 Synaptic plasticity

In addition to diversity in cell types, functional diversity among synaptic connections, notably their ability to show short- (generally lasting from a few milliseconds to tens of seconds Abbott and Regehr, 2004; Zucker and Regehr, 2002) and long-term (lasting for hours, days and weeks Abbott and Regehr, 2004) changes in strength, adds to the complexity of the microcircuit. Long-term plasticity of individual synaptic connections is thought to underly learning and memory formation (Morris et al., 1986).

The Canadian neuropsychologist Donald Hebb postulated that when a presynaptic neuron repeatedly and persistently takes part in evoking the firing of a postsynaptic neuron, then the strength of the connection between them should be increased (reviewed in Sjöström et al., 2008). Experimentally, under different conditions, both synaptic strengthening (long-term potentiation; LTP) or weakening (long-term depression; LTD) can be observed. In the classical model of plasticity, long-term changes are commonly rate-based, with high frequency stimulation of glutamatergic synapses leading to LTP and low frequency stimulation leading to LTD (Bliss and Lomo, 1973; Sjöström and Nelson, 2002). Whether LTP, LTD, or no plasticity is induced at a given connection, is critically dependent on the frequency as well as the precise timing between repeated pre- and postsynaptic firing. Many of the present insights into spike timing dependent plasticity (STDP) came from studies carried out on excitatory synapses onto glutamatergic neurons. Here, for frequencies between 10 and 50 Hz, LTP is induced when presynaptic spiking occurs around 10-15 ms (sometimes less) before postsynaptic firing (‘pre before post’), and LTD is seen when the order is switched (‘post before pre’) (Markram et al., 1997b; Sjöström et al., 2001). Of note, a single excitatory neuron can form synapses with distinct properties onto different postsynaptic partners, forming synapses onto other PCs that display short-term depression and synapses onto INs that display facilitation (Markram et al., 1998). The concept of target-specific differences in synaptic transmission was provided initially by work on invertebrates (Frank, 1973; reviewed in Tóth and McBain 2000). A study by Thomson (1997) in the rat neocortex showed that depending on the postsynaptic partner, PCs form depressing or (more rarely) facilitating synapses onto postsynaptic PCs, while forming only facilitating synapses onto INs. Studies by Shigemoto et al. (1996) and Scanziani et al.

(1998) in the hippocampus, showed target-specific differences in presynaptic mGluR expression among terminals of single PC axons. Conversely, two distinct afferent pathways converging onto the same postsynaptic IN can exhibit distinct AMPARs (Tóth and McBain, 1998).

IN diversity is reflected in the diversity of mechanisms by which LTP and LTD of their excitatory inputs can be induced (Lamsa et al., 2010). Interestingly, LTP of excitatory connections is specific to the type of postsynaptic IN (Lamsa et al., 2007; Lu et al., 2007; Nissen et al., 2010). For example, a study carried out in L2/3 of the somatosensory cortex showed that STDP was remarkably different between FS and low threshold spiking (LTS) IN subpopulations (Lu et al., 2007). In another study, carried out in the hippocampus, plasticity differences were seen among INs with similar axonal branching patterns dependant on their neurochemical markers; LTP or LTD was induced in PV-positive INs (according to their axonal targeting domain) while the same induction protocol produced no plasticity in INs expressing the cannabinoid receptor-1 (CB1) (Nissen et al., 2010). Such studies highlight why, in recent years, neurochemical markers have become important as additional tools to classify IN subpopulations (Ascoli, 2008).

As described below, LTP and LTD are triggered by changes in postsynaptic Ca^{2+}. Regardless of the timing and frequency of pre- and postsynaptic spiking, slower and smaller elevations of intracellular Ca^{2+} tend to give rise to LTD while faster and larger changes induce LTP (Sjöström and Nelson, 2002). However, the route of calcium entry – reflecting the specific postsynaptic receptor expression – influences the form of LTP expressed.

1.7.1 The role of Ca^{2+} in synaptic plasticity

Hebbian LTP in PCs is generally believed to require NMDAR activation (Collingridge et al., 1983). The resulting rise of Ca^{2+} in dendritic spines (Nicoll et al., 1988) triggers the activation of signaling proteins such as calcium/calmodulin-dependent kinase II (CaMKII), phosphorylating various targets including postsynaptic density (PSD) proteins and/or AMPARs themselves. This is thought to either (i) create new 'slots' for

the capture of additional AMPARs, (ii) phosphorylate AMPARs allowing their capture by existings slots or (iii) act on membrane trafficking machinery, driving exocytosis of AMPAR-containing vesicles (Huganir and Nicoll, 2013). The primary change associated with LTP is the gross increase in the number of AMPARs at the synapse (Huganir and Nicoll, 2013; Lüscher et al., 1999; Sjöström et al., 2008). Whether this includes the initial transient insertion of CP-AMPARs, is disputed (Adesnik and Nicoll, 2007; Plant et al., 2006). Additonally, LTP has been associated with an increase of the single-channel conductance of AMPARs (Benke et al., 1998) and CaMKII phosphorylation of the GluA1 AMPAR subunit has been shown to regulate AMPAR channel conductance (Derkach et al., 1999).

Ca^{2+} influx can also occur via receptors other than NMDARs – specifically via CP-AMPARs, which have been also implicated in the induction of LTP (Kullmann and Lamsa, 2007; Lamsa et al., 2007; Oren et al., 2009). As discussed in section 1.3 on page 17, NMDARs are known to act as coincidence detectors, being blocked by extracellular Mg^{2+}, requiring glutamate binding and depolarization for their activation (Corlew et al., 2008). CP-AMPARs on the on the other hand are blocked by intracellular polyamines, such as spermine and spermidine, at depolarised voltages and have a greatest conductance at hyperpolarised voltages. These opposite requirements mean that NMDARs and AMPARs are involved in Hebbian and anti-Hebbian plasticity, respectively (Kullmann and Lamsa, 2007). The induction of anti-Hebbian (unlike Hebbian) LTP requires presynaptic activity in the absence of postsynaptic depolarisation (Lamsa et al., 2007).

Glutamatergic synapses onto PCs can activate different subtypes of AMPARs than do those onto aspiny INs (Hestrin, 1993). Specifically, the GluA2 subunit is less abundant in INs than in PCs (Kullmann and Lamsa, 2007). Excitatory connections onto different INs also show variations in ionotropic glutamate receptor expression. CI-AMPARs are often found at synapses that contain a significant number of NMDARs, while CP-AMPARs are often found at synapses with low numbers of NMDARs (Kullmann and Lamsa, 2007). Studies carried out on hippocampal INs show a crucial role of CP-AMPARs in the induction of anti-Hebbian LTP. This form of plasticity is activated by pre- but not postsynaptic firing, and plays an important role in the hippocampal

feedback circuit, orchestrating the overall excitability of PCs (Kullmann and Lamsa, 2007). Another study on hippocampal INs showed that NMDAR-dependent Hebbian LTP was activated by pre- and post-synaptic firing, and was seen at INs that play a leading role in hippocampal feed-forward inhibition, enhancing disynaptic inhibition (Lamsa et al., 2005; Szabo et al., 2012). The exact molecular players underlying plasiticity of connections onto INs in the neocortex has still to be elucitated.

In the following chapters, I explore the presence of AMPAR subtypes at the two major neocortical IN types, the BC and MC. After introducing the Methods (Chapter 2), the first Results chapter (Chapter 3) describes the morphology of the INs, the second Results chapter (Chapter 4) explores the electrophysiology of the IN types, including the current-voltage relationship of mEPSCs and their block by Naspm. In the final Results chapter (Chapter 5) I describe immunolabelling results examining the expression of the GluA2. The final chapter (Chapter 6) is a general Discussion.

Chapter 2

Methods and Materials

2.1 Animals

All experiments were performed using tissue from juvenile mice aged between postnatal days 14 and 21 (P14–P21). Of note, although the use of mice in this age range may have been expected to increase the variability in several synaptic parameters, as there are rapid developmental changes occurring in the third postnatal week, this was not particularly apparent in measures such as mEPSC, amplitude, risetime and decay (see Chapter 4). Four groups of mice were used: (a) FVB-Tg (GadGFP) 45704Swn/J (Jackson Laboratories 003718), commonly referred to as the GIN line (Oliva et al., 2000), (b) CB6-Tg(Gad1-EGFP)G42Zjh/J (Jackson Laboratories 007677), commonly referred to as the G42 line (Chattopadhyaya et al., 2004), (c) the naturally occurring mutant *stargazer* (*stg*/*stg*) (Letts et al., 1998; Noebels et al., 1990) and (d) C57BL/6 'wild-type' (WT).

In the two transgenic lines, enhanced green fluorescent protein (EGFP) is expressed under the control of the *Gad1* (GAD67; glutamic acid decarboxylase 67) gene promoter. In the first group, transgene expression has been shown to occur throughout the CNS in a specific subpopulation of GABAergic INs that express SOM (Oliva et al., 2000). In the second, EGFP has been shown to occur in a specific subpopulation of GABAergic INs that express PV (but not SOM or cholecystokinin) (Chattopadhyaya et al., 2004). Thus, these animals allowed targeted patching from identified cortical

IN subgroups. Typically, the colonies were maintained by breeding hemizygous mice to C57BL/6 animals. Occasionally, for both GIN and G42 lines (hereafter referred to as 'SOM' and 'PV' mice), hemizygous animals were crossed. Offspring were identified as GFP-expressing at P0–P2 by illuminating them with a blue light emitting diode (LED) (492/18 nm single-band bandpass filter; Semrock FF01-482/18-25) and viewing the head through a coloured glass filter (495 nm longpass; Thorlabs FGL 49S).

S*targazer* mice were bred from +/*stg* mice (C57BL/6 background) and were identified according to their phenotype – smaller body size, abnormal head movements and unsteady gait (Noebels et al., 1990).

All procedures for the care and treatment of mice were in accordance with the UK Animals (Scientific Procedures) Act 1986.

2.2 Slice preparation

Cortical slices were prepared from mice of both sexes, as described previously for rats (Sjöström et al., 2001). To anaesthetise the mice they were placed in a perspex induction chamber with a mesh floor, beneath which were placed three cotton buds soaked in isoflurane (IsoFlo; Abbott Laboratories). The chamber was connected to a vacuum pump (Fluovac PY2 34-0387; Harvard Apparatus) and an activated carbon anaesthetic scavenging filter (Fluosorber PY2 34-0415; Harvard Apparatus). When animals became inactive they were removed from the chamber and tested for the loss of a hind limb withdrawl reflex (in which pinching the foot of one hind limb would normally cause flexion of the stimulated limb). They were then rapidly decapitated using a sharp pair of scissors.

Using a scalpel blade (No. 11; Swann Morton) a cut was made along the midline of the scalp to remove the fur and skin. Using small scissors, one cut was made along the midline of the skull, two cuts were made to the rear of the occipital bone and a final cut was made between the eyes, allowing the surface of the skull to be lifted off with forceps and the brain removed using a small curved spatula. The brain was placed into a dish (with a 5% Sylgard base) containing ice-cold slicing solution. This solution

contained (in mM): 87 NaCl, 75 sucrose, 26 $NaHCO_3$, 2.5 KCl, 1.25 NaH_2PO_4, 0.5 $CaCl_2$, 7 $MgSO_4$, and 25 glucose (pH 7.4 when bubbled with 95% O_2 and 5% CO_2).

While submerged in ice-cold slicing solution the brain was dissected along the midline using a scalpel blade (No. 22; Swann Morton). For each hemisphere two off-coronal cuts (20 degrees from vertical) were used to isolate a tissue block containing the visual cortex. Both blocks were glued (Loctite SuperGlue) to the slicing platform of a vibratome (VT1200S; Leica). The platform was then secured in the slicing chamber which was filled with ice-cold slicing solution (bubbled with 95% O_2 and 5% CO_2). Near-coronal slices containing the visual cortex were cut at 300 μm thickness. Slices were then transferred using a reversed pasteur pipette to an incubation chamber were maintained for 20–30 minutes at 37°C. Slices were then allowed to cool to room temperature and transferred to a second incubation chamber containing 'recording' solution containing (in mM): 125 NaCl; 2.5 KCl; 1 $MgCl_2$; 1.25 NaH_2PO_4; 2 $CaCl_2$; 26 $NaHCO_3$; 25 glucose, bubbled with 95% O_2 and 5% CO_2. The slices were maintained in this chamber for up to 6 hours.

Of note, since the first successful use of acute brain slices for patch-clamp electrophysiology (Edwards et al., 1989), various modifications to the originally described procedure have been investigated with a view to improving the quality of slices (i.e. to maximise the survival of healthy neurons amenable to patch-clamp recording) (Moyer and Brown, 1998; Tanaka et al., 2008; Ye et al., 2006; Zhao et al., 2011). These have generally involved modifications to the solutions used for cutting and incubation. Such alterations have included (but not been limited to) the addition of ascorbic acid (Borst et al., 1995; Rice et al., 1994) or pyruvate (Borst et al., 1995; Forsythe, 1994) to the conventional NaCl-based slicing solution, slicing in a K-gluconate solution to mimic the intracellular medium and thus prevent entry of calcium and other extracellular ions into cut neurites (Dugué et al., 2005), or slicing at a near-physiological temperature (34°C) (Huang and Uusisaari, 2013). Although I did not attempt any of these more exotic approaches, I found that partial replacement of sodium with sucrose (Aghajanian and Rasmussen, 1989; Geiger and Jonas, 2000) helped maintain the survival of INs, which are generally considered less resistant to various insults during the slicing process than, for example, PCs. When combined with the relatively young age of the

mice used (older animals tend to exhibit less resistance to anoxic damage during brain removal and increased myelination making slicing more difficult), this modification alone allowed the successful production of healthy slices. The precise composition of my slicing solution was adapted from Winterer et al. (2011) (see Table 2.1).

2.3 Visualisation and targeted patching of cells

Cortical slices were transferred to a shallow submerged recording chamber (~ 2.5 ml volume) mounted on the stage of an upright microscope (see below; section 2.3.1) and secured with a platinum wire harp strung with 4–5 individual nylon fibres teased from a pair of tights (Edwards et al., 1989). The chamber was perfused at a rate of 2–3 ml/min with gravity-fed recording solution that was continuously bubbled with 95% O_2 and 5% CO_2. The solution was heated using an in-line heater (HPT-2A heated perfusion tube; ALA Scientific Instruments). The temperature of the chamber was monitored with a thermistor probe and maintained at 32-34°C with a feedback controller (Scientifica). The bath temperature was continually displayed and recorded using custom software (Sjöström et al., 2001) running in Igor Pro 6 (WaveMetrics Inc.) on a PC (SL-4U-H67CL-HA; SuperLogics) running Windows 7 operating system (Microsoft).

2.3.1 Two-photon laser scanning microscope (2PLSM)

Slices were visualised following standard procedures (Tsai and Kleinfeld, 2009) using a custom-built 2PLSM (SliceScope; Scientifica) fitted with a multiphoton detection unit (MDU; Scientifica). The microscope was equipped with a motorized objective changer housing a 4x non-immersion objective (PlanN, 4x/0.10; Olympus) and a 40x water-immersion objective (LUMPlan FI/IR, 40x/0.8; Olympus).

The slice was illuminated from beneath (through a high-NA oil immersion condenser lens) with an 850 nm LED (M780L2; Thorlabs) and viewed using an infrared (IR)-sensitive charge-coupled device (CCD) camera (WAT-902H Ultimate; Watec). Contrast enhancement was provided by a Dodt-gradient contrast tube (Dodt and Zieglgänsberger, 1990; Stuart et al., 1993). This consisted of two lenses forming a 1X telescope

Slicing solution		**Recording solution**	
Compound	Concentration (mM)	Compound	Concentration (mM)
NaCl	87	NaCl	125
$NaHCO_3$	26	$NaHCO_3$	26
KCl	2.5	KCl	2.5
NaH_2PO_4	1.25	NaH_2PO_4	1.25
$CaCl_2$	0.5	$CaCl_2$	2
$MgSO_4$	7	$MgCl_2$	1
D-glucose	25	D-glucose	25
D-sucrose	75		

Table 2.1: **Composition of external solutions.** The pH of the solutions was adjusted to 7.3 by bubbling with 95% $O_2$and 5% CO_2. For both solutions the osmolality was adjusted with D-glucose to obtain a value of 336-340 mOsm. All chemicals were from Sigma, Fisher or VWR.

(LA1401 plano-convex lenses; Thorlabs) with a spatial filter (hand-cut from blackout foil) and a diffusor (DG20-1500-MD; Thorlabs) placed between the lenses (Nevian, 2003). Optimum contrast enhancement, combined with reduced scattering of IR illumination, allowed neurons to be visualised up to 100 μm beneath the slice surface.

Two-photon excitation was achieved using a mode-locked femtosecond pulsed Ti:Sa laser (MaiTai BB; Spectraphysics) gated using mechanical shutters (LS6ZM2/VCM-D1; Uniblitz). The laser beam was divided between two setups using a polarizing beam splitter (GL10-B; Thorlabs). Laser power was adjusted using a polarizing cube beam splitter (PBSH-450-1300-100; Melles Griot) and half-wave plate (AHWP05M-980; Thorlabs) and monitored with a power meter (13PEM001/1; Melles Griot) by picking off a fraction of the beam with a glass slide.

The laser beam was raster scanned across the sample by galvanometric mirrors (GVSM-002/M 5 mm; Thorlabs). Fluorescence detection was achieved by using two photomultiplier tubes (PMTs) (2PIMS multiphoton detection modules; Scientifica). 2PLSM reflected fluorescence was gathered with a dichroic and emitter passing 350–650 nm (FF665-Di01 and FF01-680/SP-25; Semrock). Fluorescence light was directed to the red- and green-selective PMTs using a second dichroic (FF560-Di01; Semrock) with red and green emitters (ET630/75m and ET525/50m; Chroma).

Transmitted laser light was used to perform laser scanning Dodt-contrast imaging, allowing viewing of the slice at the same time as the captured fluoresence images. The laser beam first passed through the specimen, a high-NA oil immersion condenser lens, and then travelled through the Dodt-gradient contrast tube. After the Dodt tube, a fraction of the laser beam was picked off using a glass slide or 50/50 beam splitter (BSW17; Thorlabs) and focused onto an amplified diode (PDA100A-EC; Thorlabs). Imaging data were collected with PCI-6110 A-D boards (National Instruments) using custom-modified versions of ScanImage v3.5-3.7 (Pologruto et al., 2003) and displayed in Matlab (MathWorks).

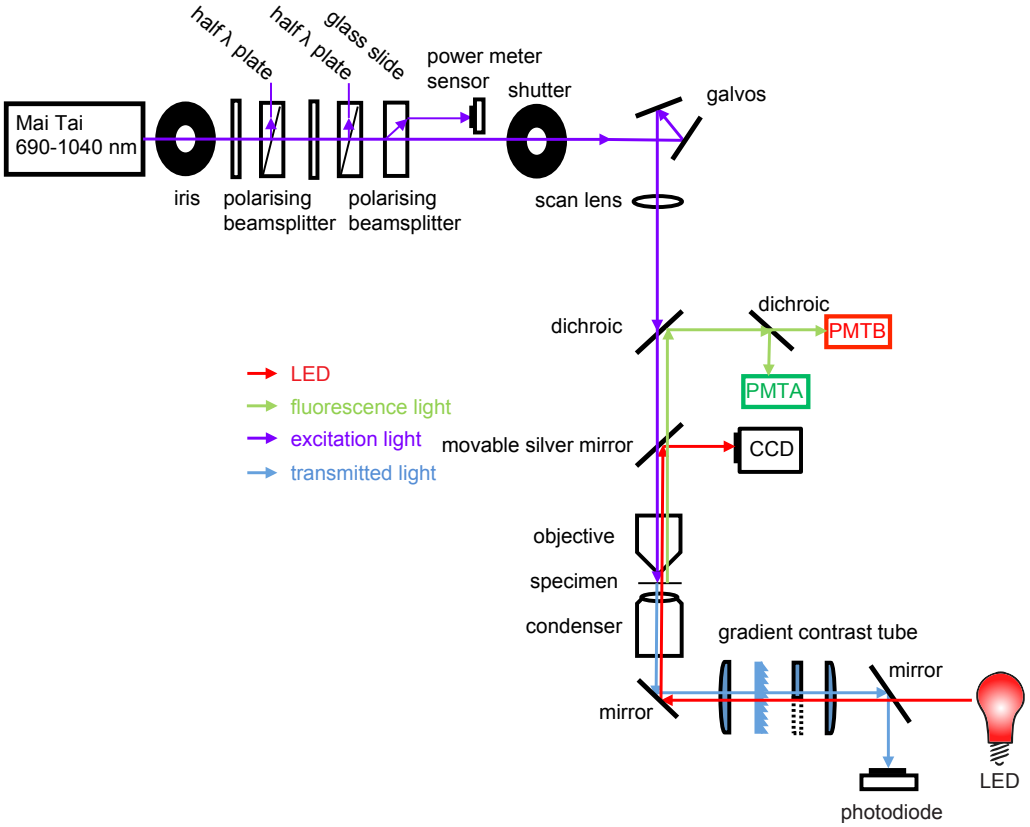

Figure 2.1: **Schematic diagram of the two-photon microscope.** For a detailed description refer to the text. The PMTs (A and B) are coloured to represent the colour of the detected fluorescence light.

2.3.2 Cell identification

I first located the visual cortex using the 4x objective. Having switched to the 40x objective, the primary visual cortex was identified based on the presence of a granular L4. Cortical L5 was found below this layer and identified by the presence of large PCs with triangular somata (around 10–20 μm in diameter) and thick ascending apical dendrites.

For slices from PV and SOM mice, the Ti:Sa laser was tuned to 870–890 nm in order to obtain an appropriate excitation wavelength. INs in L5 were identified by their EGFP expression (the presence of a signal on the green PMT channel). To adjust sensitivity, the PMT high-voltage power supply was varied to between 700 and 1000 V. Using a 40x objective, GFP-expressing cells were imaged using ScanImage at different magnifications (zoom 1 to 3). Once a suitable EGFP-expressing cell was located (i.e one in L5 that was not too close to the slice surface, allowing preservation of neurite aborisation), a z-stack was acquired (2 ms/line over 512 x 512 pixels and 2 μm steps in the z-direction). The slow line speed resulted in a prolonged pixel dwell time, improving the signal-to-noise ratio. Three images were acquired per slice and averaged to further reduce background noise. Stacks were processed in MacBiophotonics ImageJ (www.macbiophotonics.ca). The EGFP-expressing cell of interest was 'marked' in the laser scanning Dodt contrast z-stack, allowing selection of the same cell in the live IR CCD camera image for patching (see Figure 2.1).

For slices from non-transgenic animals, BCs were selected based on their small round somata (roughly 8–10 μm). MCs were targeted based on their ovoid, non-pyramidal appearance of their somata (typically larger than BCs but smaller than PCs) and the absence of the thick ascending apical dendrite characteristic of PCs.

In all recordings, the internal solutions (see Tables 2.2) contained 30–40 μM Alexa Fluor 594 to allow full morphological visualization and reconstruction. After achieving whole-cell configuration (see section 2.5) a minimum of 30 minutes was allowed to provide enough time for thinner and more distal structures to be filled before the cell was imaged. The Ti:Sa laser was tuned to 820 nm for the optimal excitation wavelength of Alexa Fluor 594 for 2PLSM. The fluorescence collection was made via the

red PMT channel. The filled cell was imaged by acquiring a z-stack using ScanImage (2 ms/line over 512 x 512 pixels and 1 or 2 μm steps in the z direction). In order to reduce noise, each slice depth was an average of three captured frames. The laser power was initially set to low, then gradually increased deeper into the slice – compensating for light scattering in the slice. Correct cell targeting was verified by comparing the Alexa Fluor 594 and GFP stacks. For illustration, maximum projection images of cells were generated, 3D-median filtered and pseudo-coloured using ImageJ.

Appropriate cell targeting was confirmed by morphological and electrophysiological analysis (see sections 2.4 and 2.5).

2.4 Analysis of cell morphology

2.4.1 Fluorescence reconstruction

To create reconstructions of neurons from 2PLSM imaging, multiple z-stacks were made to capture each neuron's entire fluorescence signal. The resulting stacks had brightness and contrast adjusted in ImageJ and were saved as 16-bit .tiff files. Registration of the stacks and manual 3D reconstruction of each neuron was carried out using Neuromantic version 1.6.3 (http://www.reading.ac.uk/neuromantic/) (Myatt et al., 2012). Different labels were assigned to somatic/axonal and dendritic segments. The resulting reconstructed morphologies were saved as .swc files. In addition, to locate each cell in relation to the neocortical layer boundaries, fluorescence stacks and laser-scanning Dodt-contrast stacks were overlaid. Layer boundaries were identified through the presence of large PC somata in L5, a slightly thinner and darker granular L4, and an L1 that generally lacked cell bodies. Also the boundary of the overlaid laser-scanning Dodt-contrast stacks for each cell were marked to identify the extent of each neuron. The resulting .swc files were saved in the same coordinate space as the corresponding reconstruction. Scaling (pixels/μm) was determined from the image of a graticule. In the rare case that *post-hoc* analysis of the Dodt contrast stacks revealed incorrect cell position (e.g. in L4 or L6), the neurons were discarded without further analysis.

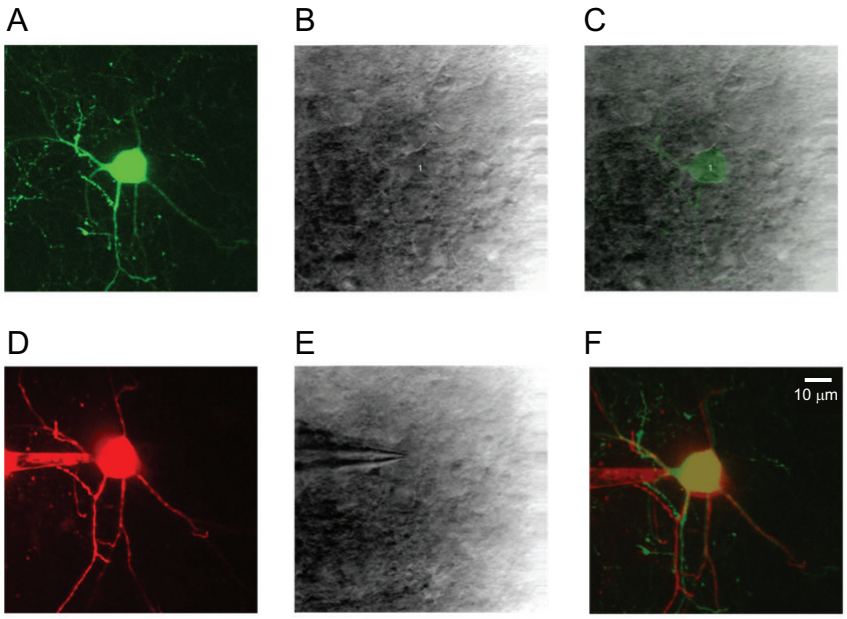

Figure 2.2: **Targeted patching of a GFP-expressing cell.** (**A**) Image of a visual cortex L5 GFP-expressing IN in a slice from a P19 mouse ('SOM' line). (**B**) Corresponding laser scanning Dodt contrast image. (**C**) The GFP image overlaid with its Dodt contrast image. (**D**) The same IN as in A, filled with Alexa-594 from the patch electrode. (**E**) The laser scanning Dodt contrast image with the patch electrode. (**F**) An overlay of the GFP and Alexa-594 images.

2.4.2 Morphometric analysis

Quantitative analysis of the reconstructions was performed using in-house custom software 'qMorph' written in Igor Pro. Reconstructions were slighty rotated about the soma to align the image with the pia horizontal and at the top and centered on the L4/5 boundary (Buchanan et al., 2012). The morphometric analysis of the reconstrutions consisted of the creation of density maps, convex hulls and Sholl analysis (Sholl, 1953). Density maps were created, having each compartment of a reconstruction of a cell represented by a two-dimensional Gaussian aligned on its XY center, with its amplitude proportional to compartment length and standard deviation set to a constant 25 µm. For each cell, these Gaussians were summed to create a smoothed 2D projection of the morphology cross-section (density map). The density map of each individual reconstruction was normalized, to enable averaging across reconstructions. Within each individual cell, axons and dendrites were density-mapped separately. Ensemble maps were normalized, gamma-corrected to visualise weaker densities, assigned colour lookup tables (yellow-to-white for the axons and magenta-to-white for the dendrites) and merged by a logical OR. The resultant coloured density maps are thus in arbitrary units and the appearance of symmetry in density maps is a result of mirroring of reconstructions. However all statistical comparisons were carried out on non-mirrored data.

The convex hull of a neuron determines the outline of the neuron by connecting the tips of the processes of the cell (Kawa et al., 1998). Convex hulls of individual reconstructions were generated separately from 2D projections of the axonal and dendritic arbours using qMorph, using the gift-wrapping algorithm (Jarvis walk). Sholl analysis (Sholl, 1953) is a classical method of quantitative analysis to characterise cell morphology based on counting the number of neurites crossing a series of circles (centered on the soma) with increasing radii. Sholl analysis was implemented in qMorph by realigning reconstructions on somata, using radial coordinates to move in 6.5 µm steps from $r = 0$. Sholl diagrams were averaged without normalisation.

2.5 Electrophysiology

Whole-cell recording pipettes were pulled from 1.5 mm o.d. medium-walled borosilicate capillaries (G150F-4; Warner Instruments) using a horizontal electrode puller (P-97; Sutter Instruments). The electrodes were filled with an internal solution containing (in mM): 5 KCl; 115 K-gluconate; 10 K-HEPES; 4 MgATP; 0.3 Na_3GTP; 10 Na-phosphocreatine and 0.1% w/v biocytin, adjusted with KOH to pH 7.3. Using the Nernst equation, the chloride reversal potential was calculated as –86.4 mV. For certain voltage-clamp recordings, a different solution was used. This contained (in mM): 100 Cs-gluconate; 5 CsCl; 10 HEPES; 8 NaCl; 0.2 EGTA; 2 MgATP; 0.3 Na_3GTP; 20 K_2 ATP; 10 Na-phosphocreatine; 5 QX-314 chloride (adjusted to pH 7.3 with CsOH). The chloride reversal potential was calculated to be –52.7 mV. To account for the extracellular fluid osmolality of mice (see, for example Bourque, 2008) the extracellular recording solution (see section 2.2) was adjusted to 338 mOsm using dextrose and the internal solutions were adjusted to 310 mOsm using sucrose. Measurements were made using a freezing-point osmometer (Model 3320; Advanced Instruments Inc.). Although these values are higher than those typically used for recordings of cells from rats (Sjöström et al., 2001), they gave reliable high quality recordings. The internal solutions were stored as frozen 1 ml aliquots and 20–40 μM Alexa Fluor 594 was added immediately before use. Internal solutions were filtered through a 0.2 μm syringe-tip filter (176-0020; Nalgene) and applied through a MicroFil 28 gauge micropipette (World Precision Instruments). The pipette glass contained an internal filament allowing the solution to rapidly flow down to the pipette tip by capillary action.

The patch pipette was mounted in a ISO-S-1.5G electrode holder (G23 Instruments) connected to the current- and voltage-clamp headstage (CV-7B; Molecular Devices) of a patch-clamp amplifier (Multiclamp 700B; Molecular Devices), which controlled the electrode potential and amplified current and voltage signals. The electrode holder served three important functions. (1) It provided electrical connection to the pipette via a silver wire coated in AgCl; the Ag/AgCl interface allowed the flow of ions in the solution to be converted to a flow of electrons in a copper wire. (2) It allowed the application of positive and negative pressure to the back of the pipette. (3) It provided a mechanically stable mounting for the electrode. Stability of electrodes dur-

K-gluconate internal solution		
Compound	Concentration (mM)	Source
KCl	5	Sigma
K-gluconate	115	
(from D-gluconic acid + KOH)		Sigma
HEPES	10	Sigma
MgATP	4	Sigma
Na_3GTP	0.3	Sigma
Na-phosphocreatine	10	Sigma
biocytin	0.1% (w/v)	Sigma

Cs-gluconate internal solution		
Compound	Concentration (mM)	Source
CsCl	5	Sigma
NaCl	8	VWR
Cs-gluconate	100	
(from D-gluconic acid + CsOH)		Sigma
HEPES	10	Sigma
MgATP	2	Sigma
K_2ATP	20	Sigma
Na_3GTP	0.3	Sigma
Na-phosphocreatine	10	Sigma
EGTA	0.2	Sigma
QX-314 chloride	5	R&D Systems

Table 2.2: **Composition of internal solutions.** The pH of the solution was adjusted to 7.3 with KOH or CsOH respectively. The osmolality for both solutions was adjusted with sucrose to obtain 310 mOsm. Alexa Fluor 594 10–40 μM were added immediatley before use. TEA (5 mM) was added in RI experimental condition.

ing patch-clamp recording is essential but movement often occurs during changes in pipette pressure. This is typically most problematic when applying suction in order to rupture the patch of membrane beneath a cell-attached electrode to enable whole-cell recording (see below). The holder minimised such movement by supporting the electrode at two points with rubber O-rings at either end of an internal polycarbonate cylinder. To complete the circuit, a AgCl pellet bath electrode was connected to the rear of the headstage. The headstage was mounted on motorised micromanipulator (PatchStar; Scientifica). Signals were displayed on an oscilloscope (TDS 2042B; Tektronix) and digitised using a PCI-6229 A-D board (National Instruments) using custom software (Sjöström et al., 2001) running in Igor Pro 6.

To obtain the whole-cell configuration (Hamill et al., 1981), the recording pipette was lowered into the recording chamber and visualized with the 40x objective above the plane of the slice. To keep the pipette tip clear of debris that might impede seal formation, positive pressure was applied to the electrode before immersion into the bath solution (Edwards et al., 1989). In the voltage-clamp configuration, a –5 mV 'seal' test pulse was applied at 50 Hz using the Multiclamp Commander (Molecular Devices). Pipette offset was adjusted to 0 pA and fast capacitance was nulled. Electrode resistance (typically 3–6 MΩ) was determined from the current response to the voltage step. The seal formation between the pipette and the cell membrane was monitored according to changes in the electrode resistance. When the electrode was moved towards the cell, an expanding dimple on the cell membrane was observed. This contact with the cell coincided with an increase in the tip resistance. The positive pressure was taken off and a gentle suction (negative pressure) was applied to increase the seal between the cell membrane and the electrode (Suchyna et al., 2009). The holding potential was slowly brought from 0 mV to –65 mV and the holding current was monitored until a seal of 5–10 GΩ (equivalent to holding current of 6.5–13 pA) was achieved. To gain electrical access to the cell, the membrane was ruptured by applying a slow ramp of suction. Successful access to the cell was indicated by the sudden appearance of capacitance transients (reflecting the 'newly added' cell membrane) and a drop in resistance (see section 2.5.2).

For each electrophysiological recording, the bath and pipette electrode were in con-

tact with solutions of different ionic composition. This produced a source of a steady potential difference between the two electrodes that is termed the liquid junction potential. This liquid junction potential introduces errors to true measurements of the membrane potential. The introduced potential difference depends on the difference in ionic charge between the internal and external solutions as well as the relative mobility of ions (dependent on the relative size of each individual ion) (Barry and Lynch, 1991; Barry, 1994). For the K-gluconate internal solution the liquid junction potential was directly measured as –9.3 mV, whereas for the CsCl internal solution it was –10.7 mV. The liquid junction potential was determined by filling the recording pipette with internal solution, lowering it into the bath that contained the same internal solution, zeroing the pipette offset then exchanging the solution in the bath for external solution and recording the change in voltage. In line with previous work (Buchanan et al., 2012), voltages in current-clamp recordings were not corrected. However, corrections were applied when calculating rectification index (see Chapter 4).

2.5.1 Current-clamp recordings

All current-clamp recordings were made with the K-gluconate internal. After establishing the whole-cell recording in voltage-clamp mode, the amplifier was switched to current-clamp mode and the resting membrane potential was noted (with no current injection). During recordings, the command current, bath temperature and membrane potential were continuously monitored. Signals were were filtered at 10 kHz and acquired at 20 kHz. To determine properties of the cell and its firing behaviour (including action potential height, threshold, half-width and after hyperpolarisation as well as firing rate accomodation; see section 2.6.1), current steps (500 ms-long) were injected, from –200 to +700 pA at 40 pA increments. The input resistance was monitored throughout the recording by measuring the steady-state membrane potential change in response to a 250 ms 25 pA hyperpolarising current step applied at the start of each recorded sweep. Cells were only included if their resting potential was more hyperpolarised than –60 mV and if they exhibited overshooting action potentials.

2.5.2 Voltage-clamp recordings

To record membrane currents the amplifier was switched back to voltage-clamp mode. In this mode a current-following operational amplifier in the headstage maintains a set potential difference (V_c) between the pipette and bath electrode by injecting current (I_p) that is proportional to, but with a reversed polarity to, fluctuations in the membrane current. Changes in membrane current are measured as the voltage drop across a feedback resistor (R_f) (see Figure 2.3). Because the current follower 'clamps' the end of the electrode (not the membrane potential), current flow accross the series resistance (R_s) causes a voltage drop. This effective resistance, the sum of the pipette resistance and the access resistance (the resistance of the access between the pipette and the cell) is always larger than the open pipette resistance, due to intracellular debris that partially occludes the pipette tip. In my recordings, the series resistance was typically ~8–15 MΩ. Also, the presence of the cell capacitance (C_m) in series with R_s acts as a low-pass filter (time constant $\tau \approx R_s C_m$) that slows down any changes in recorded membrane current. To minimise the voltage errors and unwanted filtering caused by the interaction of the series resistance and cell capacitance, I used electrodes of low resistance (see section 2.5) and used series resistance compensation to effectively reduce this resistance further.

As described above, a –5 mV test pulse was applied. The resulting fast pipette capacitance transient (from C_p in Figure 2.3) was nulled prior to patch rupture. On breakthrough into the whole-cell mode, the whole-cell capacitance transients were also nulled. Both processes were achieved by adjusting amplifier circuits that couple the command voltage via a variable resistor and capacitor in series (amplifier filter set at 10 kHz). This allowed a capacity current equal to the current needed to charge C_p or C_m to bypass the amplifier. These adjustments are cosmetic in that they do not change anything at the cell, but simply affect the output signal. However, they help prevent amplifier saturation (and oscillation) and provide an estimate of the series resistance that the amplifier uses for the subsequent series resistance compensation. I compensated for series resistance by adjusting the correction positive feedback circuit in the headstage, which introduces an additional current into the cell (a fraction of the output is added to the command potential). As current and resistance are inversely related

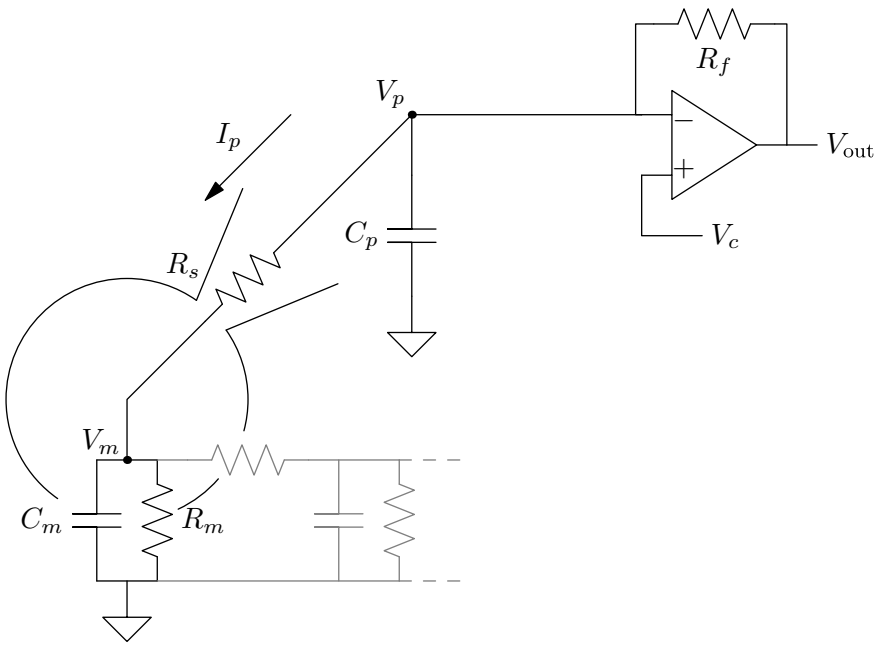

Figure 2.3: **Equivalent circuit diagram of a whole-cell voltage-clamp recording**. The single capacitor and resistor for the equivalent circuit of a one-compartment cell are shown in black – the additional capacitor and resistor in grey indicate the more realistic equivalent circuit for a neuron with somatic and dendritic compartments. Abbreviations: C_{m} membrane capacitance*;* C_{p} pipette capacitance; I_{p} electrode current; R_{s} series resistance (pipette resistance plus access resistance); R_{f} feedback resistor; R_{m} membrance resistance; V_{c} command voltage; V_{m} membrance voltage (modified from Barbour, 2011).

according to Ohm's law, the correction effectively reduces the series resistance. The amount of current injected by the amplifier was adjusted as a percentage of the series resistance determined during the *RC* adjustment. In practice, after cancellation, the *RC* circuit was turned off and I applied as much correction as possible before the capacitive current shape began to distort – a prelude to 'ringing' (oscillation due to overcompensation of the positive feedback). Typically, I achieved between 50 and 80% compensation. This was periodically checked throughout the recording and care was taken to note any changes in series resistance as indicated by altered background current noise. Recordings were rejected if the (uncompensated) series resistance increased above 25 MΩ or altered by >30%. The typical BC whole-cell capacitance of ~20 pF and uncompensated series resistance of 4 to 19 MΩ gave a lowpass corner frequency of ~0.5 kHz to 2.4 kHz. The typical MC whole-cell capacitance of ~16.5 pF and uncompensated series resistance of 5 to 23 MΩ gave a lowpass corner frequency of ~0.6 kHz to 2 kHz.

Whole-cell recordings of mEPSCs were acquired at various holding potentials, in the presence of 20 μM D-AP5, 20 μM 2-(3-carboxypropyl)-3-amino-6-(4 methoxyphenyl) pyridazinium bromide (SR-95531), 1 μM [*S*-(*R**,*R**)]-[3-[[1-(3,4-dichlorophenyl)ethyl]amino]-2-hydroxypropyl](cyclohexylmethyl) phosphinic acid (CGP 546-26) and 500 nM tetrodotoxin (TTX). The current was filtered at 4 kHz and sampled at 20 kHz. Two groups of recordings were obtained: (1) following assessment of firing properties, mEPSCs were recorded at various negative membrane potentials using the K-gluconate internal (see Table 2.2), and (2) to allow recording of mEPSCs at positive voltages, a Cs-gluconate internal was used (see Table 2.2). In most cases, to allow recordings at positive membrane voltages, TEA was added to the external recording solution (4 mM) and the internal solution (5 mM).

All intracellular solutions, except those used in control recordings for mEPSC rectification or in assessing Naspm block (see Chapter 4), contained spermine. For experiments examining mEPSC rectification, recordings were made in the absence and presence of intracellular spermine using a Cs-gluconate internal solution. In the former case, no spermine was added and endogenous polyamines were buffered with 20 mM K_2ATP (Rozov et al., 2012). In experiments examining Naspm block of mEPSCs

(see Chapter 4) I used a K-gluconate solution without added spermine (but with no additional ATP buffering). In all other recordings a free spermine concentration of ~40 μM was used. To achieve this, 500 μM spermine tetrahydrochloride was added to the Cs-gluconate internal solution (containing high K_2ATP) and 100 μM was added to the K-gluconate solution (Rozov et al., 2012). Individual sweeps of 10 s duration were acquired every 10 or 15 s. To assess potential changes in series resistance, a –5 mV step was applied at the start of each sweep.

2.6 Analysis of electrophysiological data

2.6.1 Current-clamp analysis

Voltage records were analyzed using in-house software routines in Igor Pro (Buchanan et al., 2012). The following values were determined:

- Resting membrane potential (V_m; mV) was taken from the mean of the first 50 ms of the average of all sweeps (typically 12) in the recording.
- Input resistance (R_i; MΩ) – the sum of membrane resistance (R_m) and the series resistance (R_s) – was determined from the average wave, as the maximal voltage deflection/the –25 pA current injection.
- Membrane time constant (τ_m; ms) was measured from an exponential fit to the average voltage deflection in response to the –25 pA current injection at the start of each sweep (ignoring any initial deflection due to the series resistance).
- 'I_h measure' – a measurement of the 'sag' (a delayed depolarisation) in the voltage response to a step hyperpolarising current injection, reflecting the presence of hyperpolarisation-activated cyclic nucleotide-gated (HCN) channels underlying the I_h current (McCormick and Pape, 1990; McCormick and Huguenard, 1992) – was calculated from the voltage response to the first (most negative) current injection.

- Spike threshold (mV) was determined from the first spike in the rheobase sweep (the first current injection for which spikes were generated). lt was calculated as the minimum voltage of the inflection point determined by subtracting the spike waveform from a straight line fit to the rising phase of the spike. This method was chosen as it is a more reliable method than using a pre-defined threshold of the second derivative of the spike.

- Spike height (mV) was taken as the difference between spike threshold and spike peak for the first spike in the rheobase sweep.

- Spike half-width (ms) was the width of the spike at half height for the first spike in the rheobase sweep.

- Spike afterhypolarisation (AHP) (mV) was measured from the spike threshold to the post-spike minimum for the first spike in the rheobase sweep.

- Mean frequency at rheobase (Hz) was calculated as the number of spikes evoked at rheobase/duration of the injected current.

- Mean frequency at ~1.5x rheobase (Hz) was calculated as above but for the current injection closest to 1.5x the rheobase current.

- Accommodation (%) was calculated as –((1-min ratio of instantaneous frequency) * 100), where 'ratio of instantaneous frequency' was determined from the ratio of the instantaneous frequencies (1/inter-spike interval) for the first- and last spike pairs of each sweep.

2.6.2 Miniature current detection and analysis

mEPSCs were detected using NeuroMatic software (version 2.8q; J. Rothman UCL) running in Igor Pro. For detection only, the records were digitally filtered (low-pass Butterworth, 2 kHz). Events were detected using either threshold-crossing (Kudoh and Taguchi, 2002) or template-matching (Clements and Bekkers, 1997) methods, as discussed in Chapter 4. Initially, baseline noise (current standard deviation; SD) was assessed by fitting a 'one-sided' Gaussian to an all-point histogram of a selected 250–300 ms long section of the record. For records with negative-going mEPSCs (e.g. at

–60 mV), the fit was performed using the positive half of the histogram only, enabling an accurate determination of the background noise (see Figure 2.4). For each recording voltage, this procedure was repeated 5 times and the average SD taken as the measure of background noise for that recording. For threshold-crossing detection, I variously employed an amplitude threshold that was either 2.5 x SD or a fixed value (detailed in Chapter 4).

For template-matching, a waveform template, with a time course typical of a synaptic event, was first matched to the current (Clements and Bekkers, 1997). In effect the template was slid along the recording one sample point at a time, offset and multiplied by a scaling factor so as to minimize the sum of squared errors (SSE) between the fitted template and the actual current at each position (fitted template = template * scale + offset). The SSE was used to determine a standard error, from which a 'detection criterion' was calculated as scale/standard error. This produced a continuous detection criterion wave, reflecting the similarity of the record to the template. An mEPSC was then detected when this detection criterion transiently crossed a defined level. For a correctly aligned mEPSC, the scale measure approximated the peak amplitude of the event, while the standard error approximated the noise SD. Thus, the detection criterion was closely linked the signal-to-noise ratio for the detected event. In their testing of this approach, Clements and Bekkers (1997) concluded that a default value "provides close to optimum detection sensitivity while ensuring a low rate of spurious events (false positives)". Importantly, the threshold setting was shown to be largely independent of the background noise level, meaning that within limits the algorithm attempts to "automatically adjusts to compensate for changes in recording noise".

The templates used were unique to each cell and consisted of a pre-event baseline followed by an exponential rise and decay:

$$\text{Template}(t) = 0 \;\; (t \leq 0)$$

$$\text{Template}(t) = (1 - exp(-t/\tau_{\text{Rise}}))exp(-t/\tau_{\text{Decay}}) \;\; (t > 0) \tag{2.1}$$

For MCs, for example, mEPSC templates were 9 ms long with a 3 ms baseline before the event; I used rise time constants of 0.2–0.4 ms (mean 0.35 ms) and decay time

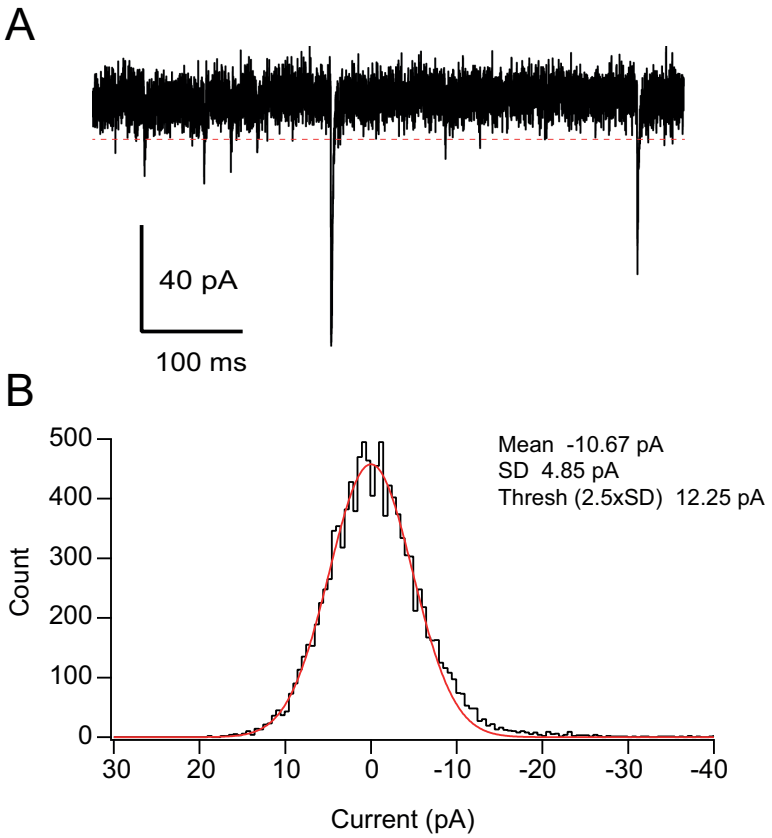

Figure 2.4: **Assessment of 'background' noise.** (**A**) A short section of mEPSC recording (–60 mV) from a visual cortex L5 BC in a slice from a P19 PV mouse. Red dotted line indicates the threshold of 12.25 pA. (**B**) All-point histogram (black) of the trace shown in A, with superimposed one-sided Gaussian curve (red) fit only to left-hand side of the histogram (from +30 to –2 pA). For display, the histogram has been centered on 0 pA. The values from the fitted Gaussian and the calculated mEPSC threshold for 2.5 x SD ('Thresh') are shown.

constants of 1–5 ms (mean 4 ms). Typically I used a detection threshold of 3 or 4.

Following their detection, individual events were extracted from the continuous sweeps and visually inspected. Detected events were rejected if they reflected noise or artefactual transients. Mean rates were determined by dividing the total number of events detected by the length of the recording. The peak amplitude, 20-80% rise time and 37% decay of each event was measured. To reduce error in estimating the risetime, peak, and decay of noisy mEPSCs, individual events were fitted with an empirical equation of the form $m^x h$:

$$f(t) = (1 - exp(-(t - t_0)/\tau_{\text{Rise}}))^N * (A1 * exp(-(t - t_0)/\tau_{\text{Decay1}} + A2 * exp(-(t - t_0)/\tau_{\text{Decay2}})) \tag{2.2}$$

where τ_{Rise}, $\tau_{\text{Decay1}}$and τ_{Decay2} are rise and decay time constants, $A1$ and $A2$ are amplitudes of the two decay components and N is a variable exponent. The measurements (amplitude, 20-80% rise time and 37% decay) were then taken from the fitted curves (Bekkers and Stevens, 1996; Bekkers and Clements, 1999) (see Figure 2.5).

Analysis of mEPSC statistics at different voltages and calculation of mEPSC rectification (see Chapter 4) was performed using custom routines in R (version 3.0.2, The R Foundation for Statistical Computing, http://www.r-project.org/) using RStudio (version 0.98, RStudio, Inc.). The decay of averaged mEPSCs was described by one or two exponential functions. When fitted with two exponentials, the weighted time constant of decay ($\tau_{\text{w, decay}}$) was calculated as the sum of the fast and slow time constants weighted by their fractional amplitudes.

2.7 Immunohistochemistry

2.7.1 Antibody labelling

Antibody labelling was performed using cortical slices from mice at P21. To ensure a rapid and consistent fixation of brain tissue necessary for high quality immunohis-

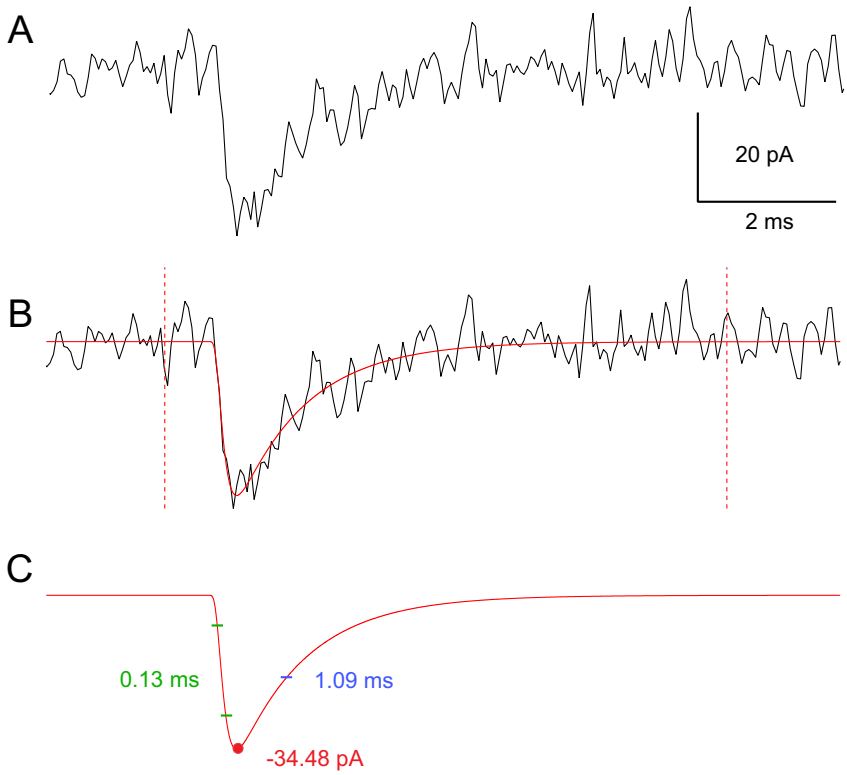

Figure 2.5: **Example of the fitting of an mEPSC to facillitate measurement of peak, rise, and decay.** (**A**) An example mEPSC from the same recording as shown in Figure 2.4. (**B**) Red trace shows fit equation 2.2 between dashed lines. (**C**) Amplitude and kinetic measurements from the fitted waveform.

tochemical reactions (Fritschy, 2008; Lorincz and Nusser, 2008), mice were anesthetized with isoflurane and transcardially perfused with 0.1 M PBS (pH 7.4) followed by 4% paraformaldehyde. This was done with the assistance of Dr Marzieh Zonouzi. The mice were decapitated and the brains removed. The brains were checked for appearance (white/yellow colour) and consistency (firm), indicating effective perfusion. Cortical tissues were postfixed overnight in 4% paraformaldehyde and placed in 30% sucrose solution, this was later changed to 10% sucrose solution.

Serial coronal sections containing the visual cortex (40-50 μm thick) were cut using a sliding microtome (HM 450; Thermo Scientific) and collected in PBS. These free-floating sections were incubated (4°C, up to 48 hours) with various primary antibodies (see Table 2.3) in blocking solution containing 20% NGS, 1% BSA and 0.5 % Triton. Free-floating sections were then washed with carrier solution (2% NGS, 1% BSA and 0.5 % Triton) 4 x 15 minutes and incubated with various secondary antibodies (see Table 2.4) at room temperature for 1 h in the same solution. After 3 further 15 minute washes, slices were incubated in diamidino-2-phenylindole (DAPI) (1:1000; Molecular Probes) at room temperature for 10 minutes, washed once for 15 minutes in PBS and then mounted on coverslips and kept frozen in the dark before imaging. Primary and secondary antibodies were initially tested for optimal dilution, with reference to previously published studies (Antonucci et al., 2012; Cammalleri et al., 2009; Fukaya et al., 2006; Gonchar et al., 2007; Huang et al., 2013; León-Espinosa et al., 2012; Massi et al., 2012; Shimuta et al., 2001; Xu et al., 2006). Additionally, the number of washes, and the temperature of various incubations were varied in order to maximise the signal-to-noise ratio (minimise background labelling). To control for fluorescence crosstalk, fluorphores were selected carefully and imaged sequentially.

2.7.2 Confocal microscopy

Mounted sections were imaged with a confocal microscope (Leica SPE). A confocal microscope was used as this captures light only from the plane of focus, reducing

Primary antibodies

Description	Source	Number	Species	Type	Dilution
anti-PV	Swant	235	mouse	monoclonal	1:500
anti-PV	Synaptic Systems	195-004	guinea pig	polyclonal	1:200
anti-SOM	Millipore	MAB354	rat	monoclonal	1:100
anti-GluA2	Frontier Institute	GluR2C-Rb-Af1050	rabbit	polyclonal	1:200-250
anti-GFP	Roche	11814460001	mouse	mixed monoclonals	1:250

Table 2.3: **Details of primary antibodies used for immunolabelling.**

Secondary antibodies

Description	Source	Number	Excit./Emis. (nm)
Alexa Fluor 555 Goat Anti-Rat IgG	Life Technologies	A-21434	555/565
Alexa Fluor 647 Goat Anti-Rabbit IgG	Jackson Immuno Research	111-175-144	651/667
Alexa Fluor 647 Goat Anti-Guinea Pig IgG	Life Technologies	A-21450	650/668
Alexa Fluor 488 Goat Anti-Rabbit IgG	Life Technologies	A-11008	488/519
Alexa Fluor 647 Goat Anti-Mouse IgG	Life Technologies	A-21236	650/668
Alexa Fluor 488 Goat Anti-Mouse IgG	Jackson Immuno Research	115-545-062	493/519
Alexa Fluor 647 Goat Anti-Rabbit IgG	Jackson Immuno Research	111-175-144	651/667

Table 2.4: **Details of secondary antibodies used for immunolabelling.** Abbreviations: Excit./Emis. excitation and emission wavelengths. All antibodies were used at a dilution of 1:250. Note, all secondary antibodies were raised in a species (goat) different from that in which primary antibodies were raised.

blur (out-of-focus light), allowing specimens to be optically sectioned and an arbitrary number of such optical sections collected into a z-stack representing the 3-D structure. The key feature of a confocal microscope is a pinhole to restrict the collection of out-of-focus light by the detector (in this case a photomultiplier tube; PMT). The tissue was illuminated (as appropriate for the antibody) by light from four low-noise, solid-state lasers, which were used to provide excitation lines of 405, 488, 561 and 635 nm. For each fluorophore a suitable emission range was specified and laser power and gain were adjusted (Leica Application Suite, Advanced Fluoresence software version 2.3.6). Fluorophores were chosen to have non-overlapping emission spectra and no bleed through was observed between channels. The following combinations were used; DAPI 488ex/405-455em, GFP 488ex/500-545em, anti-GluA2 488ex/500-550em, anti-GluA2 635ex/650-800em, anti-SOM 532ex/560-640em, anti-PV 635ex/650-800em, anti-PV 488ex/500-550em, Anti-GFP 635ex/690-800em.

The SPE confocal had one PMT, so all multi-channel acquisition was done sequentially and subsequently merged for analysis. To change the focus when optically sectioning the samples, a galvanometer-driven stage insert was used to provide specimen scanning (z-step 1 μm). Fluorescent light emitted by the illuminated tissue was collected by a 10x, 20x or 63x objective (10x Air ACS APO 0.3NA; 20x Multi ACS APO 0.6NA; 63x Oil ACS APO 1.3NA). To avoid photobleaching (irreversible chemical reactions of the fluorophore molecule resulting in a dramatic reduction of the fluorescence light intensity after a short period of exposure) I attempted to minimise the tissue exposure to high intesity excitation and exposed the tissue for no longer than necessary. Settings and gains were kept invariant between samples and images (1024 x 1024 pixels) were saved as .tiff and .lif files.

2.7.3 Analysis of antibody labelling

Analysis of antibody labelling was performed manually using Fiji (Schindelin et al., 2012) (ImageJ 2.0.0). In each individual image stack, layer 5 boundaries were identified by the presence of labelled PCs in the GluA2 channel and, if present, by large PC cell bodies surrounded by PV-immunoreactive puncta when viewed in the PV channel.

To quantify fluoresence intensity across labelled cells (PV, SOM, GluA2, GFP), the mean grey value in selected regions of interest (ROIs; ~3 μm diameter) centered on the brightest regions of the cell body were measured. ROIs of the same area were used to determine the average mean grey background (minimum of 15 values for each stack). The GluA2 labelling in PCs was used to normalise the GluA2 intensity accross slices and animals. The quantitative observations gained with this method were always in accordance with my qualitative assessment of somatic fluorescence immunolabelling intensities when inspecting the images visually.

2.8 Statistics

Summary data are presented in the text as mean ± s.e.m. from n cells or animals. Comparisons involving two data sets only were performed using a two-sided Welch two-sample t test that does not assume equal variance. Analyses involving data from three or more groups were performed using one-way or two-way analysis of variance (ANOVA; Welch heteroscedastic F test) followed by pairwise comparisons using two-sided Welch two-sample t tests (with Holm's sequential Bonferroni correction for multiple comparisons). Correlations between data sets were determined using either Pearson's product-moment correlation test or Spearman rank order correlation test. Results were considered significant at $p < 0.05$. Statistical tests were performed using JMP (JMP®, Version 11.2.0. SAS Institute Inc.) or R (version 3.0.2, The R Foundation for Statistical Computing, http://www.r-project.org/) and R Studio (version 0.98.477 RStudio, Inc.).

Chapter 3

Morphometric characterisation of L5 IN classes

3.1 Introduction

The axonal and dendritic branching pattern of neurons reflects their function. These morphological features are also key in terms of neuronal classification. Certain neuronal types are morphologically relatively homogeneous (e.g. PCs; DeFelipe and Fariñas 1992) whereas other neurons are quite heterogeneous, with much less stereotyped anatomical features (e.g. INs; Markram et al. 2004). Certain INs can be precisely recognised only by their unique morphological characteristics (Markram et al., 2004). Regarding the classification of INs, one particularly important feature is the nature of the axonal arbor, specifically whether this is confined to a single layer ('intralaminar') or crosses multiple layers ('translaminar'). In fact, the most unambiguous identification of IN types comes from assessing the *full* extent of axonal aborisation – somatodendritic morphology alone is considered to be insufficient (Ascoli, 2008; DeFelipe et al., 2013).

Many techniques have been used to assess the shape of neurite branching. These include bulk dye loading (such as the Golgi method), intracellular injections (such as dyes or biocytin), and genetic labelling (Parekh and Ascoli, 2013). Visualization of the labelled neurons can be performed using bright-field-, confocal-, two-photon- or

superresolution microscopy (Lemmens et al., 2010; Parekh and Ascoli, 2013). Digital reconstructions gained by tracing the cell body, its axon and dendrites (sometimes including spines) convert the microscopic image into a quantitative representation of the neuron. Various commercial or free open-source software options are available to perform such semi-automatic, semi-manual, or manual tracing. These include, for example, tracing of biocytin labelled cells using Neurolucida (MBF Bioscience, Williston, VT, USA; Glaser and Glaser, 1990) or tracing from image stacks with Neuromantic (Myatt et al., 2012), Neuron_Morpho (Brown et al., 2005) or NeuronJ (Meijering et al., 2004).

Once digitally reconstructed, morphological data can be used for cell type identification (Ascoli, 2008), computer modeling/simulation (Blackman et al., 2014; Branco and Häusser, 2011), studies of morphology itself (Buchanan et al., 2012; Helmstaedter et al., 2009) or to link morphology to network connectivity (Gupta et al., 2000; Silberberg and Markram, 2007). The exponential rise in the number of publications describing digital reconstructions over the last 15 years or so has prompted the development of approaches such as NeuroMorpho.org (http://NeuroMorpho.org/), NeuronDB (http://senselab.med.yale.edu/neurondb/) or Open Source Brain, (http://www.opensourcebrain.org/), open archives giving access to a large pool of reconstructed neurons and models from published data (Crasto and Shepherd, 2007; Halavi et al., 2012). Such initiatives have contributed to the initiation of even larger projects such as the Human Brain Project (www.humanbrainproject.eu/) (Markram, 2013).

The aim of the morphological analysis described in this chapter was to allow identification of the different IN types (BCs and MCs) in layer 5 of the visual cortex from which I recorded mEPSCs (see Chapter 4). I made recordings from transgenic animals in which either PV- or SOM-expressing cells contained GFP (see Chapter 2) and from WT animals, in which I used soma shape to target BCs and MCs. The following sections outline the imaging and clustering approaches and the resulting IN classification.

3.2 2P Imaging

I imaged single Alexa-594-filled neurons with 2PLSM and carried out quantitative analysis of neuronal morphology by manually reconstructing each dye-filled IN using Neuromantic. 2P imaging allowed initial assessment of fine axonal morphology at the time of the experiment, and did not require histological processing or a dedicated set-up for neuronal reconstruction (as in Neurolucida). Before presenting the results of the morphometric analyses, I briefly outline of those principles of 2P microscopy relevant to its use for neuronal tracing.

Excitation of a fluophore (introduced into the neuron *via* a patch-pipette) requires the absorption of energy from a photon, excitation of the fluophore from its ground state to an excited state, followed by its rapid relaxation back to its ground state through the emission of a red-shifted photon. In comparison to a one-photon absorption event, the simultaneous absorption of two photons of twice the wavelength (half the energy per photon) brings the fluorphore into its excited state, with the emitted photon having the same wavelength as in the one-photon case. This phenomenon was described as early as 1931, but found its application to imaging biological specimens with 2PLSM only in 1990, made possible by the high local intensity provided by the ability to generate femtosecond pulses of red laser light (Denk et al., 1990).

2PLSM exhibits several beneficial features. The nature of two-photon interactions results in a quadratic dependence of the absorption (and thus the signal) on the excitation intensity – doubling the intensity gives four times the fluorescence. This feature, by allowing the use of lower intensity illumination, greatly reduces limitations of photobleaching; this leads to a lengthening of the available observation time. Also, as excitation is localised to the focal point (where photon density is the highest) thus there is a reduction in out-of-focus excitation (Denk et al., 1990). Since no fluorescence is generated outside of the vicinity of the geometrical focus (outside of the so-called focal volume), the sectioning effect makes pinhole-like detection, as in single photon excitation, unnecessary. All fluorescence photons contribute to the signal (Denk et al., 1990; Denk and Svoboda, 1997). With scattering being proprotional to λ^{-4}, one final advantage of two-photon microscopy over one-photon excitation lies in the reduced

scattering of the excitation light, which is in the red or infrared. Therefore, in strongly scattering specimens, imaging depths of more than 100 μm can be reached (Denk et al., 1994).

3.3 Cluster analysis of morphometric features

Initially, I wished to determine whether the recorded cells fell into distinct morphological subgroups comparable with those IN types previously decribed in the literature (Markram et al., 2004). Reconstructions of Alexa594-filled cells were carried out both by myself and by colleagues in Montreal. I reconstructed approximately one third of the 60 INs, the remaining reconstructions were carried out by Erica Gregor and Andrew Chung. In the later case, those performing the reconstructions were blind to the nature of the electrophysiological data (spiking pattern or mEPSC properties). Table 3.1 lists the measures derived from the reconstructions using qMorph (see Chapter 2). For illustration purposes, all 40 of the dendritic and axonal measures are shown in a dendrogram/heat map produced using Ward's hierachical clustering (see Figure 3.1 on page 72). Cluster analysis was performed using JMP (JMP®, Version 11.2.0. SAS Institute Inc.).

As illustrated in Table 3.1 on page 71 and Figure 3.1, cell morphology can be described by many diverse features. Although I considered interpreting the information from qMorph by using Principal Component Analysis, to group together INs with similar features, I instead chose to examine only selected axonal measures. This is because the pattern and extent of axonal aborisation are particularly relevant metrics of IN classification (DeFelipe et al., 2013). Specifically, I examined measures decribing the length of the longest axonal compartment (measure 11 in Table 3.1) and the maximal axonal y-excursion above L4 (measure 35 in Table 3.1). Figure 3.2A shows the results of Ward's hierachical clustering of the INs using the two axonal measures described. Figure 3.2B shows a scree plot of linkage distance versus cluster number and has a point for each cluster join. The number of major clusters was determined by the position at which the maximum increase in linkage distance was observed (a method first described in 1953 by Thorndike; Cauli et al. 2000; Helmstaedter et al. 2009).

This revealed two major groups; one was composed of fourteen cells, all of which were originally targeted as MCs, while the second contained 45 BCs and only one MC (recorded from the GIN line).

No.	qMorph measure	Description
1	AxonRelXCenter	X-coordinate of the density cloud centre – average of all compartment X-coordinates
2	AxonRelYCenter	As above, but for Y-coordinate
3	AxonCenterDist	Euclidean distance from 0,0 to density cloud center
4	AxonAngle	Angle to density cloud center from 0,0 (e.g to 1,0 = 0° and to 0,1 = 90°)
5	DendrRelXCenter	X-coordinate of the density cloud center – average of all compartment X-coordinates
6	DendrRelYCenter	As above, but for Y-coordinate
7	DendrCenterDist	Euclidean distance from 0,0 to density cloud center
8	DendrAngle	Angle to density cloud center from 0,0
9	maxAxonDistCompX	X-coordinate of the most distal (Euclidean distance) axonal compartment from 0,0
10	maxAxonDistCompY	As above, but for Y-coordinate
11	maxAxonDist	Euclidean distance to most distal axonal compartment
12	maxAxonDistCompAngle	Angle to the most distal axonal compartment
13	maxDendrDistCompX	X-coordinate of the most distal (Euclidean distance) dendritic compartment from 0,0
14	maxDendrDistCompY	As above, but for Y-coordinate
15	maxDendrDist	Euclidean distance to most distal dendritic compartment
16	maxDendrDistCompAngle	Angle to the most distal dendritic compartment
17	AxonHullCenterX	X-coordinate of axonal convex hull center
18	AxonHullCenterY	As above, but for Y-coordinate
19	AxonHullWidth	Maximum axonal convex hull width
20	AxonHullHeight	Maximum axonal convex hull height
21	DendrHullCenterX	X-coordinate of dendritic convex hull center
22	DendrHullCenterY	As above, but for Y-coordinate
23	DendrHullWidth	Maximum dendritic convex hull width
24	DendrHullHeight	Maximum dendritic convex hull height
25	percAxonAboveL5	Percent of axon hull above L5
26	percDendrAboveL5	Percent of dendritic hull above L5
27	AxonAreaAboveL5	Area of axon hull above L5
28	DendrAreaAboveL5	Area of dendritic hull above L5
29	SomaYCenter	Y-coordinate of soma centre
30	AxonMaxVal	Maximum number of axonal crossings for any sinlge measured radius in Sholl analysis
31	AxonCritR	Radius with maximum number of axonal crossings (maximum value) in Sholl analysis
32	DendrMaxVal	Maximum number of dendritic crossings for any single measured radius in Sholl analysis
33	DendrCritR	Radius with maximum number of dendritic crossings (maximum value) in Sholl analysis
34	extYAboveOrig	Extent of imaged area above 0,0
35	axonLenAboveL4	Total axon length above L4
36	dendrLenAboveL4	Total dendrite length above L4
37	maxAxonYAboveL4	Maximum axonal distance above L4
38	maxDendrYAboveL4	Maximum dendritic distance above L4
39	AxonAreaAboveL4	Area of axon hull above L4
40	DendrAreaAboveL4	Area of dendritic hull above L4

Table 3.1: **qMorph measures and their meanings**.

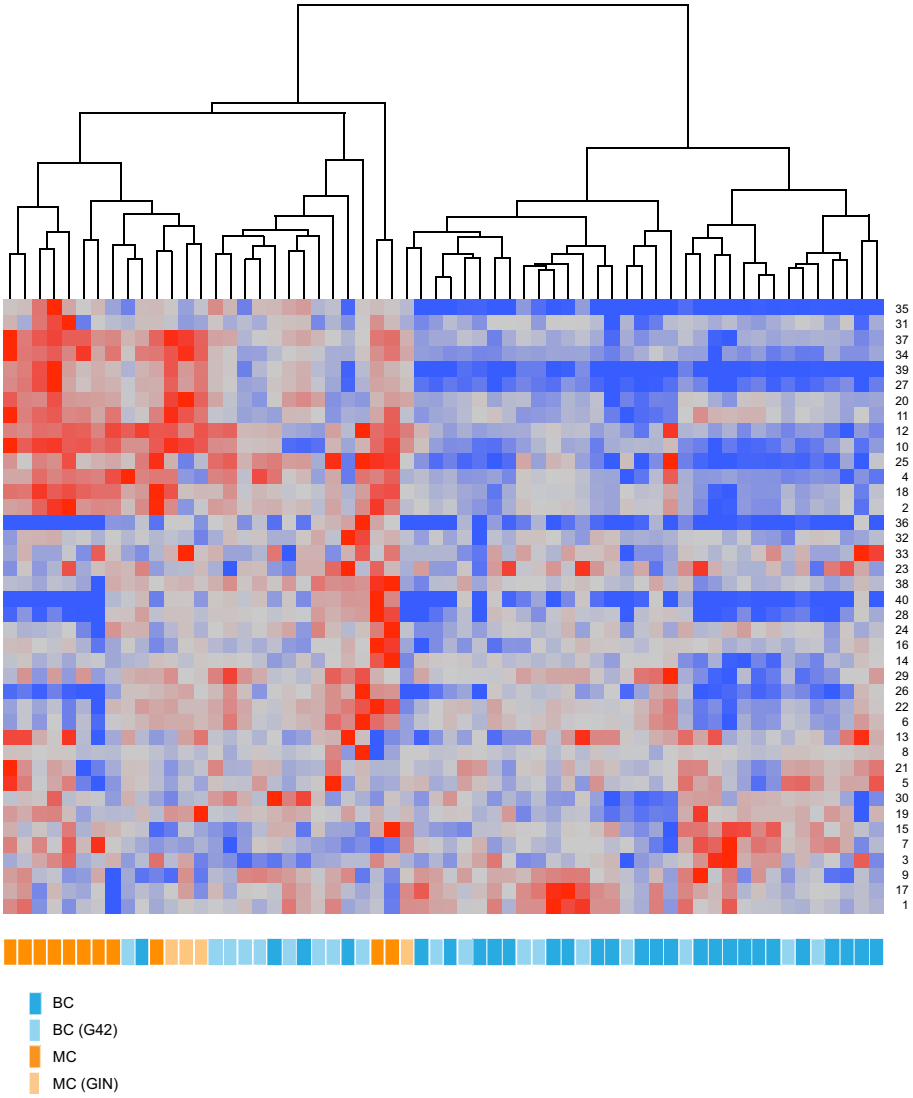

Figure 3.1: **Hierarchical clustering on all qMorph measures**. Illustrative dendrogram showing results of hierarchical cluster analysis (Ward's method). The x-axis represents the individual cells (colour-coded according to the original classification of targetted cells from transgenic lines and WT mice) and the dendrogram y-axis represents the within-cluster linkage distance (dendrogram branch scale proportional to within-cluster linkage distance). The blue-to-grey-to-red colour map indicates the values various measures (numbered from 1 to 60 as described in Table 3.1).

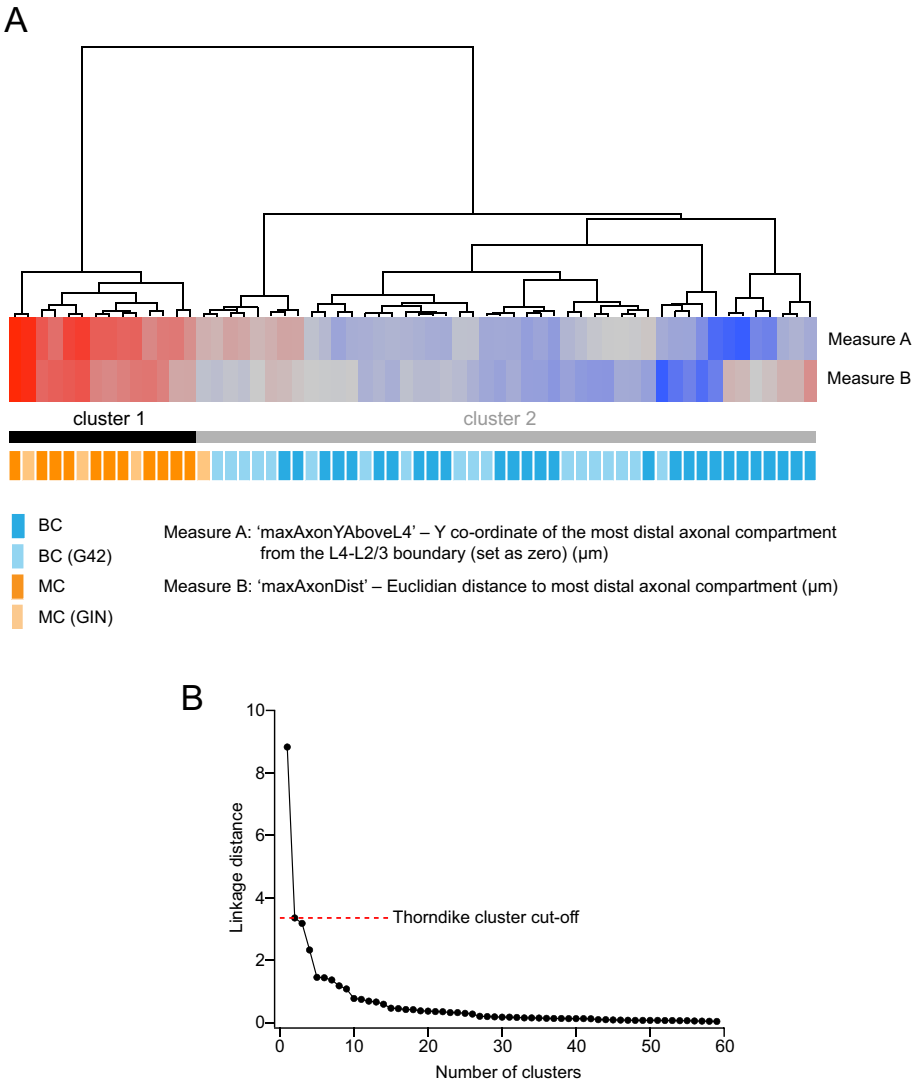

Figure 3.2: **Hierarchical two-way clustering on selected axonal features**. (**A**) Dendrogram showing results of two-dimensional hierarchical cluster analysis (Ward's method) on two axonal features. The x-axis represents the individual cells and the y-axis represents the within-cluster linkage distance (dendrogram branch scale proportional to within-cluster linkage distance). The blue-to-grey-to-red colour map indicates the values of the two measures. The horizontal bars denote the two major clusters identified by Thorndike's procedure for cluster cut-off, as illustrated in panel B. The orange and cyan bars indicate the original classification of targetted cells from transgenic (G42 and GIN lines) and WT mice. (**B**) 'Scree plot' of linkage distance against cluster number. Each point represents a single cluster join. The dashed red line illustrates the linkage step leading to the maximum increase in linkage distance – indicating the presence of two major clusters (Thorndike procedure; Cauli et al. 2000; Helmstaedter et al. 2009).

I also examined the same data using *k*-means clustering. The *k*-means method initially selects a set of *n* points called cluster seeds as a first guess of the means of the clusters. Each observation is assigned to the nearest seed to form a set of temporary clusters. The seeds are then replaced by the cluster means, the points are reassigned, and the process continues until no further changes occur in the clusters. Using this approach I observed the greatest correspondence with the hierarchical clustering when chosing four clusters (Figure 3.3). The identified clusters corresponded to MCs, BCs with ascending axons and two overlapping groups of BCs with locally arborizing axons.

3.4 Morphological features of identified IN clusters

Examination of the individual reconstructions confirmed the grouping. Figure 3.4 shows the cells from 'cluster 1' in Figure 3.2 ('red cluster' in Figure 3.3). These cells were predominantly from wild-type mice, but included three of the four cells recorded from mice of the GIN line. Overall, they had the appearance of the traditionally described L5 MCs as defined by their characteristic ascending axon, transcending all layers and branching at the pia (Wang et al., 2004). Figure 3.5 shows cells from the third cluster identified by the hierachical clustering in Figure 3.2 ('blue cluster' in Figure 3.3). These cells had a much reduced extent of ascending axon, which arborized in layer 2/3. These cells were recorded predominantly from mice of the G42 line. Their morphology is similar to that previously described for PV-positive INs with translaminar axonal arborization – identified as 'type 1 PV cells' by Buchanan et al. (2012) or as 'translaminar' neurons by Bortone et al. (2014). In subsequent sections I will refer to this group of cells a 'type 1 BCs'. Figure 3.6 shows all of the remaining cells ('cluster 2' in Figure 3.2). These cells were from both WT mice and those of the G42 (PV) line. Their morphology was that of classical BCs with axons that arborized locally in L5 (Buchanan et al., 2012). In subsequent sections I will refer to this group of cells a 'type 2 BCs'.

Graphical representation of the overall morphometric distinctions between these INs is provided in Figure 3.7 on page 80. This shows, for each class of IN, a single representative reconstruction, overlaid convex hulls, density maps of average axonal and

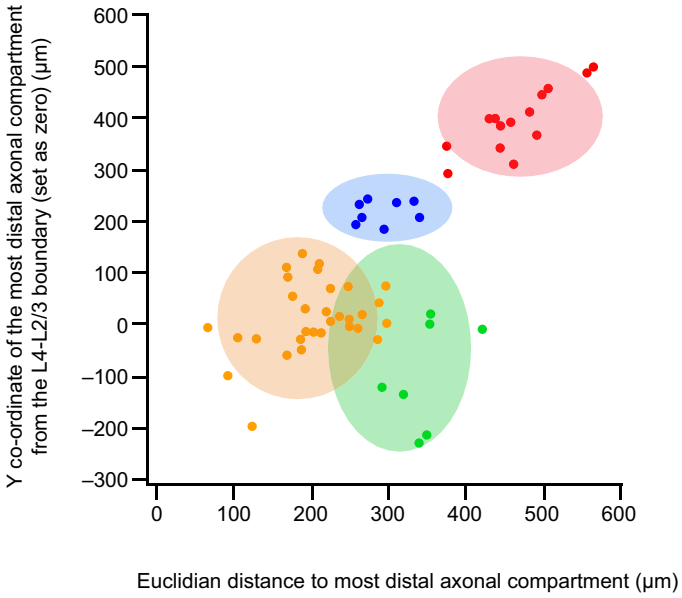

Figure 3.3: ***k*-means clustering**. Scatter plot showing the results of *k*-means clustering with four clusters. The filled circles denote individual cells and their colours denote membership of the four clusters. Shaded elipses indicate the regions in which 90% of observations in each cluster are expected to fall. All red symbols are from cells that show the greatest extent of ascending axon – all orginally designated MC or MC (GIN) cells. The blue symbols indicate cells that have some ascending axon – predominantly BC (G42) cells. The yellow and green symbols denotes cells with axons that arborize more locally – both BC and BC (G42) – that fall into two overlapping clusters.

dendritic arbors, ensemble Sholl diagrams and a bar plot of total axonal and dendritic lengths within the cortical layers. The convex hulls provide a representation of the maximum extent of axonal and dendritic arborization. The density maps indicate the average distribution of the axonal and dendritic arborization. Sholl analysis (Sholl, 1953) is a quantitative method to describe branching patterns of axons and dendrites by counting the number of branches intersecting concentric circles of increasing radii centered over the soma; it provides a way to assess the pattern of axonal and dendritic branching and, together with the measures of neurite lengths within different layers, provides a way to judge the IN segregation.

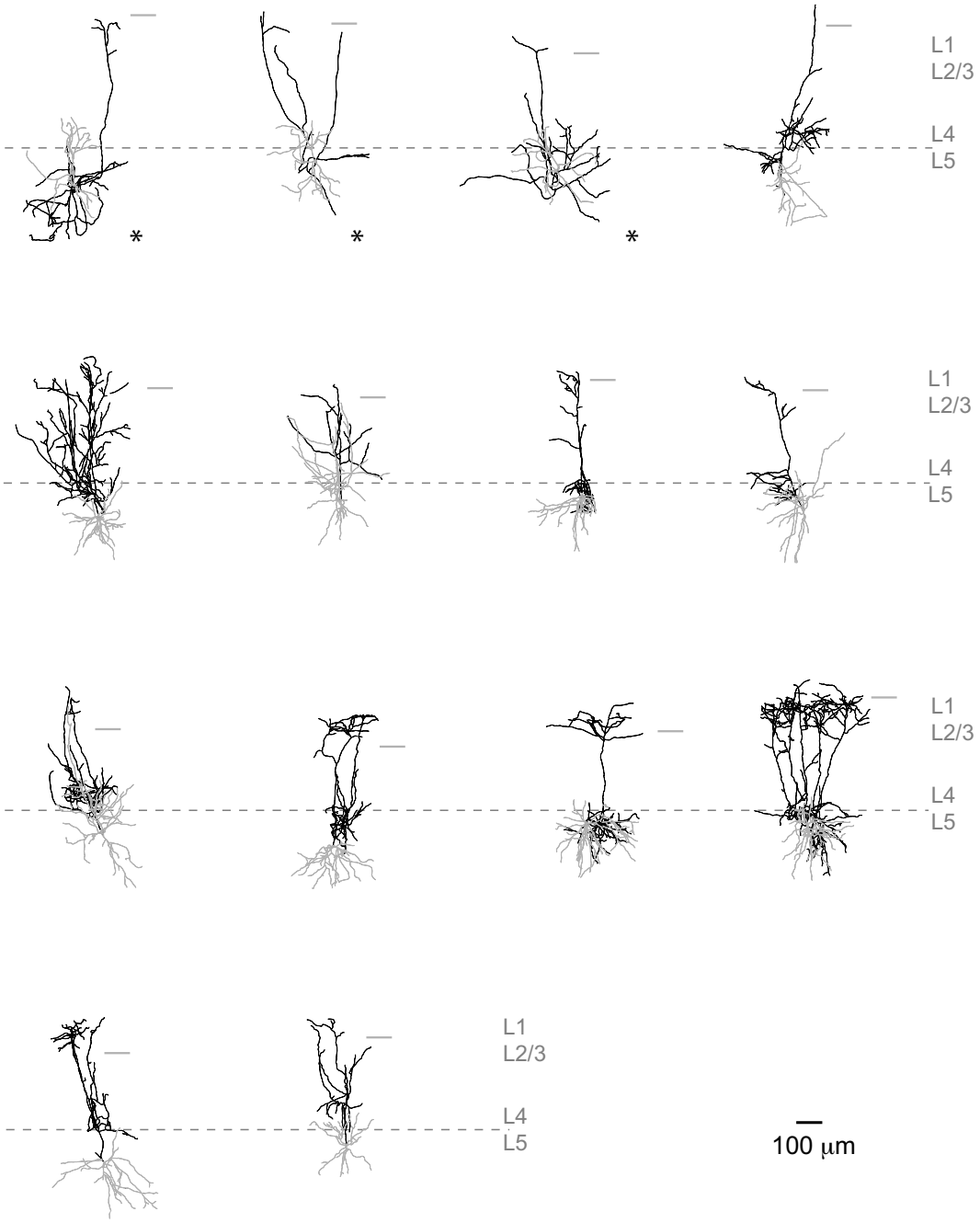

Figure 3.4: **Reconstructions of the 14 cells forming the major cluster 1 in Figure 3.2.** The axonal compartments are shown in black, and the dendritic compartments are shown in grey. The cells are aligned on the L4-L5 boundary (grey dashed lines). Grey ticks next to individual cells mark the L1-L2/3 boundaries. Asterisks indicate cells from the GIN line. Of note, although it is possible that both axons and dendrites could be cut during the slicing process, care was taken to minimise this possibility by targeting cell bodies relatively deep within the 300 μm slice. Moreover, any cells showing clearly cut axons were excluded from analysis.

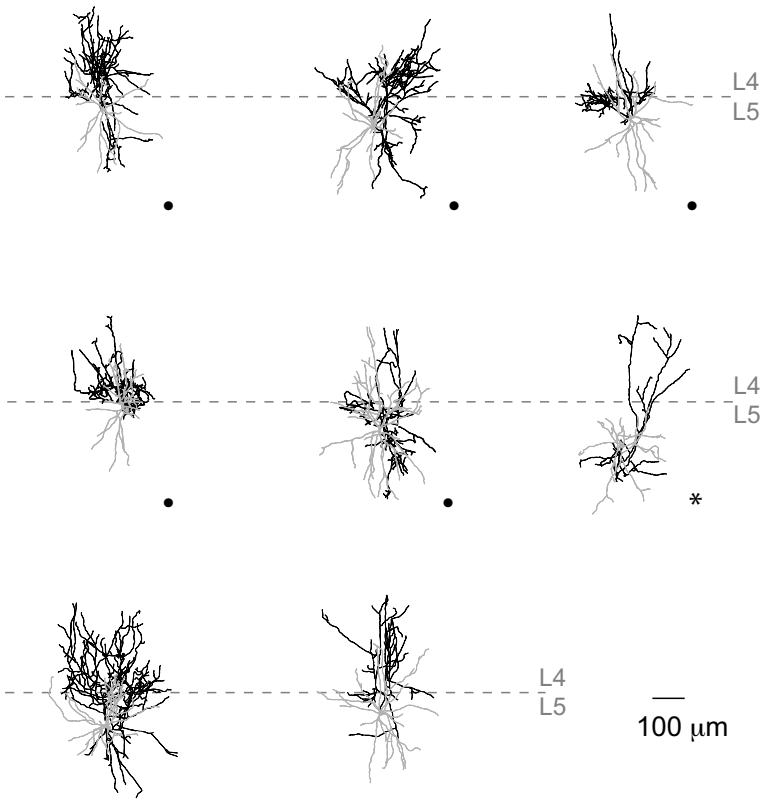

Figure 3.5: **Reconstructions of the eight cells forming the third cluster in Figure 3.2**. The axonal compartments are shown in black, and the dendritic compartments are shown in grey. The cells are aligned on the L4-L5 boundary (grey dashed lines). Filled circles indicate cells from mice of the G42 line.

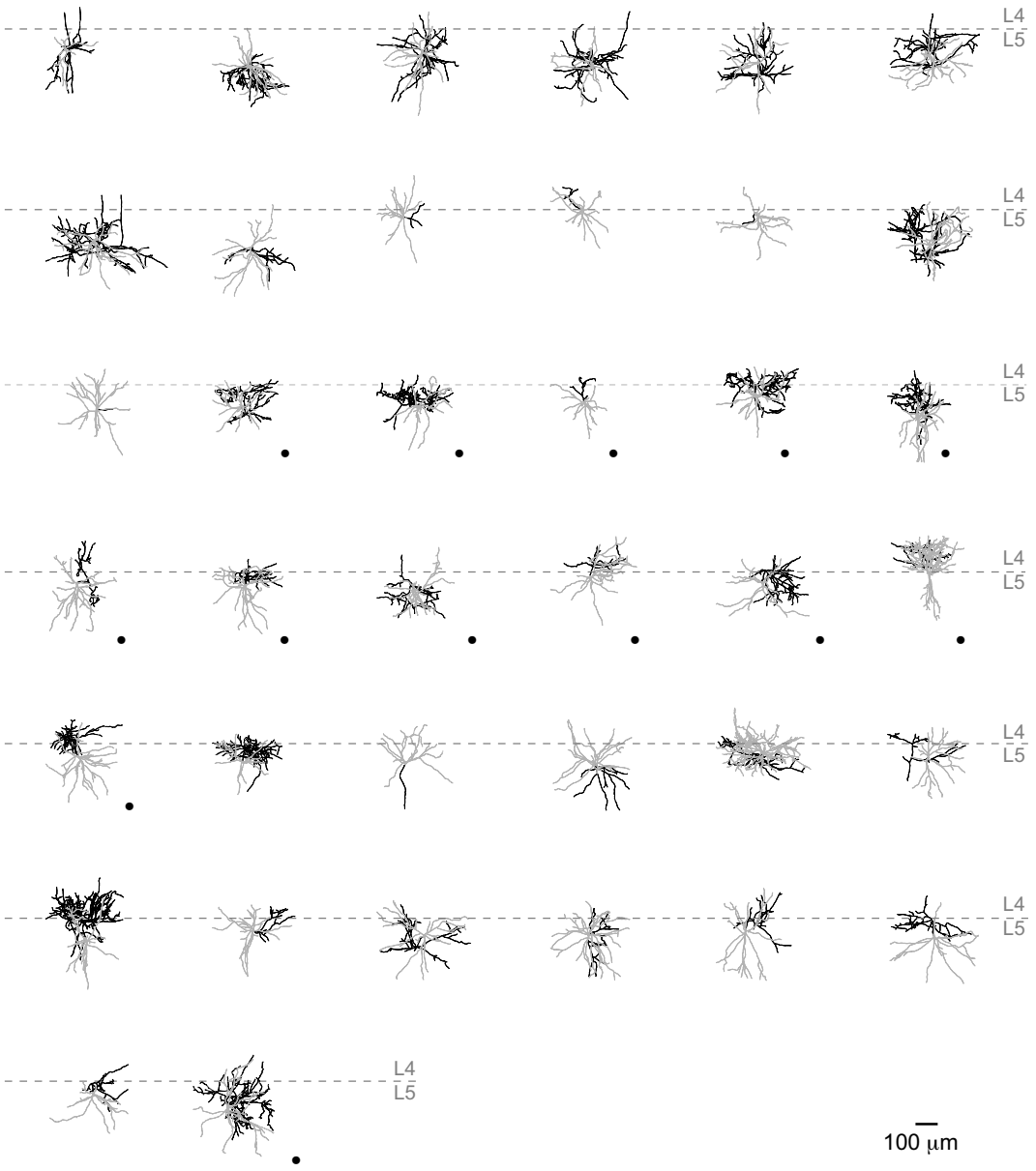

Figure 3.6: **Reconstructions of the 38 cells forming cluster 2 in Figure 3.2** . The axonal compartments are shown in black, and the dendritic compartments are shown in grey. The cells are aligned on the L4-L5 boundary (grey dashed lines). Filled circles indicate cells from mice of the G42 line.

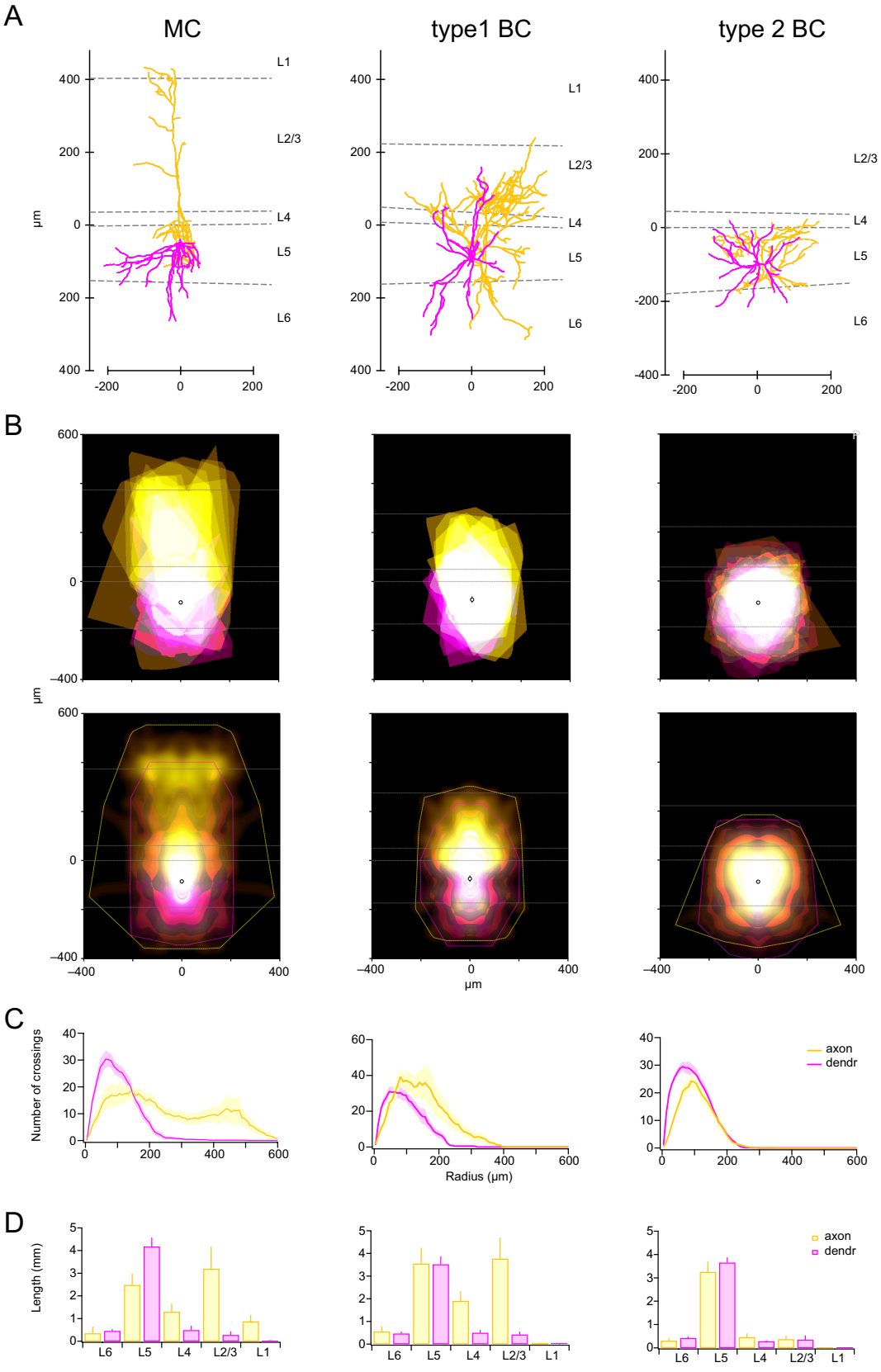

Figure 3.7: **Morphometric analysis of identified IN clusters.** (**A**) Representative IN reconstructions with axonal compartments in yellow and dendritic compartments in magenta. Individual reconstructions were aligned on the L4-L5 boundary

Figure 3.7: Legend continued...
(0 μm on y-axis), with horizontal dotted grey lines marking layer boundaries. (**B**) Upper row shows overlaid convex hulls (see Chapter 2) illustrating the maximum extents of axonal (yellow) and dendritic (magenta) arbours in individual cells (14 MCs, 8 type 1 BCs and 38 type 2 BCs) . The lower row shows density maps denoting the average distributions of axonal (yellow) and dendritic (magenta) compartments. The yellow- and magenta dashed lines indicate axonal and dendritic ensemble convex hulls (the symmetry in both the density maps and ensemble hulls arises from mirroring of the reconstructions). Horizontal dashed white lines demarcate neocortical layer boundaries, while the open circles show the soma positions. (**C**) Ensemble Sholl diagrams showing the number of axonal (yellow) or dendritic (magenta) branches crossing a given radial distance from the soma. (**D**) Bar plots showing the total length of neurite arborisation in different neocortical layers.

Statistical analysis of qMorph measures by IN group (MC, type 1 BC and type 2 BC) showed differences in axonal but not dendritic morphology. One way analysis of variance (Welch heteroscedastic F test) revealed no significant difference among the cells for any measure of dendritic morphology (all $p > 0.05$). By contrast, this omnibus test revealed differences across the cells for fifteen out of nineteen measures of axonal morphology. Subsequent pairwise comparisons using two-sided Welch two-sample t tests (with Holm's sequential Bonferroni correction for multiple comparisons) showed differences between MCs and type 1 BCs, differences between MCs and type 2 BCs, differences between type1 and type 2 BCs or differences between all three IN classes (see Table 3.2).

qMorph Measure	IN class			
	MC (n =14)	**type 1 BC** (n = 8)	**type 2 BC** (n = 38)	**ANOVA**
AxonRelYCenter (μm)	81.3 ± 23.4	8.6 ± 17.4*	–68.5 ± 12.2$^{***\ \#}$	$F_{(2,19.89)}$= 17.91, $p < 0.001$
AxonCenterDist (μm)	116.3 ± 13.2	55.0 ± 5.3*	93.6 ± 8.9	$F_{(2,28.44)}$= 13.37, $p < 0.001$
AxonAngle (°)	69.0 ± 19.8	42.4 ± 30.4	–52.6 ± 11.9$^{***\ \#\#}$	$F_{(2,16.36)}$= 15.16, $p < 0.001$
MaxAxonDistCompY (μm)	451.6 ± 14.8	48.1 ± 106.2***	–143.2 ± 23.9$^{***\ \#\#}$	$F_{(2,16.71)}$= 217.9, $p < 0.001$
MaxAxonDist (μm)	473.5 ± 15.0	299.4 ± 11.5**	237.8 ± 12.8$^{***\ \#}$	$F_{(2,25.59)}$= 72.81, $p < 0.001$
MaxAxonDistCompAngle (°)	94.7 ± 4.7	34.6 ± 32.7*	–49.4 ± 10.8$^{***\ \#\#}$	$F_{(2,16.71)}$= 72.96, $p < 0.001$
AxonHullCenterY (μm)	142.0 ± 15.0	22.0 ± 17.8***	–70.4 ± 12.3$^{***\ \#\#}$	$F_{(2,20.4)}$= 58.21, $p < 0.001$
AxonHullHeight (μm)	624.5 ± 33.4	479.1 ± 35.9**	238.5 ± 16.2$^{***\ \#\#\#}$	$F_{(2,16.51)}$= 60.92, $p < 0.001$
percAxonAboveL5 (%)	60.6 ± 7.0	57.1 ± 7.5	23.1 ± 4.9$^{***\ \#\#}$	$F_{(2,19.77)}$= 12.38, $p < 0.001$
AxonAreaAboveL5 (μm^2)	110245 ± 11011	56366 ± 6063***	9287 ± 1669$^{***\ \#\#}$	$F_{(2,13.48)}$= 63.39, $p < 0.001$
AxonMaxVal	30.7 ± 4.3	52.0 ± 7.3*	29.5 ± 3.2$^{\#}$	$F_{(2,17.31)}$= 3.93, $p < 0.05$
AxonCritR (μm)	195.5 ± 40.3	115.8 ± 16.5	87.0 ± 5.2***	$F_{(2,13.81)}$= 4.56, $p < 0.05$
AxonLenAboveL4 (μm)	4062.0 ± 996.7	3799.0 ± 948.4	370.1 ± 149.7$^{***\ \#\#\#}$	$F_{(2,12.71)}$= 12.15, $p < 0.01$
MaxAxonYAboveL4	393.1 ± 16.6	216.0 ± 8.0***	–9.3 ± 14.0$^{***\ \#\#\#}$	$F_{(2,29.35)}$= 177.3, $p < 0.001$
AxonAreaAboveL4	93775 ± 9961	43114 ± 5491***	4007 ± 1322$^{***\ \#\#\#}$	$F_{(2,13.17)}$= 59.04, $p < 0.001$

Table 3.2: **Statistical comparison of axonal features of the three IN types.** The ANOVA column shows the results of the omnibus test (Welch heteroscedastic F test). Asterisks denote difference from MCs (* $p < 0.05$, ** $p < 0.01$, *** $p < 0.001$) while hashes denote difference from type 1 BC ($^{\#}$ $p < 0.05$, $^{\#\#}$ $p < 0.01$, $^{\#\#\#}$ $p < 0.001$) (two-sided Welch two-sample t tests with Holm's sequential Bonferroni correction for multiple comparisons).

3.5 Discussion

My results are consistent with the clear distinction between MCs and BCs, as previously described in the literature (see, for example Ascoli 2008; DeFelipe et al. 2013; Markram et al. 2004) and support the approach used for targetting these IN classes (molecular markers and/or somatic shape). MCs clearly differed in their dendritic and axonal branching patterns from BCs, with much less overlap of dendritic and axonal compartments (see Figure 3.7). This morphological classification is used in the following chapter, to facilitate the investigation of AMPAR expression by BCs and MCs.

Of note, while there is close agreement in the literature as to what constitues MC morphology, this is not true of BCs (DeFelipe et al., 2013). Additionally, many different and potentially confusing naming schemes have been employed by different authors. Many authors do not subclassify BCs and instead talk only about the group as a whole (Hendry et al., 1983; Jones, 1993; Somogyi et al., 1998). On the other hand, varying morphologies have been classified as, for example, 'typical' BCs (Gupta et al., 2000), 'common' BCs (DeFelipe et al., 2013), 'small' BCs (Gupta et al., 2000; Kawaguchi and Kubota, 1996, 1998; Wang et al., 2002), 'large' BCs (Hendry et al., 1989; Kisvárday et al., 1985; Somogyi et al., 1983; Wang et al., 2002) or 'nest' BCs (Gupta et al., 2000; Wang et al., 2002). Cluster analyses showed that the BCs I recorded could be divided into at least two subgroups (Figure 3.5 and Figure 3.6), with one type exhibiting ascending translaminar axonal arborization (type 1 BCs) and the other type exhibiting local axonal arborization largely confined to L5 (type 2 BCs). The existence of non-MCs with ascending axonal arborisation has been described previously by Helmstaedter et al. (2009). Importantly, two studies in the mouse visual cortex describe a non-MC IN type in the infragranular layers that sends its axonal arborization across multiple layers (Buchanan et al., 2012; Bortone et al., 2014). Interestingly, both studies found this IN type in the G42 mouse line. Five out of eight of my type1 BCs were patched in the G42 line (and are thus presumably PV-expressing INs). Two of the eight cells were from WT mice. All seven of these cells had mEPSCs that were distinct from those of the MCs I recorded (see Chapter 4). The remaining cell in this cluster was from the GIN line and also had distinct mEPSCs as well as firing properties charac-

teristic of an MC. Although it may be thought odd that this cell clustered separately from MCs (albeit in an adjacent cluster), this simply reflects the fact that morphological features, as detected here, could not provide an absolute distinction. This is not necessarily unexpected, as axonal variability has peviously been described for INs in SOM-positive lines (X94 and X98) and the GIN line (Ma et al., 2006; McGarry et al., 2010).

One important question arising from all of these studies is whether different methodological approaches can be compared with each other in respect of their level of accuracy, completeness and resolution. Reconstructions from fluorescence imaging stacks acquired with 2PLSM have been shown to be comparable with biocytin reconstructions in regard to comparison of overall morphology (Blackman et al., 2014). While biocytin reconstructions certainly remain the best choice for the tracing of more distal aborisations, given that one has access to a 2PLSM, reconstructions from fluorescence imaging is gained at comparatively lower costs and more easily.

Although the popularity of reconstructions from fluorescence markers has increased significantly over the last twenty years (Halavi et al., 2012), one limitation of the 2PLSM approach is the time taken to perform single-point scanning of the whole IN aborisation. When combined with the time required for manual reconstruction, this represents something of a bottleneck. One development that offers the possibility of avoiding the time consuming step of manual reconstruction of these 2PLSM stacks is the automated Sholl analysis directly from bitmap images. Colleagues in McGill have developed a new open-source plug-in for ImageJ that allows one to bypass manual reconstructions. Although this requires high-quality image stacks and pre-processing to remove the pipette, it allows rapid and fully-automated morphometric analysis. Importantly, despite an inability to unambiguously discriminate axonal from dendritic segments and the consequent reliance on data from both compartments, using twelve of my eighteen G42 INs, this approach was able to independently verify the existence of type 1 and type 2 BCs (Ferreira et al., 2014).

Although 2PLSM has proved successful (whether used with manual or automated reconstruction), improvement in accuracy of reconstruction is likely to come from improvements in image quality. For example, additional detail could come from super-

resolution fluoerescence microscopy (Lemmens et al., 2010; Parekh and Ascoli, 2013). Such techniques rely either on the sequential and stochastic switching on and off of fluorphores (stochastic optical reconstruction microscopy - STORM; Rust et al. 2006 and photo-activated localization microscopy PALM; Betzig et al., 2006) or the use patterned illumination (stimulated emission depletion - STED; Klar and Hell, 1999 and saturated structured illumination microscopy - SSIM; Gustafsson, 2005) to achieve nanometer resolution. Although challenges remain (Lu, 2011), the potentially enhanced accuracy of reconstruction afforded by such techniques may help in the quest for automated neuromorphological reconstruction through the use of image analysis algorithms and initiatives such as DIADEM (Digital Reconstruction of Axonal and Dendritic Morphology) (Donohue and Ascoli, 2011; Gardner et al., 2008).

Chapter 4

Electrophysiological characterisation of layer 5 INs

4.1 Introduction

In the previous chapter I used features of dendritic and axonal morphology to identify BCs and MCs. In this chapter I first confirmed this classification by examining the firing properties of the cells (Kawaguchi and Kubota, 1997; Markram et al., 2004; Silberberg and Markram, 2007), before investigating the properties of their AMPAR-mediated mEPSCs. Importantly, all electrophysiological observations were taken from cells that were morphologically reconstructed and identified as either MCs or BCs (type 1 or type 2).

My main goal was to examine the presence of CP-AMPARs at synapses on the two IN types. As discussed in Chapter 1, in this regard one frequently used functional approach is to assess the degree of spermine-dependent rectification of EPSCs. Conventionally, this question could be approached in several ways; either using paired recordings, extracellularly-evoked EPSCs or mEPSCs. With paired recordings (PC-to-INs) the presynaptic partner is clearly defined and presynaptic 'factors' such as the precise timing of glutamate release can be controlled. With extracellularly evoked EPSCs, timing is similarly controlled but the presynaptic element is less easily determined. In both cases, voltage-activated sodium channels can not be blocked and therefore when

blocking $GABA_A$ receptors, there can be difficulties in controlling the excitability of the slice. Moreover, the paired recording approach suffers from a potentially low success rate while with extracellular stimulation it can be difficult to maintain a consistent response. Accordingly, I chose to record mEPSCs in the presence of TTX.

Miniature (quantal) events result from the random exocytosis of single vesicles of transmitter, as originally described at the neuromuscular junction more than 60 years ago (Fatt and Katz, 1952). Unlike unitary or evoked currents, that occur at a subset of excited synapses, mEPSCs can arise at any of the synaptic contacts on a neuron and thus sample the entire excitatory synaptic input onto the recorded cell. This could be viewed as an experimental advantage. However, the comparatively small amplitude and random occurence of mEPSCs makes their detection and analysis challenging. Given that mEPSCs can originate from all synapses throughout the dendritic tree, measures may need to be taken to restrict analysis to those well-clamped events with fast risetimes indicative of an origin proximal to the soma (see Section 4.1).

4.2 Results

4.2.1 Firing patterns

I first sought to confirm the spiking behaviour of the two major cell groups (MCs and BCs), identified morphologically in Chapter 3. As expected, cells of the two classes (from hierachical cluster 1 and 2) that were recorded using a K-gluconate internal displayed properties characteristic of the corresponding anatomical types, as previously described in the literature (Ascoli, 2008; Buchanan et al., 2012; Markram et al., 2004).

The firing behaviour of a representative PV-positive BC is shown in Figure 4.1 on page 89. When comparing BCs that were patched from WT mice with those patched from the G42 line, the firing behaviour of both types was very similar. The only observed difference was a small, albeit statistically significant, difference in spike AHP (see Table 4.1 on page 90). In the following sections, the WT-BCs and PV-positive BCs are treated as equivalent, and data from these cells are pooled. Overall, the firing properties of the BCs were similar to those reported previously (Ascoli, 2008;

Buchanan et al., 2012; DeFelipe et al., 2013; Kawaguchi and Kubota, 1997; Markram et al., 2004). Specifically, they displayed narrow action potentials, a relatively large AHP, fast spiking and little spike accomodation. The majority of the BCs for which firing properties were examined were of morphological type 2. Both these cells, and the two type 1 cells recorded, displayed firing properties similar to those previously described for these two classes (Buchanan et al., 2012).

The firing behaviour of a representative MC is shown in Figure 4.2 on page 91. The MCs (cells from cluster 2, Chapter 3) were different from BCs in their discharge behaviour. They exhibited a relatively broad spike width, a smaller AHP, lower firing frequency, a higher R_{input} and a lower spike threshold. These differences, highlighted in Table 4.2 on page 92, are evident when comparing Figures 4.1 on the following page and 4.2 on page 91 and in the plots of firing frequency and accomodation for these two representative cells (Figure 4.3 on page 93).

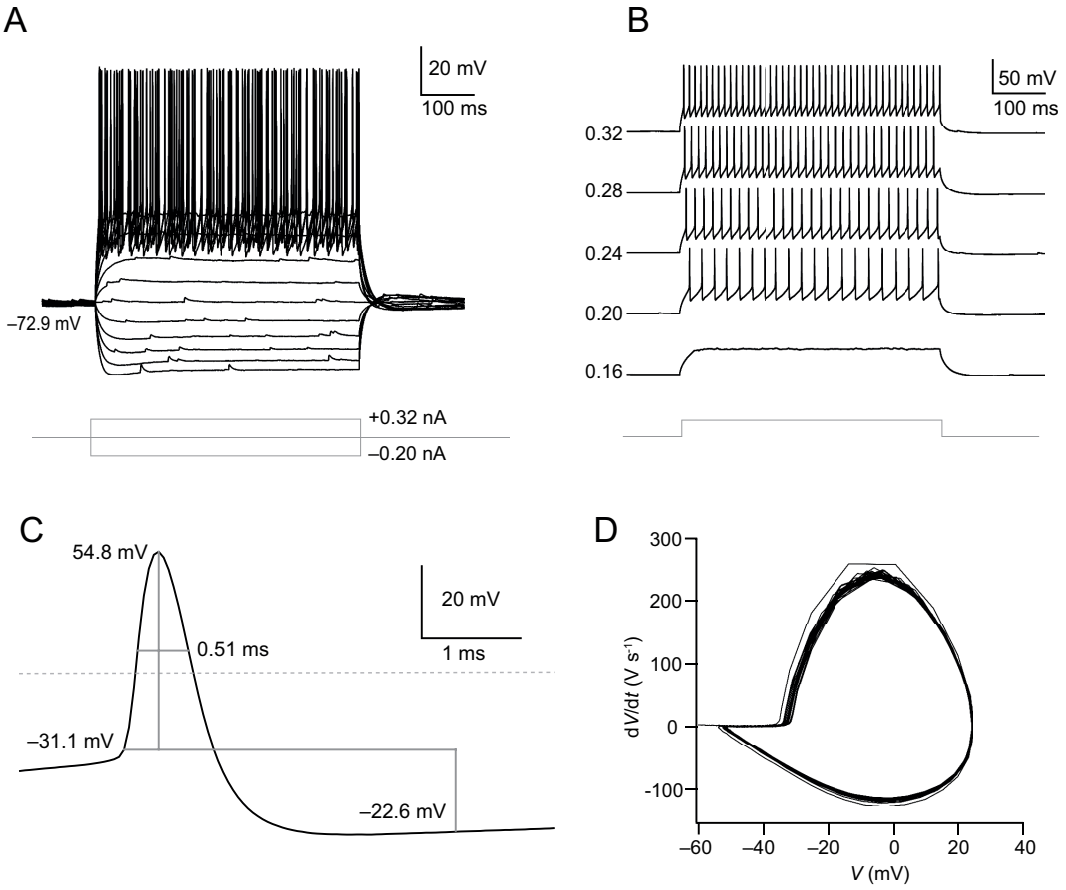

Figure 4.1: **Firing properties of a representative (morphologically identified) PV-positive type 2 BC.** (**A**) Voltage responses from rest (–72.9 mV) to current injections (–0.2 to +0.32 nA). Note the clear spontaneous EPSPs. (**B**) Voltage responses to the largest subthreshold- and four suprathreshold current injections (current values in nA shown to the left). Note the regular fast-spiking pattern. (**C**) An illustration of the spike threshold, spike height, spike half-width and AHP measured from the first spike in the rheobase trace. Note the relatively narrow spike and large AHP, typical of BCs. The horizontal dashed line indicates 0 mV. (**D**) Phase plot of the rheobase response. Note the relatively consistent spike shape throughout the sweep, with little change in spike threshold.

Measure	**PV-positive BCs** (n = 6)	**BCs** (n = 17)
V_{m}(mV)	–70.1 ± 1.4	–69.3 ± 1.1
R_{in}(MΩ)	130.8 ± 14.3	163.1 ± 18.8
$R_{\mathrm{series,\ compensated}}$ (MΩ)	6.56 ± 1.09	11.67 ± 1.08 **
C_{m}(pF)	18.5 ± 2.81	25.38 ± 2.5
$\tau_{\mathbf{m}}$(ms)	10.5 ± 0.8	12.9 ± 2.0
I_{H} measure	–0.07 ± 0.01	–0.07 ± 0.01
Spike threshold (mV)	–30.8 ± 1.7	–28.2 ± 5.3
Spike height (mV)	55.5 ± 2.5	51.0 ± 2.2
Spike half-width (ms)	0.54 ± 0.02	0.59 ± 0.04
Spike AHP (mV)	–22.9 ± 0.9	–18.9 ± 1.0 *
Rheobase current (nA)	0.29 ± 0.04	0.23 ± 0.03
Mean freq. 1.5x rheo. (Hz)	57.7 ± 6.3	57.0 ± 6.6
Accommodation (%)	–25.4 ± 19.2	–3.1 ± 8.8

Table 4.1: **Electrophysiological properties of PV-positive- and WT BCs.** Values are mean ± SEM. The two groups of BCs show firing properties that are very similar. There was a small, albeit statistically significant, difference in AHP (* p <0.05; two-sided Welch two-sample t test).

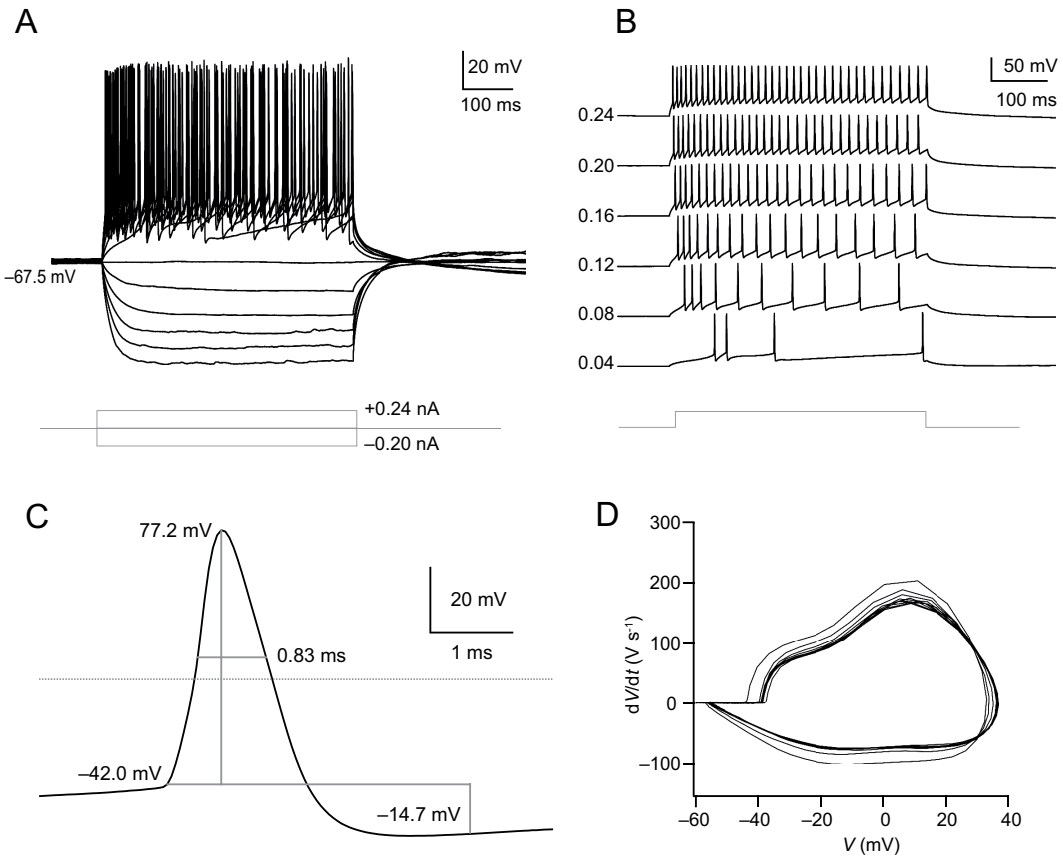

Figure 4.2: **Firing properties of a representative (morphologically identified) MC.** (**A**) Voltage responses from rest (–67.5 mV) to current injections (–0.2 to +0.24 nA). Note the absence of clear spontaneous EPSPs. (**B**) Voltage responses to the six suprathreshold current injections (current values in nA shown to the left). Note the clear accomodation. (**C**) An illustration of the spike threshold, spike height, spike half-width and AHP measured from the first spike in the rheobase trace. Note the relatively wide spike and small AHP, typical of MCs. The horizontal dashed line indicates 0 mV. (**D**) Phase-plane plot of the rheobase response. Note the subtle components reflecting two phases of spike initiation, the rather variable spike shape throughout the sweep, and changes in spike threshold.

Measure	**MCs** (n = 4)	**type 1 and 2 BCs** (n = 23)
V_{m}(mV)	–67.2 ± 1.0	–69.5 ± 0.9
R_{in}(MΩ)	272.3 ± 38.0	154.7 ± 14.6 *
$R_{\mathrm{series,\ compensated}}$(MΩ)	6.14 ± 1.76	10.34 ± 0.96
C_{m}(pF)	13.74 ± 0.99	23.58 ± 2.06 ***
$\tau_{\mathbf{m}}$(ms)	22.33 ± 4.88	12.27 ± 1.48
I_{H} measure	–0.25 ± 0.08	–0.07 ± 0.01
Spike threshold (mV)	–38.6 ± 1.3	–28.8 ± 3.9 *
Spike height (mV)	69.4 ± 4.7	52.2 ± 1.8 *
Spike half-width (ms)	0.75 ± 0.05	0.58 ± 0.03 *
Spike AHP (mV)	–11.7 ± 1.0	–19.9 ± 0.9 ***
Rheobase current (nA)	0.07 ± 0.01	0.24 ± 0.02 ***
Mean freq. 1.5x rheo. (Hz)	13.0 ± 3.4	57.2 ± 5.1 ***
Accommodation (%)	229.7 ± 118.8	–8.9 ± 8.3

Table 4.2: **Electrophysiological properties of MCs and BCs.** Values are mean ± SEM. MCs show firing properties that are clearly distinct from those of BCs. Asterisks denote significant differences (* p <0.05, ** p < 0.01, *** p <0.001) (two-sided Welch two-sample t tests).

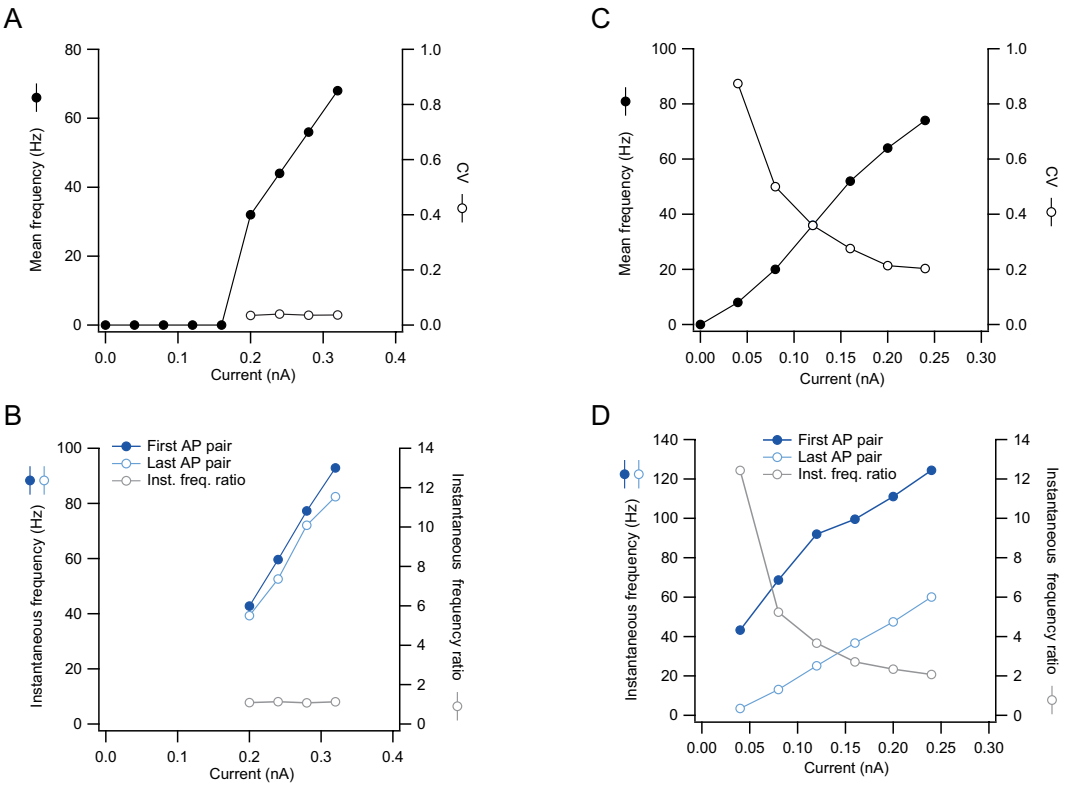

Figure 4.3: **Comparison of BC and MC spiking frequency and accomodation.** (**A**) Mean frequency and CV plotted against injected current for the same BC shown in 4.1. (**B**) Instantaneous frequency and instantaneous frequency ratio plotted against injected current for the same BC. (**C**) and (**D**) Same as A and B, but for the MC shown in 4.2. Note, the mean frequency at rheobase of the BC is 32 Hz while that of the MC is 8 Hz. Also, note the absence of accomodation in the BC firing (grey symbols in B), and the marked accomodation in the firing of the MC (grey symbols in D).

The two IN groups morphologically identified in Chapter 3 clearly show firing properties expected of MCs and BCs. In the next section I describe the properties of mEPSCs in these two IN types.

4.2.2 Properties of mEPSCs from MCs and BCs

mEPSCs were recorded at –60mV with K- or Cs-gluconate-based internals in the presence of TTX (to block voltage-gated Na^+ channels). To isolate currents through AMPARs, the external solution contained D-APV (to block NMDARs), SR-95531 (to block $GABA_A$Rs) and CGP 54626 (to block $GABA_B$Rs) (see Chapter 2). mEPSCs were detected using a threshold-crossing method (Kudoh and Taguchi, 2002) with a chosen amplitude threshold of 2.5 x SD. All mEPSCs were visually examined and those with a stable baseline and non-contaminated rise and decay were selected for analysis. For these selected events, measurements of peak amplitude, 20-80% rise time and 37% decay time were taken from a fitted waveform (see Chapter 2). I initially generated amplitude distributions and examined the relationship betwen mEPSC rise and decay. As described in Section 1.6.1, the mEPSCs recorded in BCs originate from local PCs (Wang et al., 2002) and long-range input from the thalamus (Cruikshank et al., 2007). As described in Section 1.6.2, mEPSCs in MCs originate predominantly from local- and translaminar PCs (Berger et al., 2009; Kapfer et al., 2007; Silberberg and Markram, 2007) as they receive little thalamic input (Cruikshank et al., 2007).

Dendritic filtering

For both the BC and the MC shown in Figures 4.4 and 4.5, the plots of mEPSC rise time versus decay time showed an apparent correlation. This result could be explained by dendritic filtering of the somatically recorded mEPSCs. Whole-cell voltage-clamp recordings made from the soma allow only indirect measurement of mEPSCs originated in the dendrites. Because of cable filtering, the ability of the somatic electrode to clamp the voltage at the dendritic synapses is expected to decline as the active

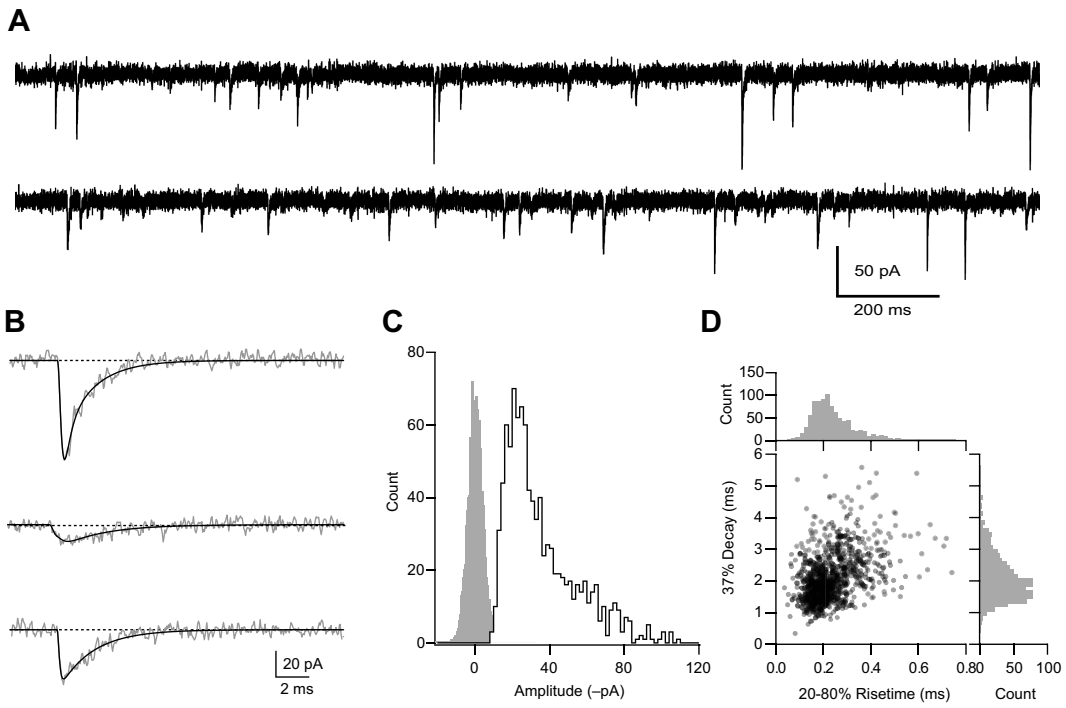

Figure 4.4: **Representative mEPSCs from a L5 BC.** (**A**) Raw traces at –60mV from a cell recorded with a K-gluconate internal. (**B**) Selected events fitted with an empirical function (see Chapter 2). (**C**) Distribution of mEPSC amplitudes (from fitted traces). The grey histogram shows the background current noise, from which the detection threshold was calculated (2.5 x SD = 7.0 pA). (**D**) Scatter plot of 20-80% risetime against 37% decay with marginal histograms. For this cell, the mean amplitude (from 961 events) was 35.2 ± 19.2 pA, the mean 20-80% risetime was 0.23 ± 0.10 ms and the mean 37% decay time was 2.11 ± 0.79 ms.

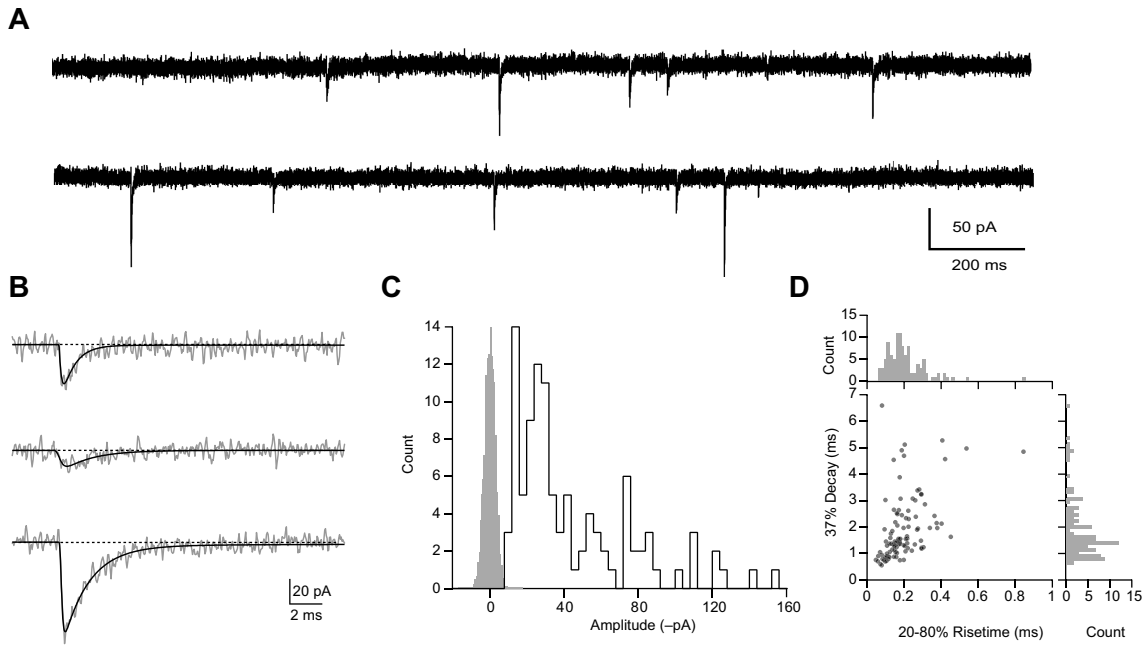

Figure 4.5: **Representative mEPSCs from a L5 MC.** (**A**) Raw traces at –60mV from a cell recorded with a Cs-gluconate internal. (**B**) Selected events fitted with an empirical function (see Chapter 2). (**C**) Distribution of mEPSC amplitudes (from fitted traces). The grey histogram shows the background current noise, from which the detection threshold was calculated (2.5 x SD = 7.7 pA). (**D**) Scatter plot of 20-80% risetime against 37% decay with marginal histograms. For this cell, the mean amplitude (from 103 events) was 44.5 ± 32.6 pA, the mean 20-80% risetime was 0.20 ± 0.11 ms and the mean 37% decay time was 1.93 ± 1.23 ms.

synapses are located progressively further away from the soma – the 'space clamp' problem (Bekkers and Stevens, 1996; Spruston et al., 1993; Williams and Mitchell, 2008). In this situation, without boosting by voltage-gated currents (Spruston, 2008), synaptic currents originating in the dendrites are attenuated at the soma and are slower than the conductance at the site of origin. Thus, it is important to appreciate that when synaptic currents originating from different parts of the cell are pooled, slower, smaller currents could simply reflect inadequate space clamp (Bekkers and Clements, 1999; Zhou and Hablitz, 1997).

To examine this in more detail, I examined plots of rise time versus decay time and rise time versus amplitude. For type 2 BCs recorded with Cs-gluconate internal, 17 out of 17 cells showed a significant positive correlation between rise and decay (all $p < 0.001$; Pearson's product-moment correlation coefficients ranged from +0.43 to +0.67). This significant correlation is indeed indicative of dendritic filtering, suggesting that the range of kinetics observed reflects the varied location of synapses accross the dendritic tree and not only differences in receptor properties. For rise versus peak, 14 out of 17 cells showed a significant ($p < 0.001$) negative correlation. For these cells the Pearson's product-moment correlation coefficients ranged from –0.14 to –0.38. Such a correlation is consistent with the idea that the kinetics of mEPSCs are influenced by dendritic filtering (Bekkers and Stevens, 1996). In an attempt to select proximal, well-clamped mEPSCs, I chose a rise time 'cut-off' that excluded slow-rising (distal) events. Selecting only those currents with rise times < 0.125 ms greatly reduced the correlations seen between rise and decay and between rise and amplitude. With this cut-off, the correlation coefficients for rise versus decay remained significant for only 8 out of 17 cells ($p < 0.05$; +0.13 to +0.26). For rise versus peak, only one of the 17 cells showed a significant negative correlation ($p < 0.01$; –0.12).

Similar results were obtained for MCs. For MCs recorded with a Cs-gluconate internal, 10 out of 10 cells showed a significant positive correlation between rise and decay (all $p < 0.001$; Pearson's product-moment correlation coefficients ranged from +0.42 to +0.62). For rise versus peak, 1 out of 10 cells showed a significant negative correlation ($p < 0.001$; –0.34). Following the selection of fast-rising events only (20-80% rise time < 0.125 ms), there was no significant positive correlation between rise and decay

and no significant negative correlation between rise and peak.

Kinetics of mEPSCs from different IN types

I first examined whether the kinetics of fast-rising (rise time < 0.125 ms) mEPSCs, presumed to arise proximal to the soma, differed between the two morphologically identified BC types. This was done for currents recorded using the Cs-gluconate internal, for which there were a sufficient number of cells. Figure 4.7 shows the pooled data comparing the mean rise time, amplitude and decay time for the type 1 and type 2 BCs. A Welch two sample *t* test showed no significant difference for the 20-80% rise time ($p = 0.82$), peak amplitude ($p = 0.15$) or 37% decay time ($p = 0.35$) for fast rising mEPSCs of type 1 and type 2 BCs. Broadly similar results were obtained when I did not use rise time to select events. Moreover, with the K-gluconate internal, the mEPSC amplitudes and kinetics for the two type1 BCs recorded fell in the range of values observed for the type 2 BCs ($n = 21$). Thus, the 20-80% rise time values for the two type 1 BCs were both 0.09 ms, while for type 2 BCs the average value was 0.098 ms (range 0.087 – 0.106 ms). For the peak amplitude, the corresponding individual values were 54.1 and 42.2 pA versus a mean value of 41.2 pA ms (range 21.9 – 77.7 pA). For the 37% decay time, the values were 0.92 and 0.86 ms, versus 1.22 ms (range 0.62 – 2.26 ms).

Given the lack of evidence for any difference in the properties of the mEPSCs from the two types of BCs, I next pooled these data and compared the overall pool of BCs with the MCs. Because the recordings were made with two different internals, which could introduce differences in mEPSC properties independent of the nature or number of the AMPARs in the two IN types, I compared the properties using two-way analysis of variance (Figure 4.8). For the 20-80% rise time, two-way ANOVA (Welch heteroscedastic *F* test) showed no significant main effect of IN type ($F_{1, 54} = 0.65$, $p = 0.42$). However, there was a significant main effect of the internal ($F_{1, 54} = 8.66$, $p < 0.01$) but no interaction between IN type and the internal ($F_{1, 54} = 2.30$, $p = 0.14$). Although there was a significant effect of the internal, overall the differences between internals and between MCs and BCs were very small, providing no evidence for any real difference between the IN types. For the peak amplitude, there was a significant

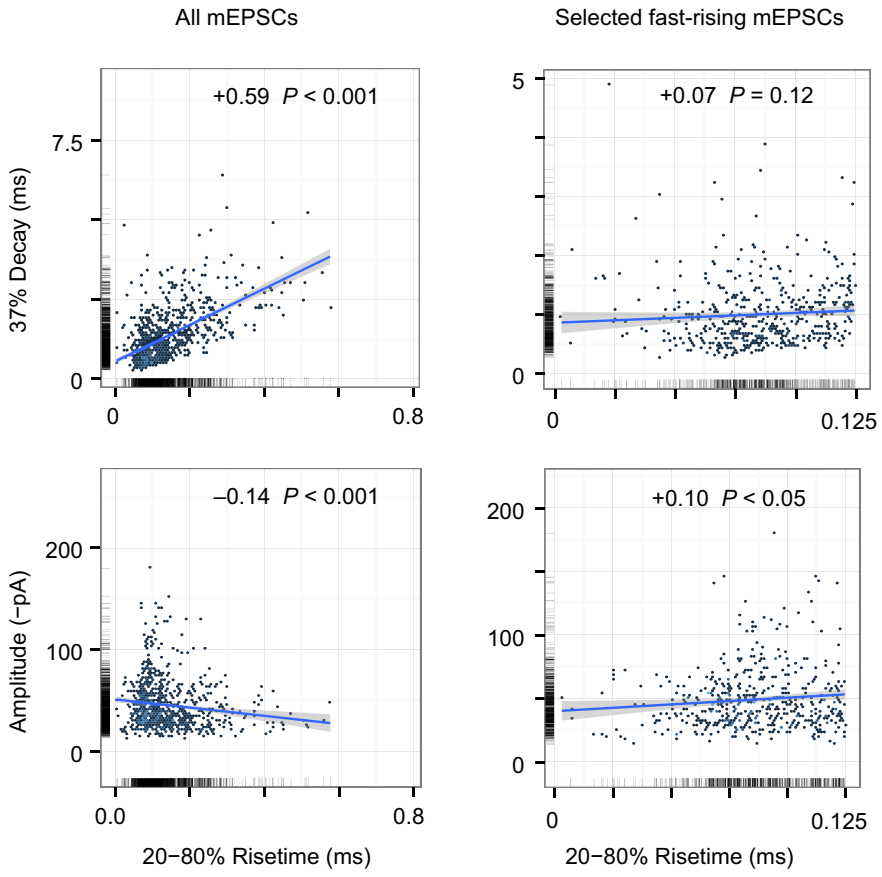

Figure 4.6: **Relationships between rise and decay and between rise and amplitude for mEPSCs from a representative type 2 BC (Cs-gluconate internal).** Left column shows scatterplots of 20-80% rise time versus 37% decay (upper panel) and amplitude (lower panel) for all mEPSCs. Pearson's product-moment correlation indicated positive and negative correlations between rise and decay and between rise and peak amplitude, respectively. This analysis used a parametric test. For this cell, when the analysis was repeated using a non-parametric Spearman's rank correlation test, the correlation coefficient (ρ) between rise and decay was reduced from 0.57 for all events to 0.18 for fast-rising events (in this case, however, both relationships were significant; $p < 0.0001$). For rise versus amplitude, both relationships were non-significant. Straight line indicates the 95% confidence interval. Marginal rug plots, Pearson's coefficient of correlation, and the p value are shown in each panel. Overplotted points are shown in brighter colour. The two scatterplots to the right show the corresponding data for selected fast-rising events (rise time < 0.125 ms). Of note, selecting fast-rising mEPSCs eliminated correlations that would be taken to indicate dendritic filtering.

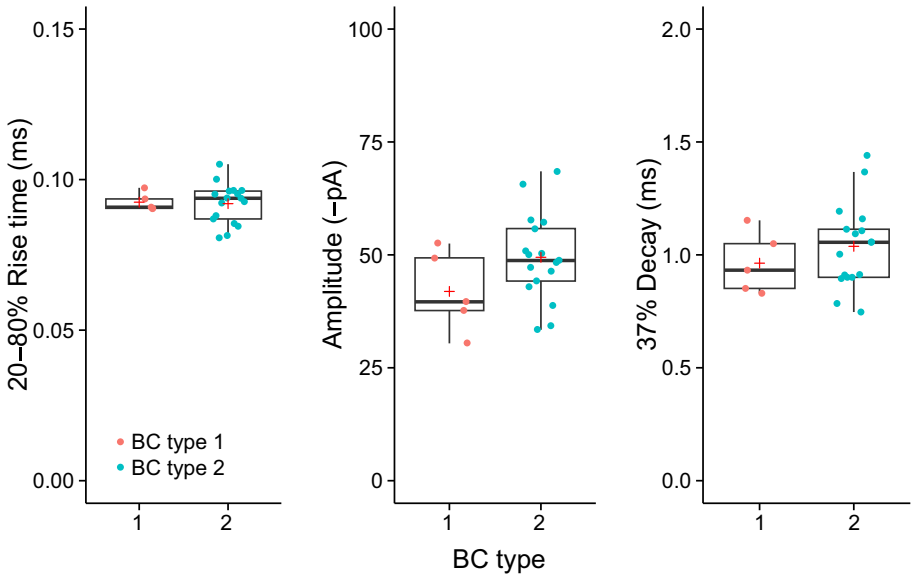

Figure 4.7: **Comparison of fast rising mEPSCs from type 1 and type 2 BCs.** Box-and-whisker plots for 20-80% rise time, peak amplitude and 37% decay time of mEPSCs (rise time < 0.125 ms) from five type 1 BCs (red symbols) and 17 type 2 BCs (cyan symbols) recorded with a Cs-gluconate internal. The plots indicate the median value (black line), the first and third quartiles (the 25th and 75th percentiles) (box) and the highest and lowest values within 1.5 x the inter-quartile range (whiskers); filled circles represent individual values and red crosses denote the means.

main effect of IN type ($F_{1, 54}$ = 36.31, $p < 0.001$), no main effect of the internal ($F_{1, 54}$ = 2.78, $p = 0.10$) and no interaction between IN type and internal ($F_{1, 54}$ = 0.23, p = 0.64). For the 37% decay time, there was a significant main effect of IN type ($F_{1, 54}$ = 4.23, $p < 0.05$), no main effect of the internal ($F_{1, 54}$ = 3.67, $p = 0.06$) and no interaction between IN type and internal ($F_{1, 54}$ = 0.08, $p = 0.78$). Overall, these data suggest that in MCs mEPSCs arising proximal to the soma are smaller and decay more slowly than do those in BCs.

Taken together, these results indicate a difference in mEPSC kinetics for MCs and BCs. Are these differences reflective of different types of synaptic AMPARs, specifically CI- and CP-AMPARs? Of course, the time course of synaptic currents is influenced not only by the properties of postsynaptic receptors, but also by the time course of quantal release and the rate of glutamate clearance from – and thus the time course of glutamate concentration in – the synaptic cleft (Barbour and Häusser, 1997; Jonas, 2000; Overstreet et al., 1999). However, it is known that the time course of AMPAR-mediated EPSCs is markedly different for PCs and INs in the hippocampus and neocortex, with much slower decay time constants for the PCs (Geiger et al., 1997; Jonas et al., 1993) and that this is mirrored in the properties of receptors examined in isolated outside-out patches (reviewed in Jonas 2000). Thus, Koh et al. (1995b) showed that the deactivation of AMPAR-mediated patch currents was 2-to-3-fold slower in the PC than in both hippocampal or L4 neocortical BCs. Importantly, these authors showed that AMPARs in BCs and PCs differed in their Ca^{2+} permeability, with BCs predominantly expressing GluA1 (flop) subunits and PCs exhibiting a much higher abundance GluA2 (flip) subunits (Geiger et al., 1995). Similar findings were obtained by Lambolez et al. (1996) when comparing regular-spiking PCs with fast-spiking non-PCs in the cortex. Thus, at face value, one might conclude that regular-spiking MCs, with slower mEPSCs, express a greater proportion of CI-AMPARs. However, the differences in decay time I observed between BCs and MCs (~1 vs 1.5 ms) were less than those reported between BCs and PCs (~1 ms vs 2.5 ms). Additionally, data from heterologously expressed recombinant AMPARs suggests that heteromeric (CI-) AMPARs (GluA1/A2(R)) do not in fact deactivate more slowly than homomeric (CP-) AMPARs (GluA1) (Coombs et al., 2012). Thus, the differences seen between different neurons may be influenced by factors other than the AMPAR subunit composition. This could

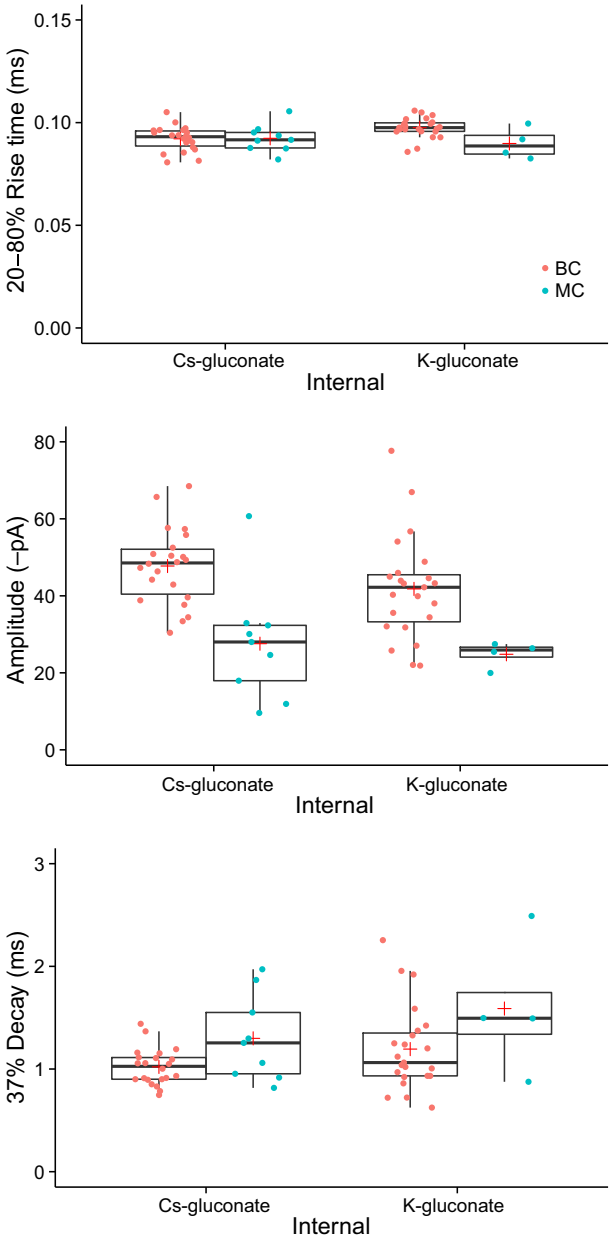

Figure 4.8: **Comparison of of fast rising mEPSCs from BCs and MCs.** Box-and-whisker plots for 20-80% rise time, peak amplitude and 37% decay time of mEPSCs (rise time < 0.125 ms) from 45 BCs (red symbols; 22 Cs-gluconate and 23 K-gluconate) and 13 MCs (cyan symbols; 9 Cs-gluconate and 4 K-gluconate). Box-and-whisker plots as described in Figure 4.7. For results of two-way ANOVA, see text.

include posttranslational modification of the receptors, but could more equally well reflect the influence of auxiliary subunits, TARPs or CNIHs (see Chapter 1).

As elaborated in the Introduction (Chapter 1), native AMPARs are modulated by their interaction with TARPs such as γ-2 (stargazin). TARP γ-2 mRNA is found in L5 of the mouse cortex (Fukaya et al., 2005) and antibody labelling has shown that this is specifically expressed in cortical INs, including PV-positive INs (Maheshwari et al., 2013; Tao et al., 2013). As γ-2 is known to slow recombinant AMPAR deactivation (channel closure following agonist removal) (Priel et al., 2005), γ-2 could play a role in setting mEPSC decay time in BCs.

To determine whether γ-2 influences mEPSC kinetics in BCs, I made recordings from seven cells in four *stargazer* mice lacking γ-2 (Letts et al., 1998; Noebels et al., 1990). Although the cells were not morphologically reconstructed, as judged from 2PLSM stack projections of Alexa-594 fills, the cell morphologies were similar to those of BCs in WT animals. Additionally, the cells exhibited typical BC firing properties. They had fast, non-accomodating spiking (accomodation 16.8 ± 5.7 %), with a high spike threshold (–32.3 ± 1.9 mV), a narrow spike width (0.61 ± 0.05 ms) and a pronounced AHP (–21.0 ± 1.0 mV) (compare with Table 4.2).

For selected fast rising mEPSCs (rise time < 0.125 ms), the peak amplitude (47.6 ± 5.0 pA, range 30.1–65.8 pA), 20–80% rise time (0.096 ± 0.002 ms, range 0.088–0.103 ms) and 37% decay time (1.18 ± 0.08 ms, range 0.81–1.48 ms) were in the range of the values obtained for WT BCs (see section 4.8). Interestingly, these results agree with those of Tao et al. (2013), who found no change in mEPSC kinetics in fast-spiking PV-positive INs of prefrontal cortex following knockout of erbin – an interacting protein that governs γ-2 expression. These observations could suggest either that γ-2 plays no role in synaptic AMPARs in cortical INs or, more likely, that other TARPs offer a degree of redundancy that maintains normal kinetics when γ-2 is lost (Menuz et al., 2008). Indeed Fukaya et al. (2005) found that γ-3, γ-4, γ-7 and γ-8 were also present in cortex L5. Alternatively, loss of γ-2 could lead to the synaptic expression of AMPARs with a different subunit composition (Bats et al., 2012) or different association with other auxiliary proteins (such as cornichons; Schwenk et al. 2009), resulting in no overall change in kinetics or amplitude. This could be examined using *in situ* hy-

bridization or antibody labelling. Of note, while mEPSC kinetics were not altered in INs of *erbin*$^{-/-}$ mice, the amplitude of events was reduced by ~20% (Tao et al., 2013). I did not obsevere such a reduction. Although it is possible that knockout of erbin has effects not seen with a simple loss of γ-2, it is also possible that this could reflect the difference in the age of the animals used (P14–P21 versus 2–3 months). Of note, a 2-fold decrease in the dendrite/soma expression ratio of GluA4 in PV-positive INs of somatosensory cortex has been reported for adult *stargazer* mice (Maheshwari et al., 2013), consistent with defecits in dendritic (synaptic) AMPAR trafficking in older animals.

Interestingly, I did observe a reduction in the frequency of mEPSCs in BCs of *stargazer* mice. For selected 'uncontaminated' events the frequency was reduced from 4.47 ± 0.31 Hz to 0.98 ± 0.11 Hz (n = 45 and 7, respectively; $p < 0.0001$, Welch two sample unpaired t test). In fact, the extent of this change is likely an underestimate, as the effect of eliminating closely timed events would be greater for the WT recordings. Studies by Leitch and colleagues (Leitch et al., 2009; Richardson and Leitch, 2005) in the cerebellum showed that in the *stargazer* mouse there were fewer glutamate-containing vesicles adjacent to active zones, as well as fewer docked vesicles. This was attributed to loss of brain-derived neurotrophic factor (BDNF). Loss of BDNF in *stargazer* is thought to be specific to the cerebellum (Qiao et al., 1996), thus it can not explain the reduced mEPSC frequency I observed in the *stargazer* BCs. Further studies would be required to resolve this issue. Potentially, loss of γ-2 could affect synapse development or function such that the lower frequency of mEPSCs could reflect the presence of fewer excitatory synapses or a reduced rate of spontaneous vesicle fusion.

4.2.3 Rectification of BC mEPSCs

Receptors that lack GluA2 are blocked by endogenous intracellular polyamines at positive membrane potentials, resulting in inwardly rectifying currents (Bowie and Mayer, 1995; Geiger et al., 1995; Kamboj et al., 1995; Koh et al., 1995b). In an attempt to asses the prevalence of CI- and CP-AMPARs in the two IN types, I recorded mEPSCs at –60 mV and +60mV. Recordings were made with Cs-gluconate internal and with

the addition of TEA to the bath to block voltage-gated K^+channels at positive potentials. First, I recorded currents in the absence of added intracellular spermine, using an internal solution containing 20 mM K_2ATP in order to buffer endogenous spermine (Rozov et al., 2012). Subsequently, I performed recordings with 0.5 mM spermine added to the intracellular solution, yielding a free spermine concentration of ~40 μM (Rozov et al., 2012). As shown in Figure 4.9, in the absence of added spermine mEPSCs were easily detected at +60 mV whereas in the presence of spermine mEPSCs were smaller and much less frequent at +60 mV. Averaging of all mEPSCs indicated inward rectification in the presence of spermine (Figure 4.9 C and D).

As the SD of the background noise generally increased at +60 mV, small mEPSCs might be expected to fall below the detection threshold of 2.5 x SD, artificially increasing the mean amplitude at the positive voltage. This would lead to an overestimate of RI (i.e. an underestimation of rectification). Accordingly, to quantify mEPSC rectification, I calculated $RI_{+60/-60,\,cm}$ as the ratio of 'count-matched' mEPSC conductances according to

$$\frac{\bar{I}_{\mathrm{p}}/(60-V_{\mathrm{L}}')}{\bar{I}_{\mathrm{N,\,cm}}/(60-V_{\mathrm{L}}')} \tag{4.1}$$

where $\bar{I}_P$ is the mean mEPSC peak amplitude (from all n fitted events) at positive voltage, $\bar{I}_{\mathrm{N,\,cm}}$ is mean mEPSC peak amplitude at negative voltage (from the largest n fitted events), and V_{L}' is the correction for the liquid junction potential (measured as –11 mV). For this analysis I used an intermediate rise time cut-off of < 0.4 ms, as using a more stringent cut-off of 0.125 ms (as used in section 4.2.2) resulted in too few events at +60 mV in the presence of spermine in some cells. For nine BCs in the absence of spermine, $RI_{+60/-60,\,cm}$ was 1.31 ± 0.07. For twelve BCs with added intracellular spermine, the corresponding RI was 0.48 ± 0.03. This method of calculating RI with count-matched amplitudes is likely to underestimate rectification, as any quantal events mediated entirely (or largely) by CP-AMPARs would not be detected at positive potentials due to the block by spermine reducing their amplitude below the detection threshold.

An alternative approach is to measure rectification as the ratio of summed mEPSC amplitudes (the sum of peak currents from equal lengths of recordings at positive and

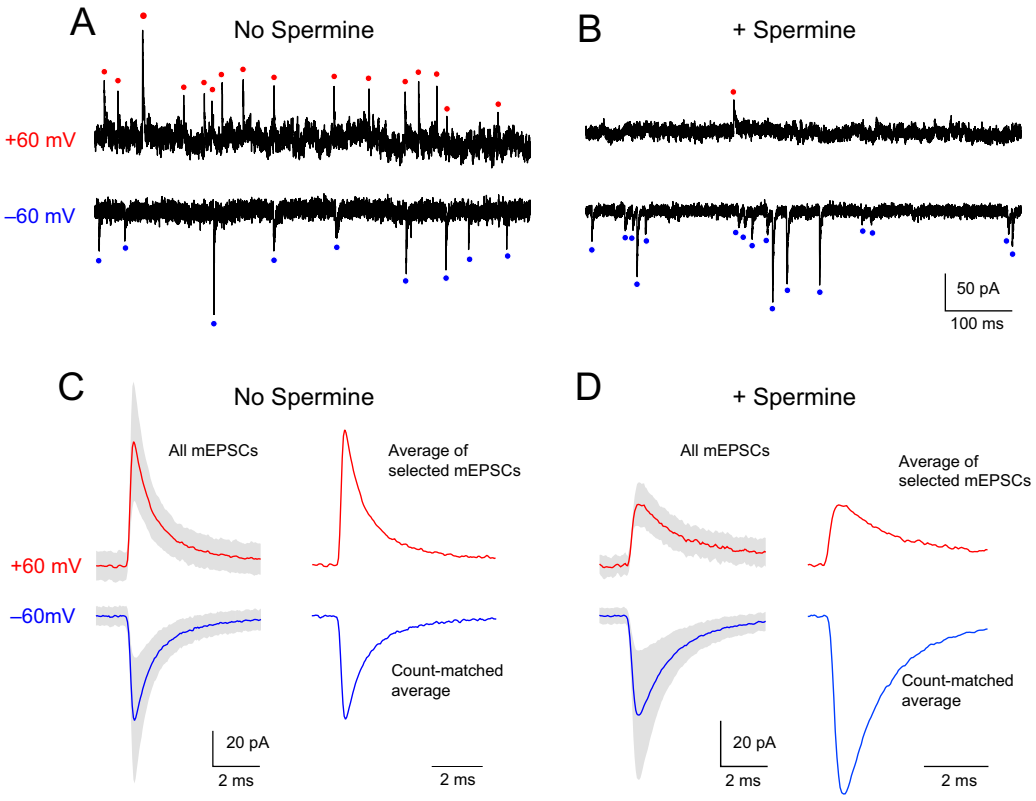

Figure 4.9: **Rectification of mEPSCs recorded from BCs.** Representative mEPSCs recorded from two BCs using internal solutions without (**A**) and with (**B**) added spermine. mEPSCs were detected using a threshold of 2.5 x the SD of the baseline noise. Coloured dots denote identified mEPSCs at –60 mV (blue) and +60 mV (red). (**C**) Left, the average of all accepted mEPSCs from the BC in A at +60 (n = 318) and –60 mV (n = 355) in the absence of spermine. The shaded areas denote the SEM. To the right are average fast-rising mEPSCs (20-80% risetime < 0.4 ms) recorded from the same cell at +60 mV and the count-matched average at –60 mV. Rectification index $RI_{+60/-60,\,cm}$ was calculated as described in the text and was 1.7. (**D**) Same as C, but from a cell recorded with intracellular spermine. The number of mEPSCs averaged at positive and negative voltages in the left hand panels were 96 and 516, respectively. For this cell $RI_{+60/-60,\,cm}$ was 0.44. Of note, in the presence of spermine, count matching the negative mEPSCs to the largest mEPSCs recorded at +60 mV had a substantial influence on the amplitude.

negative voltages, corrected for driving force) according to

$$\frac{\sum I_{\mathrm{P}}/(60 - V_{\mathrm{L}}^{'})}{\sum I_{\mathrm{N}}/(-60 - V_{\mathrm{L}}^{'})} \tag{4.2}$$

where I_{P} is the peak amplitude of individual fitted mEPSCs at positive voltage, I_{N} is the peak amplitude of individual fitted mEPSC at negative voltage, and V_{L}' is the correction for the liquid junction potential. With this method, the full range of potential rectification at individual synapses is taken into account, including those at which no currents would be detected at +60 mV should the block by spermine reduce the mEPSC amplitude below 2.5 x SD (resulting in a notional RI of 0). This combined use of 'count-matched' and 'summed' analysis is taken from earlier work on cerebellar stellate cells by Bats et al. (2012). For nine BCs in the absence of spermine, $\mathrm{RI}_{+60/-60,\,\mathrm{cm}}$ was 0.91 ± 0.08. For twelve BCs with added intracellular spermine, the corresponding RI was 0.09 ± 0.03. The result of this analysis was qualitatively comparable to that obtained using count-matching, and both support the view that CP-AMPARs are present at excitatory synapses onto BCs.

To address the concern that these results may be influenced by the choice of the rise time cut-off value (< 0.4 ms), I next sought to minimize any effect of dendritic filtering of distal mEPSCs by using mEPSC charge as a measure by which to determine rectification. Although some synaptic charge is lost due to voltage escape in the dendrite and the shunting effect of dendritic conductances, the charge of an mEPSC recorded at the soma is much less influenced by denritic filtering than is the current, particularly so for small synaptic conductances (Spruston et al., 1993). For mEPSCs in BCs the synaptic conductance was small (on average ~0.8 nS at –60 mV). For each mEPSC recorded at –60 and +60 mV, the charge (Q) was determined as the integral of the fitted waveform (see Chapter 2). This was determined as $Q = \int_{t_o}^{t_{end}} I\ dt$, where t_0 is the start of the mEPSC and t_{end} is the end following recovery to baseline, typically 20 ms. At –60 mV the mean mEPSC charge ranged from 52–128 fC. Rectification was calculated as described for currents, with Q replacing I (see equations 4.1 and 4.2). Both count-matched- and summed charge analysis revealed that, independent of dendritic filtering, synaptic AMPARs in BCs displayed rectification. Thus, in the

presence of intracellular spermine mEPSC rectification ($RI_{+60/-60,\ cm}$ 0.25 ± 0.02 and $RI_{+60/-60,\ sum}$ 0.09 ± 0.03; mean ± SEM) was significantly greater than in the absence of spermine ($RI_{+60/-60,\ cm}$ 0.82 ± 0.08 and $RI_{+60/-60,\ sum}$ 0.96 ± 0.12; both $p < 0.001$) (see Figure 4.10 on the next page). Overall, these results suggest that CP-AMPARs are present at excitiatory synapses onto visual cortex L5 BCs.

4.2.4 Rectification of MC mEPSCs

I next repeated the rectification experiments in MCs, in an attempt to determine whether CP-AMPARs were similarly expressed at synapses onto these cells. Unfortunately, when held at positive voltages MCs often exhibited clear indications of poor space-clamp (Spruston and Johnston, 2008; Williams and Mitchell, 2008), with evidence of the activation of voltage-gated calcium channels as a result of voltage escape in the dendrites. Although my 2PLSM morphological analysis revealed no difference in the distance to the most distal dendritic compartment, dendrite hull width or dendrite hull height between MCs and BCs, reconstructions using biocytin have shown that the total dendritic length of MCs in L5 of the rat cortex is ~20% greater than that of BCs (Kawaguchi et al., 2006). Moreover individual MC dendrites (in L2/3 at least) can be substantially longer than those of BCs (Kawaguchi et al., 2006; Kubota et al., 2011). Additionally, my data showed that the distance to the most distal axonal compartment in MCs is nearly twice that in BCs (see Chapter 3). Thus, it is likely that morphological features contributed to poor space clamp. Moreover, the presence of dendritic T-type calcium channels in L5 MCs is well established, and these channels support low-threshold calcium spikes in MCs firing in burst mode (Goldberg et al., 2004).

Although the regenerative currents tended to inactivate during repeated sweeps, both with continuous (+60 mV) and interleaved protocols (+60/–60 mV) (see Chapter 2), their presence indicated inadequate voltage clamp of (distal) dendrites. Nevertheless, I attempted to examine rectification of mEPSCs with fast rise times that were assumed to arise from perisomatic locations. As described above, mEPSCs in MCs are smaller than those in BCs (see section 4.2.2 on page 94). This introduced additional difficulties for their detection at +60 mV where the SD of the background noise was increased

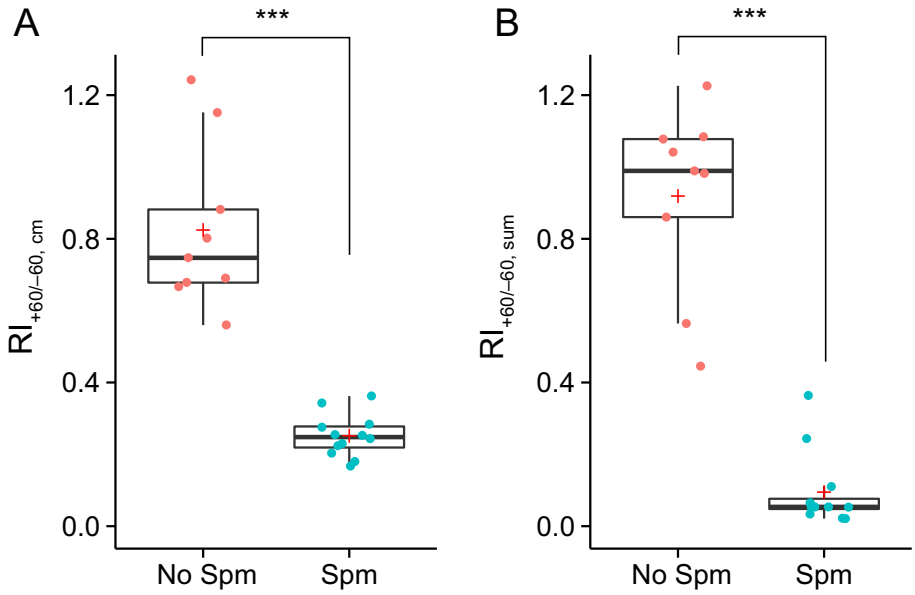

Figure 4.10: **RI determined from the measurement of charge.** (**A**) Boxplot of RIs for BCs recorded with Cs-gluconate internal, with and without added spermine. $RI_{+60/-60,\,cm}$ was calculated as the ratio of 'count-matched' mEPSC charges. (**B**) Same as A, but with RI calculated as ratio of 'summed' mEPSC charges. Box-and-whisker plots as described in Figure 4.7 (*** $p < 0.001$, Welch two sample *t* test).

above that at –60 mV – from 2.5 pA (range 2.2–3.1 pA) to 4.2 pA (range 2.5–5.3 pA) (n = 10).

Even when I sought to resolve events at +60 mV in control conditions with intracellular spermine buffered with high K_2ATP (see Chapter 2), where there should be no inward rectification, event detection proved difficult. For this reason, I initially assessed various approaches in an attempt to appropriately detect mEPSCs and guage their rectification; *a*) a variable amplitude threshold (a multiple of the standard deviation of the background noise, as used above), and *b*) a scaled template algorithm. Having recorded from ten MCs (identified on morphological criteria; see Chapter 3), I first compared these two methods.

Using a variable threshold of 2.5 x SD of the background noise (see section 4.2.3), reliably detected events at –60mV, but the number of events detected at +60 mV was always much greater than expected (if one assumed an unaltered release probability) suggesting the detection of false-positives. In an attempt to increase selectivity at positive potentials while retaining sensitivity for small events I next used a scaled template detection algorithm (Clements and Bekkers, 1997). The template waveforms were modeled on the time course of averaged spontaneous events and consisted of events with an exponential rise (τ = 0.2–0.4 ms) and decay (τ =1–5 ms). An important feature of this approach is that it takes the noise standard deviation into account, only selecting events that cross a certain threshold level. I used values for the 'detection criterion' of 2.5–4, close to the optimal value suggested by Clements and Bekkers (1997) that should ensure sensitivity of detection with a low rate of false positives. With this method, the number of detected events at +60 mV was dramatically reduced, but while for some cells the frequency of events at +60 mV was less than that seen at –60 mV in others it remained much greater than at –60 mV. Such variability was also seen in the analysis of recordings with intracellular spermine.

Because of the difficulties with detecting mEPSCs at +60 mV, I chose not to calculate the RI for MCs. Even though some events at +60mV were clearly mEPSCs – in those cases where the AMPAR antagonist NBQX was applied I observed a clear decrease in event frequency – I was not confident that I could obtain a reliable measure of rectification. Clearly, using mEPSCs to assess synaptic AMPAR rectification

is not appropiate in MCs. Interestingly, my collaborators Txomin Lalanne and Jesper Sjöström at McGill when making paired recordings of PC to IN connections were able to detect unitary EPSCs at positive voltages. This was likely because the currents were time-locked and averaged. Importantly, they found that unitary PC-BC EPSCs were rectifying, while unitary PC-MC EPSCs had linear current-voltage relationships (Lalanne et al., 2014; Oyrer et al., 2013).

4.2.5 Block of BC mEPSCs by Naspm

If mEPSCs in BCs are mediated (at least in part) by CP-AMPARs they should display sensitivity to CP-AMPAR blockers such as the wasp polyamine toxin PhTx (Osswald et al., 2007), JSTX (Blaschke et al., 1993) or the synthetic analogue of JSTX, Naspm (Koike et al., 1997). These blockers generally show use- and voltage-dependence of block, with supression becoming less prominent with depolarization (Koike et al., 1997; Washburn and Dingledine, 1996). I recorded from BCs with a K-gluconate internal (to allow a functional indication of IN type), and monitored mEPSCs at –60 mV while bath applying Naspm. In line with previous studies (for example, Purgianto et al., 2013 and Studniarczyk et al., 2013) I used a concentration of 100 μM and waited for 20 minutes, after which time the drug effect had reached a steady state.

To assess the Naspm block, I measured summed mEPSC Q – the sum of charge from 100 s recordings made before and after 20 minutes of drug application. This approach was chosen in order to avoid potential underestimation of block that could occur with simple averaging or count-matching if events arose from a mixture of synapses with CI- or CP-AMPARs. These recordings were made without the addition of intracelluar spermine to ensure any GluA2-lacking CP-AMPARs were available to be blocked by Naspm (Rozov et al., 2012). As shown in Figure 4.11, Naspm produced a significant block of mEPSC summed charge.

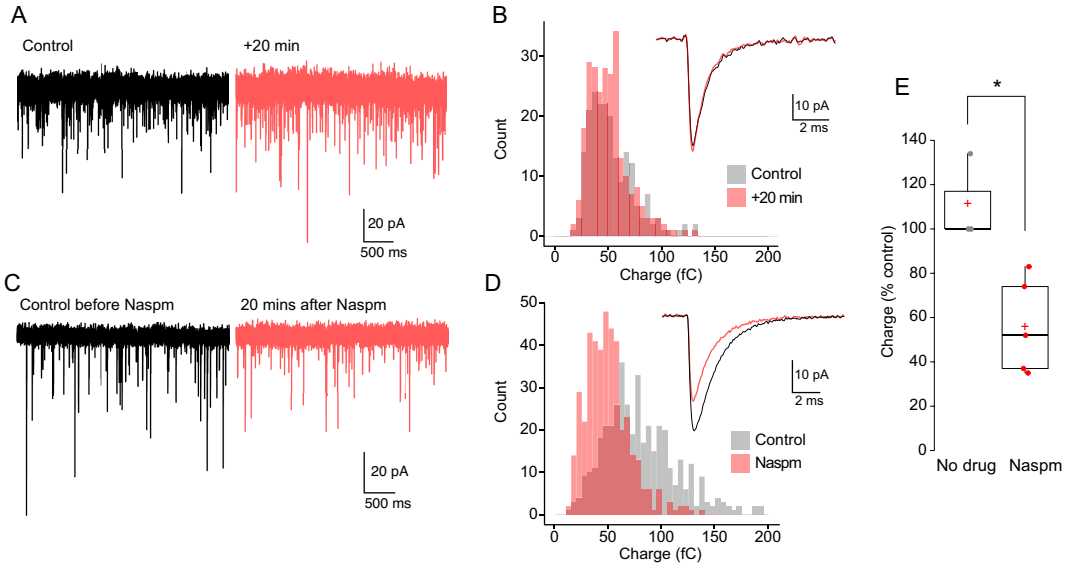

Figure 4.11: **Partial block of BC mEPSCs by Naspm suggests the presence of CP-AMPARs.** (**A**) Representative control mEPSCs (–60 mV) (black) and mEPSCs recorded after 20 min (red). (**B**) Charge histograms and mean mEPSCs (202 control mEPSCs and 255 events after 20 minutes) for the cell shown in A. (**C**) Same as A, but with application of 200 μM of the CP-AMPAR blocker Naspm. (**D**) Same as B, but for the cell in C (419 control mEPSCs and 423 events after 20 minutes in Naspm) . (**E**) Pooled data from 3 cells without drug and 5 cells with Naspm. Box-and-whisker plots as decsribed in Figure 4.7 on page 100 (* $p < 0.05$; Welch two-sample t test).

This result was supported by a separate analysis that did not involve event detection or selection. In one representative control recording and in one representative Naspm recording I determined synaptic charge transfer using a method based on that of Glykys and Mody (2007). I divided each record into 100 ms episodes, generated all-point amplitude histograms and fit these with a single-sided Gaussian (to the most-positive current values). For each episode the peak of the Gaussian fit was taken as the baseline current value, and the integral of the section of histogram not fitted by the Gaussian was taken as the charge carried by the mEPSCs. The phasic charge per episode was averaged for control recordings and for those obtained after 20 minutes (with or without Naspm). In the two cells examined, the fraction of charge remaining was 0.65 and 0.93 with- and without Naspm (the corresponding values for the original analysis were 1.00 and 0.74) (see Figure 4.12).

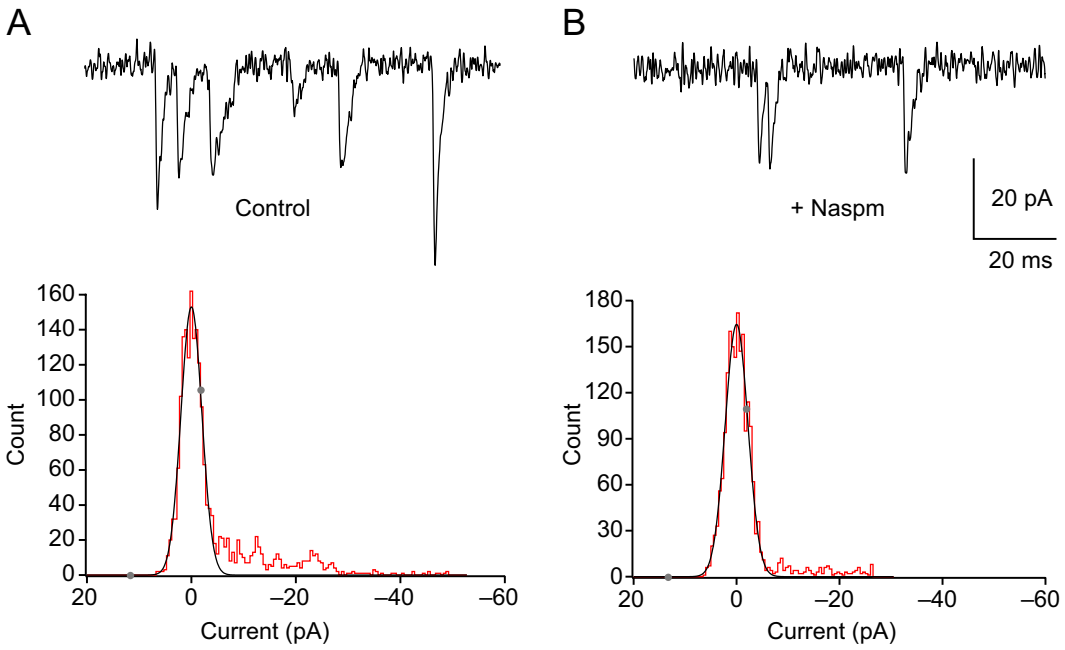

Figure 4.12: **Reduction in phasic charge transfer by Naspm.** (**A**) Representative 100 ms episode taken from a period of recording in control external solution (–60 mV). The all-point histogram below shows the method of charge calculation. As described in the text, the integral of the histogram outside the fitted one-sided Gaussian (fit between grey circles) was taken as the charge carried by the mEPSCs. (**B**) Same as A but for a representative 100 ms episode 20 mins after application of 100 μM Naspm. The average charge in control and Naspm was calculated from 950 episodes in each condition.

4.3 Discussion

The results presented in this chapter suggest the presence of CP-AMPARs at excitatory connections onto BCs in layer 5 of the visual cortex. The rectification for BC mEPSCs in the presence of spermine, independent of the method of assessment of RI, strongly supports this view. While the RI estimated by count-matching (mean 0.25) is likely to underestimate the rectification (see section 4.2.3), the RI calculated from the summed mEPSC charges (mean 0.09) is likely to overestimate the rectification. The fact that these two methods gave slightly different values suggests possible heterogeneity among synapses in the prevalence of CP-AMPARs. Of note, the modest difference is much less than seen in the study of Bats et al. (2012) that asssed mEPSC rectification using these two approaches and argued for heterogeneity among excitatory synapse onto cerebellar stellate cells. Although it is difficult to compare recombinant and synaptic data obtained under different conditions, what does such a comparison of rectification say about the relative proportion of CI- and CP-AMPARs in BCs? For recombinant CP-AMPARs (GluA1 or GluA4) $RI_{(+60/-60mV)}$ is ~0.2 without γ-2 and ~0.6 with γ-2, whereas for CI-AMPARs (GluA2/4) $RI_{(+60/-60mV)}$ is ~0.75 both with and without γ-2 (Soto et al., 2007). The RI values I obtained for BCs with spermine were 0.25 (count-matched data) and 0.09 (summed). At face value this would suggest that >90% of the AMPARs in BCs were calcium permeable.

The fact that I obtained only an incomplete block of BC mEPSCs by Naspm (see section 4.2.5) would be consistent with these cells expressing a mixture of CP- and CI-AMPARs. However, this simple interpretation is complicated by the need to understand *a*) how much block one could achieve with a pure population of CP-AMPARs, and *b*) to what degree the extent of block is affected by the frequency of activation at individual synapses.

Regarding the expected degree of block for CP-AMPARs, various studies have shown that with PhTx-433 or Naspm complete or near-complete block can be achieved for both recombinant CP-AMPARs (Jackson et al., 2011; Washburn and Dingledine, 1996) and for native receptors in cells lacking GluA2 (Koike et al., 1997; Sara et al., 2011; Studniarczyk et al., 2013). The issue of use-dependency, and thus the impact of the

frequency of release at individual synapses, is more complex. The very nature of quantal events – reflecting random release events across all individual synapses – means that for a given frequency of mEPSCs recorded at the soma, the average frequency of release at any individual synapse could be only a tiny fraction of this. The precise frequency of mEPSCs at a given synapse will depend on the total number of synapses received by the cell and on any heterogeneity of release probability (e.g. Holderith et al., 2012). Interestingly, a study of cultured hippocampal neurons Sara et al. (2011) reported a full block of mEPSC charge transfer in GluA2-lacking neurons within 5 minutes of application of 100 μM PhTx-433. In this study the frequency of mEPSCs was ~3 Hz and, surprisingly, the speed and extent of block was not increased by increasing the mEPSC frequency ~2-fold (switching from 2 to 10 mM Ca^{2+}). Of course, I cannot assume that hippocampal neurons in culture have the same number of excitatory synaptic contacts as BCs in slices, or that Naspm behaves exactly as PhTx-433 (Washburn and Dingledine, 1996). Nevertheless, these observations would be consistent with the view that the mEPSCs in BCs do not arise from a pure population of CP-AMPARs.

My findings were confirmed by the work of my collaborators Txomin Lalanne and Jesper Sjöström (Lalanne et al., 2014; Oyrer et al., 2013). They made paired recordings from PCs and BCs and from PCs and MCs also in L5 of visual cortex from P14-P21 mice (see Figure 4.13). Similar to my results with mEPSCs, they found that unitary currents at PC-BC synapses were rectifying (RI ~0.15). In additional experiments they also examined rectification of currents evoked by the uncaging of AMPA. These experiments also revealed strong rectification in BCs (RI ~0.2). Moreover, PC-BC synapses were also sensitive to Naspm, with 100 μM Naspm producing a block of ~50%. Although Naspm (and JSTX) can produce some non-specific block of CI-AMPARs (Blaschke et al., 1993; Studniarczyk et al., 2013), when considered together with our joint rectification data, these results are consistent with the presence of postsynaptic CP-AMPARs. While the experiments I carried out unfortunately left unanswered the question of whether MCs express CP-AMPARs, my collaborators were able to show, both in paired recordings of PC-MC connections and with AMPA uncaging, that the synaptic and non-synaptic AMPARs in MCs were non-rectifying (RI ~1 in both cases). Thus, my results, together with the findings of my collabora-

tors, are strongly suggestive of the presence of postsynaptic CP-AMPARs in BCs, but not in MCs. Recently, it has been suggested that spontaneous and evoked glutamate release activates non-overlapping populations of receptors (Atasoy et al., 2008; Sara et al., 2011; Sutton and Schuman, 2009) or can occur preferentially at different sets of synapses (Peled et al., 2014). Our data on BCs suggests that glutamate released in an action potential-dependent or action potential-independent fashion activates AMPARs with similar functional properties.

Relationship to previous studies of BCs

Previous functional studies, in other regions (both cortex and hippocampus) have also identified the presence of CP-AMPARs in BCs. For example, the classic studies of Jonas and colleagues showed clear inward rectification of currents in outside-out somatic patches from BCs in slices of the dentate gyrus of the rat (Geiger et al., 1995; Koh et al., 1995b). Similar results were obtained in equivalent experiments on neocortical fast-spiking non-pyramidal cells in slices of frontal cortex of rat (Angulo et al., 1997). In two of these studies, the functional properties were correlated with a low relative abundance of GluR2 (GluRB) mRNA, as judged by single-cell RT-PCR (Angulo et al., 1997; Geiger et al., 1995). More recently, a study by Wang and Gao (2010) showed that the majority of fast-spiking INs in the prefrontal cortex of the rat exhibit evoked EPSCs that are inwardly rectifying, suggesting the presence of CP-AMPARs. The same authors showed a significantly increased rectification in adolescent- (P31-P63) compared to juvenile- (P15-P28) rats. This is of interest given that my recordings were from relatively young mice. The existence of CP-AMPARs in PV-postive INs in the prefrontal cortex was additonally confirmed by Tao et al. (2013), who showed a pronounced inward rectification of evoked EPSCs in adult mice. Finally, CP-AMPAR-mediated EPSCs have also been demonstrated in the mouse barrel cortex (Hull et al., 2009).

The study by Hull et al. (2009) found that thalamocortical inputs evoke CP-AMPAR-mediated EPSCs in fast-spiking INs but not in regular-spiking INs. It is interesting to compare this evidence for postsynaptically-determined differences with the earlier

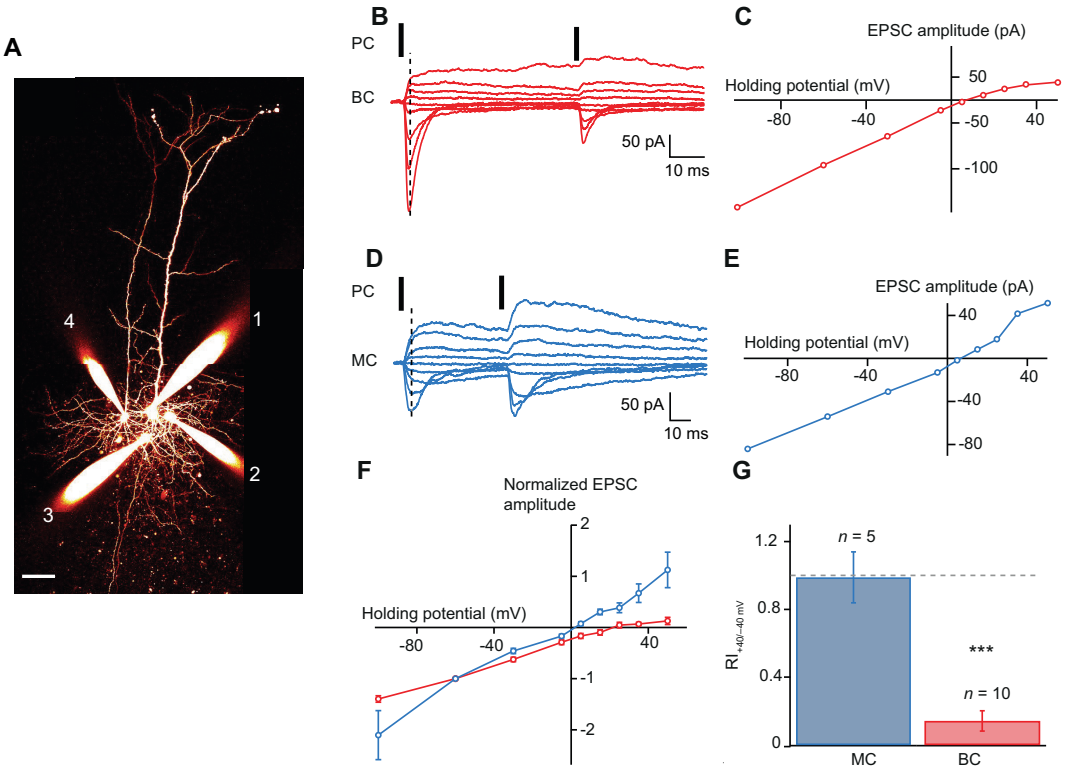

Figure 4.13: **Paired recordings of PC-BC and PC-MC connections.** (**A**) Maximal intensity projection of fluorescence obtained with 2PLSM showing four Alexa-594-filled neurons in L5 of mouse visual cortex. Image shows two PCs (1 and 4) and two INs (2 and 3). Scale bar 100 μm. (**B**) Family of currents elicited in a BC by action potentials (black bars) in presynaptic PC (average of 6 sweeps). (**C**) Current-voltage relationship of the currents shown in B (at the time indicated by the vertical dashed line). (**D, E**) Same as B and C but from a PC-MC pair (10 sweeps). (**F**) Pooled data showing average *I-V* plots for PC-BC and PC-MC pairs. (**G**) Bar plot showing estimates of rectification for the two IN types, calculated as the ratio of currents at positive and negative voltages; +40/–40, corrected for measured liquid junction potential. Figure provided by Txomin Lallane and Jesper Sjöström.

study of Tóth and McBain (1998) that found evidence for AMPAR expression that appeared to be determined by the nature of the afferent inputs. Thus, they found that the synaptic expression of CP-AMPARs in single hippocampal INs (as judged by PhTx-433 block) depended on the nature of the presynaptic neuron, with mossy fibre-evoked EPSCs being mediated by PhTx-sensitive CP-AMPARs but EPSCs arising from CA3 PC inputs being mediated by PhTx-insensitive CI-AMPARs. My results extend this body of work by demonstrating that CP-AMPARs are present at synapses onto BCs in L5 of the mouse visual cortex. The potential roles of CP-AMPARs in fast-spiking BCs will be considered in Chapter 5.

Comparision with MCs

My data, together with that of my collaborators, suggests the presence of CP-AMPARs on excitatory synapses onto BCs but CI-AMPARs at excitatory synapses onto MCs (Lalanne et al., 2014; Oyrer et al., 2013). The potential significance of this difference in AMPAR subtypes between these two IN classes in terms of their circuit function will be elaborated in Chapter 6. Regardless of their ultimate functional roles, it is interesting to consider how AMPAR expression may be linked to the development of BCs and MCs. Fate mapping studies have shown that both PV-positive- and SOM-positive cortical INs originate from the MGE (Kessaris et al., 2014; Wonders and Anderson, 2006), with PV-positive cortical INs primarily being generated within the ventral MGE, and SOM-positive cortical INs primarily originating from the dorsal MGE (Fogarty et al., 2007; Wonders et al., 2008). This is of interest as, in the hippocampus, it has recently been shown that the lineage of INs determines the nature of the AMPARs they express. Thus, Matta et al. (2013) has shown that excitatory synaptic inputs to MGE-derived INs activate GluA2-lacking AMPARs, while excitatory synaptic inputs to CGE-derived INs activate GluA2-containing CI-AMPARs. As both cortical BCs and MCs derive from MGE progenitors, our findings that these two IN types have different AMPAR subtypes at their excitatory inputs appears at odds with the picture emerging from the hippocampus. However, it is important to note that gene expression profiling has revealed considerable molecular heterogeneity between the dorsal and ventral MGE (Wonders et al., 2008). Moreover, as pointed out by Matta et al. (2013), an absolute origin-dependent rule for the expression of CP- versus

CI-AMPARs is probably too simplistic, as individual INs have been demonstrated to express CP- and CI-AMPARS at synapses innervated by distinct afferent inputs (Tóth and McBain, 1998).

In the following chapter I will describe immunohistochemical experiments that address the AMPAR subunit expression (more precisely that of GluA2) in the two IN types.

Chapter 5

Immunohistochemical characterisation of GluA2 expression

5.1 Introduction

As described in previous chapters, the presence or absence of edited GluA2 subunits in an AMPAR tetramer dictates whether or not the receptor will be of the CI- or CP-subtype. Thus, the balance of AMPAR receptor subtypes expressed within any one cell will, to a large extent, reflect the abundance of GluA2 (Jonas et al., 1994; Szabo et al., 2012). As the electrophysiological data from my own studies and those of my collaborators suggested the presence of CP-AMPARs in BCs but the expression of predominantly CI-AMPARs in MCs (Lalanne et al., 2014), one might predict a greater expression of GluA2 in MCs than in BCs. In order to assess the relative expression of GluA2 in BCs and MCs within L5 of the mouse visual cortex, I sought to examine the pattern of GluA2 immunoreactivity in these INs, as identified by the presence of PV and SOM, respectively.

As discussed in Chapter 1, neocortical INs can be classified according to their neurochemical expression profile. However, a general consensus has been slow to emerge, in part because different studies have sometimes taken very different approaches. For example, attempted comparisons among different species (rat, mouse, human etc), at different levels of resolution (region- and layer-specific or more indiscriminate) or

with different markers (protein versus mRNA), have often led to confusion or contention (see section 5.5). Nevertheless, SOM and PV are commonly used as key neurochemical markers to separate different IN groups. Firstly, PV and SOM label predominantly inhibitory GABAergic neurons (Gonchar et al., 2007; Kubota et al., 1994; Kawaguchi and Kubota, 1997) and hardly ever non-GABAergic neurons (Jinno and Kosaka, 2004). Secondly, they constitute two non-overlapping molecular markers (Gonchar and Burkhalter, 1997; Gonchar et al., 2007; Kawaguchi and Kubota, 1997; Kubota et al., 1994) (reviewed in Ascoli 2008; DeFelipe et al. 2013; Toledo-Rodriguez et al. 2005). More specifically, in mouse visual cortex, PV and SOM are non-overlapping, both during development (Xu et al., 2006; Gonchar et al., 2007; Pfeffer et al., 2013) and in the adult (Xu et al., 2010). Here, SOM immunoreactive GABAergic INs are first seen at P0, while PV immunoreactive INs appear later (P13) (Gonchar et al., 2007). At P16 ~40% of INs express SOM and 40% PV, while in the adult the corresponding precentages are ~30% and ~50% (Gonchar et al., 2007). Thus, together these markers identify the majority of GABAergic INs.

I chose to answer the question about levels of GluA2 expression within the major L5 IN players by labelling visual cortical slices with specific primary antibodies (namely anti-PV, -SOM and -GluA2) and fluorescently labelled secondary antibodies. By chosing different excitation and emission wavelenghts, the sequential visualization of all three cellular markers was possible.

5.2 GluA2 expression in PV and SOM interneurons

I examined immunolabelling in visual cortex layer 5. To broadly match my electrophysiological data, which was from the 3rd postnatal week (P14-21), I used slices from P21 mice and collected frozen slices from the microtome at approximately the same depth into the tissue block as used for slicing fresh tissue for acute slices for electrophysiology. Free floating sections (40 μm) were incubated with primary antibodies against PV, SOM and GluA2 then with secondary antibodies conjugated with various fluophores (see Chapter 2). This is illustrated schematically below (Figure 5.1).

Figure 5.1: **Schematic diagram illustrating the origin (species) and selectivity of the primary (1°) and secondary (2°) antibodies used for triple labelling of cortical sections for PV, SOM and GluA2.** Note, in order to avoid secondary antibodies cross reacting with other secondary antibodies, the primary antibodies were from different species (guinea pig, rat and rabbit) while the secondary antibodies were raised in a different species again (goat).

Identification of visual cortex L5

To identify the visual cortex, I first located the corpus callosum and focussed on the cortex slightly lateral to the posterior forceps and dorsal hippocampal commissure, above the external capsule (Lein et al., 2006). Between the pia and the corpus callosum, cortical layers were distinguished by subtle differences in the density of DAPI staining when viewed with the 10x objective (Figure 5.2), including a higher density of cell bodies in L4 in comparison to L5 (Tsiola et al., 2003). When viewed with a 20x objective L5 was characterised by large GluA2-immunoreactive PC soma surrounded by PV-immunoreactive puncta (Figure 5.2) (Kawaguchi and Kubota, 1997; Somogyi et al., 1998). No SOM-immunoreactive puncta were seen around the PC cell bodies, consistent with SOM-positive MC INs preferentially targetting distal dendrites (Kawaguchi and Kubota, 1997; Somogyi et al., 1998).

5.2.1 Triple labelling of PV, SOM and GluA2

The goal of my quantitative analyses was to determine the relative expression of GluA2 in PV-positive INs, SOM-positive INs and PCs. All of the antibodies produced reproducible labelling of cell bodies, but labelling of dendrites was not sufficiently clear to provide adequate descriptions of the dendritic morphologies. As I did not employ any synaptic markers, my comparison was restricted to counts of double-labelled cell bodies (e.g. Vissavajjhala et al. 1996).

PV and SOM displayed distinct somatic immunoreactivity, with the former showing strong, complete labelling (Moga et al., 2002; Vissavajjhala et al., 1996; Sommeijer and Levelt, 2012; Kawaguchi and Kubota, 1998) while the latter showed characteristic crescent-shaped peri-nuclear labelling only (Pesold et al., 1999; Kawaguchi and Kubota, 1996, 1998; Perrenoud et al., 2012). The majority of INs in the cortex of juvenile rodents are BCs, followed by MCs (Markram et al., 2004). Consistent with this, I always detected many more PV- than SOM-immunoreactive cell bodies. Although one might have expected the ratio of SOM:PV cells to be between 0.6:1–1:1 (see above; Gonchar et al. 2007), I obtained a ratio of 0.2:1 (three L5 stacks from each of three

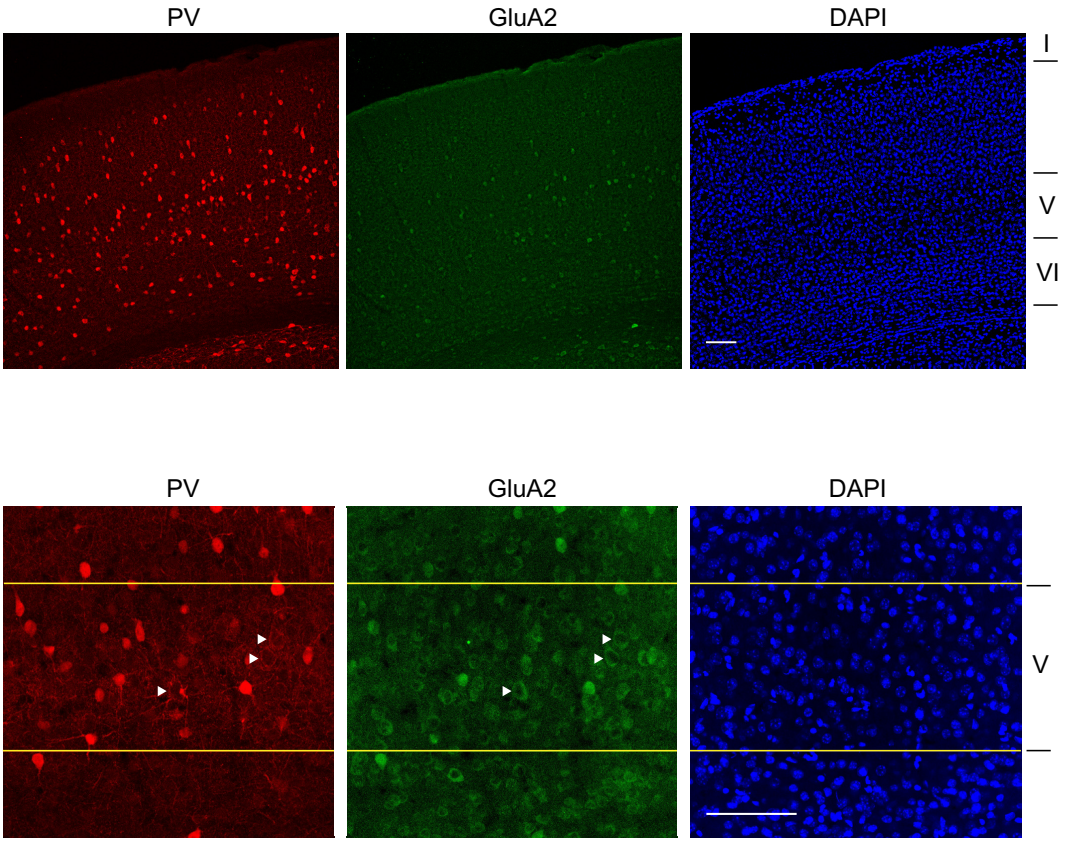

Figure 5.2: **Layer identification in visual cortex.** Coronal sections of visual cortex from P21 WT mouse. Top row shows three maximum intensity projection images from multiple optical slices of 3 μm step size (immunolabelled with antibodies against PV and GluA2 and stained with DAPI). Images were obtained with a 10x objective and have been background subtracted (for illustration purposes only). Layer identification is shown to the right. Scale bar 100 μm. Bottom row shows images from the same area but centered on layer V and obtained with a 20x objective. In this case only a single optical slice is shown. Arrowheads indicate selected PCs. Scale bar 100 μm. Sparse labelling for SOM neurons (see below) did not provide useful information on layering.

mice). This comparatively low ratio may be explained by the fact that I selected SOM-positive cells very conservatively (when chosing cells for assessing the presence of GluA2).

Triple labelling for PV, SOM and GluA2 is shown together with DAPI staining in Figure 5.3 on the next page. The upper row of images shows a PV-positive IN (arrowhead) and two nearby PV-negative PCs (asterisks). Both the PV-positive INs and the PCs are immunoreactive for GluA2 (in agreement with previous studies; Vissavajjhala et al. 1996; Petralia and Wenthold 1992; He et al. 2001 for PCs and Vissavajjhala et al. 1996 for PV-positive INs). The lower row shows images from the same stack, illustrating a SOM-positive IN (double arrowhead) and two nearby SOM-negative PCs (asterisks). Note that SOM backround labelling is pronounced, but that the SOM immunoreactive soma is very distinct. Again, both the PCs and the SOM-positive IN are immunoreactive for GluA2, with the expresssion in the IN less than that seen in the PCs.

To quantify GluA2 immunoreactivity across the two IN types, I measured the mean grey value in selected regions of interest (ROIs) centered on the cell bodies (see legend to Table 5.1 on page 128). The mean grey value is simply the sum of the grey values of all the pixels in each selected ROI divided by the number of pixels. For all cells, each mean grey measurement was higher than the mean background value. Of note, GluA2-labelling was much more variabe among PV-positive INs than SOM-positive INs. For example, in one slice mean grey values for GluA2 in the SOM INs varied between 43.8 and 71.0, while in PV INs the measure ranged from 46.4 to 179.9. Across all three animals, the CV of GluA2 mean grey value was significantly greater for PV INs compared to SOM INs (0.36 ± 0.05 versus 0.11 ± 0.02; $p = 0.00063$, Welch t test; $n = 7$ and 9, respectively). Consistently accross the three animals, GluA2 labelling intensity (background subtracted) had the following order PV INs > PCs > SOM INs. When normalised to PC GluA2 levels, the GluA2 labelling of PV-positive INs was more than double that of SOM-positive INs.

The results described above were unexpected, given my electrophysiological results and those of my colleagues (Lalanne et al., 2014). Most notably, it was surprising that the soma of PV-positive INs exhibited a greater intensity of GluA2 labelling than did PCs. Rather disturbingly, it appeared that many cells with the brightest GluA2

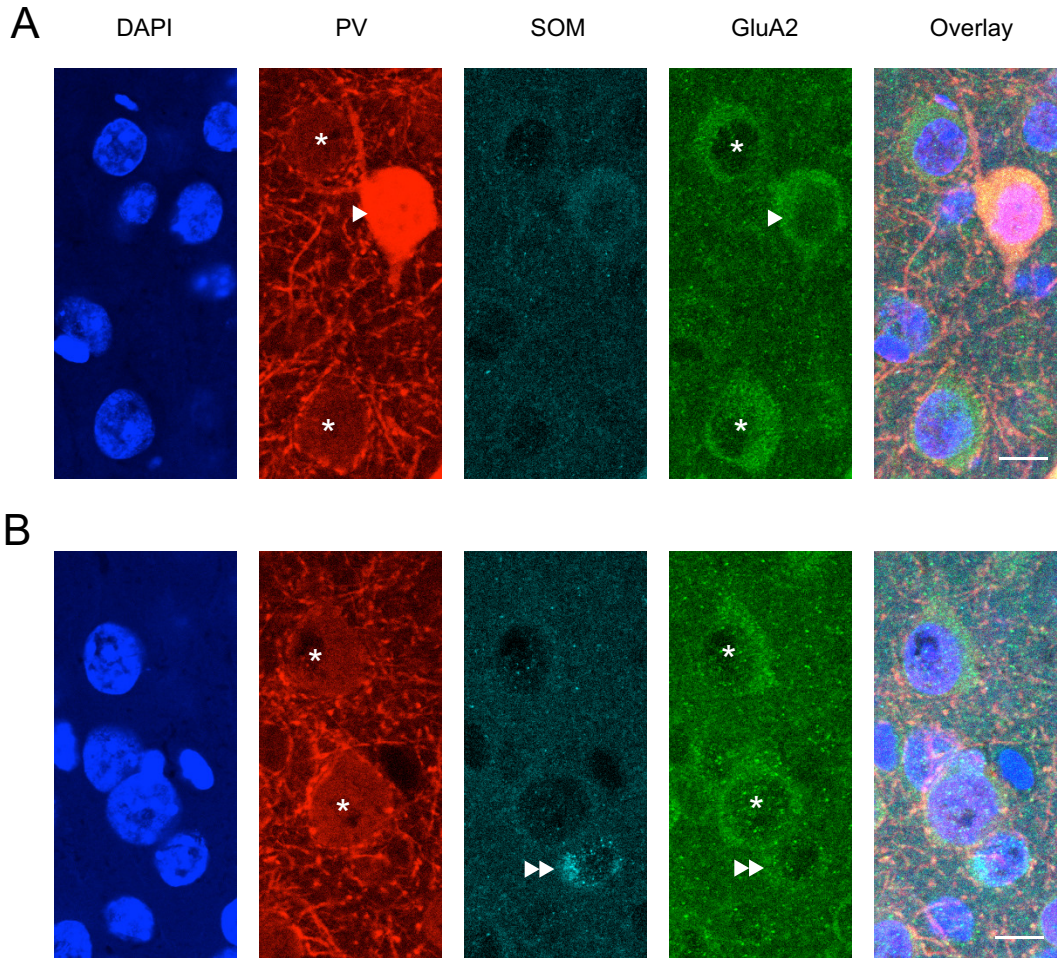

Figure 5.3: **Triple labelling for PV, SOM and GluA2.** Images of coronal sections of visual cortex from a P21 WT mouse obtained with a 40x objective. (**A**) Selected region of a single optical slices from L5 (stained with DAPI and immunolabelled with antibodies against PV, SOM and GluA2). The final image is an overlay of the previous four. Note the PCs surrounded by PV-positive puncta (asterisks) and the intensely labelled PV-positive IN soma with a typical round soma. Scale bar 10 μm. (**B**) Images from a different selected region of the same slice. Note the SOM-positive IN (double arrowhead). Scale bar 10 μm.

	Mean grey value			Normalised to PC	
	PC	PV	SOM	PV	SOM
Animal 1	68.8	72.3	27.9	1.07	0.42
Animal 2	48.5	64.3	22.4	1.35	0.46
Animal 3	39.9	58.3	28.6	1.54	0.79
Global average	52.4	65.0	26.3	1.32	0.56
SEM	8.6	4.0	2.0	0.14	0.12

Table 5.1: **GluA2 immunolabeling of PV- and SOM-positive interneurons.** Values shown are the average measurements from three slices per animal, in which mean grey values were determined from a single optical section with circular ROIs of ~3 μm diameter located on the soma. For PV-positive INs, the ROI was centred on the brightest region of PV labelling and the GluA2 intensity was taken from the same position. For SOM-positive INs, ROI was centered on the brightest expression (outside of the unlabelled nuclei) and, again, GluA2 intensity was taken from the same position. The GluA2 labelling in PCs was used to normalise the GluA2 intensity accross slices and animals. Here, GluA2 labelling was taken from the brightest region of the soma. Note, all measurements are background subtracted (average of at least 20 ROIs per stack).

immunofluorescence were also the brightest for PV. To quantify this, I examined the correlation between PV and GluA2 immunoreactivity. For each PV-positive IN, I measured the mean grey value for the brightest PV labelling and the mean grey level for GluA2 in the corresponding optical section.

Plots of mean grey level for PV against that for GluA2 are shown for three different mice in Figure 5.4 on the next page. There was a clear trend for the highest GluA2 labelling to be associated with the highest PV labelling (R_S = 0.52, 0.44 and 0.29).

The apparently greater expression of GluA2 in the INs most heavily immunoreactive for PV could reflect a developmental progression, particularly as it is known that PV expressing INs increase in number between eye-opening and adulthood (Gonchar et al., 2007). Although this possibility was considered attractive, control experiments (described below) suggest a more mundane explanation.

5.3 Technical considerations and antibody specificity

The above work was carried out under the assumption that the antibodies used were highly specific (as claimed by each of the suppliers). All the primary antibodies I employed have been widely used and, in certain cases, characterised using relevant controls, including use of preimmune serum, immunoabsorption, and labelling of transfected cells. The anti-PV antibody has been used previously by many studies, including, for example, by León-Espinosa et al. (2012) in the mouse neocortex, by Massi et al. (2012) in rat prefrontal cortex, by Antonucci et al. (2012) in the rodent hippocampus, and by Huang et al. (2013) in the mouse olfactory bulb. Likewise, the anti-SOM antibody has been used previously by Gonchar et al. (2007) in the mouse visual cortex, by Perrenoud et al. (2012) in the mouse barrel cortex, by Cammalleri et al. (2009) in mouse hippocampus, and by Xu et al. (2006) in the mouse cortex. Finally, the anti-GluA2 antibody was used by Shimuta et al. (2001) and by Fukaya et al. (2006) in the mouse hippocampus.

The major factors influencing the quality of immunohistochemical experiments, and the necessity for control experiments have been extensively reviewed (Fritschy, 2008;

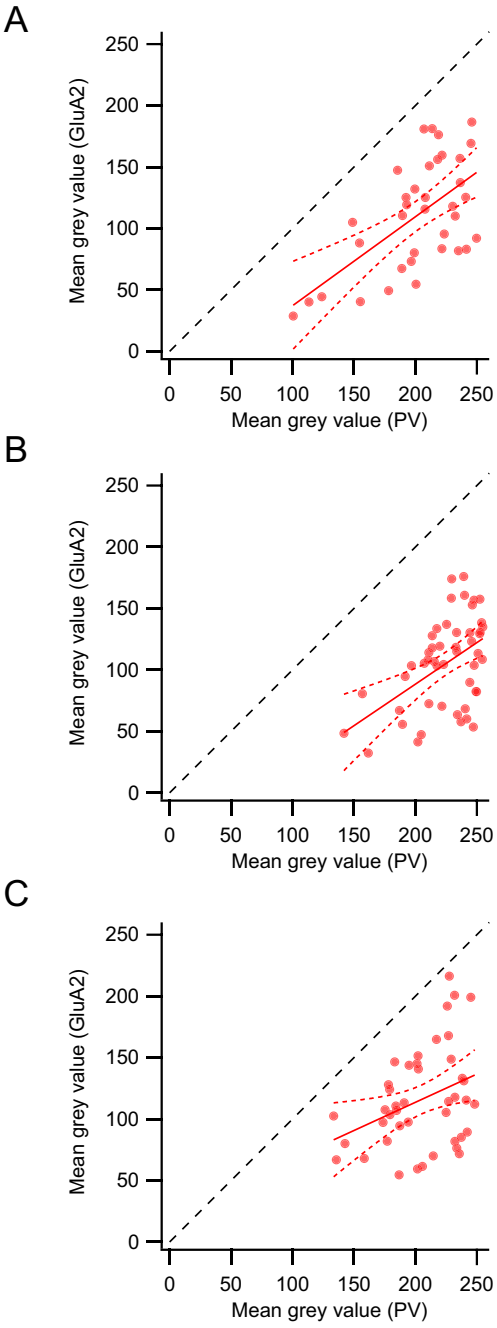

Figure 5.4: **Scatterplots illustrating the relationship between GluA2 and PV somatic labelling**. The three plots (A, B and C) are from single slices from each of three mice. Symbols denote background subtracted grey values (as described in the text). Solid lines (red) are linear fits and curved dashed lines (red) indicate the 95% confidence interval of the fit. The straight dashed lines (black) are lines of identity. In each case the significance of the relationship was tested using a Spearman rank order correlation test. (**A**) $n = 36$, $R_S = 0.52$, $p = 0.0011$.(**B**) $n = 49$, $R_S = 0.44$, $p = 0.0014$ (**C**) $n = 43$, $R_S = 0.29$, $p = 0.063$.

Rhodes and Trimmer, 2006; Lorincz and Nusser, 2008; Editors, 2011). Both primary and secondary antibodies can fail to bind to their targets or can bind non-specifically to other targets or tissue components. The primary antibodies I used have been widely tested (see above). However, to avoid potential misinterpretation of my results I performed various control experiments, specifically addressing the possibility of fluorescent cross-talk and secondary antibody cross-reactivity.

5.3.1 Tests of fluorescence crosstalk

Crosstalk (also known as bleed-through) can occur when two (or more) fluophores are excited and imaged. Essentially, the emission of one fluorophore is detected in the photomultiplier channel or through the filter combination reserved for a second fluorophore. To avoid fluorescence crosstalk I used sequential imaging (see Chapter 2) and carefully selected fluophores to minimise overlap of excitation/emission spectra. The excitation and emission spectra for the fluophores I employed are shown in Figure 5.5 and indicate there should be minimal fluoresence crosstalk.

The absence of fluorescence crosstalk is evident in Figure 5.6, which shows that while cell bodies labelled with respective primary and secondary antibodies are detected in the relevant channels (left column) they do not appear in the other channels. To illustrate the selective identification of cell bodies in the appropriate channels only, I measured mean grey values from five randomly chosen cells (circular ROIs of ~7 μm diameter) and ten background ROIs within each stack (Figure 5.7). This anlaysis confirmed the absence of fluorescence crosstalk.

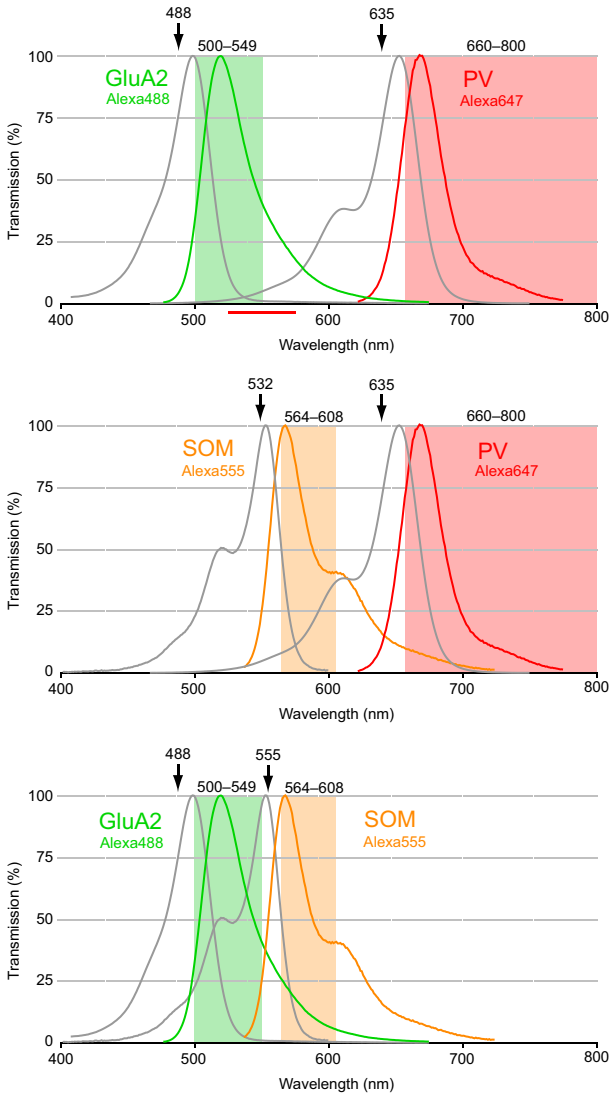

Figure 5.5: **Excitation and emission spectra for each pair of fluophores.** Graphs show excitation and emission spectra for the three fluophores used – Alexa 488, Alexa 555 and Alexa 647. To assess potential overlap, the spectra are shown as pairs: GluA2/PV, SOM/PV and GluA2/SOM. The arrows denote the wavelengths of the laser excitation lines and the coloured blocks denote wavelengths over which the emission was collected. Note that DAPI was excited with a laser line of 405 nm. Curves taken from http://www.omegafilters.com/Products/Curvomatic

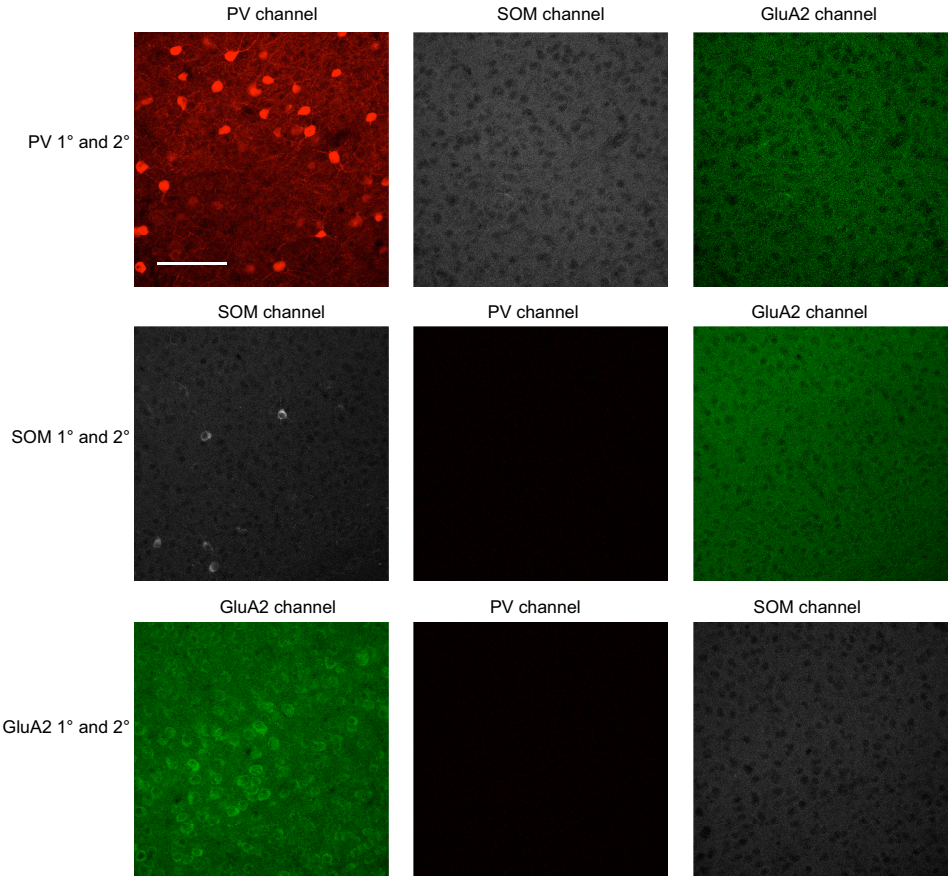

Figure 5.6: **Absence of fluorescence crosstalk.** Coronal sections of visual cortex from P21 WT mice obtained with a 20x objective. Images of single optical sections from the PV-, SOM- and GluA2 channels for slices labelled with PV primary and secondary antibodies (top row), SOM primary and secondary antibodies (middle row), and GluA2 primary and secondary antibodies (bottom row). Note the absence of bleed-through in the right-hand pair of columns. Scale bar is 100 μm.

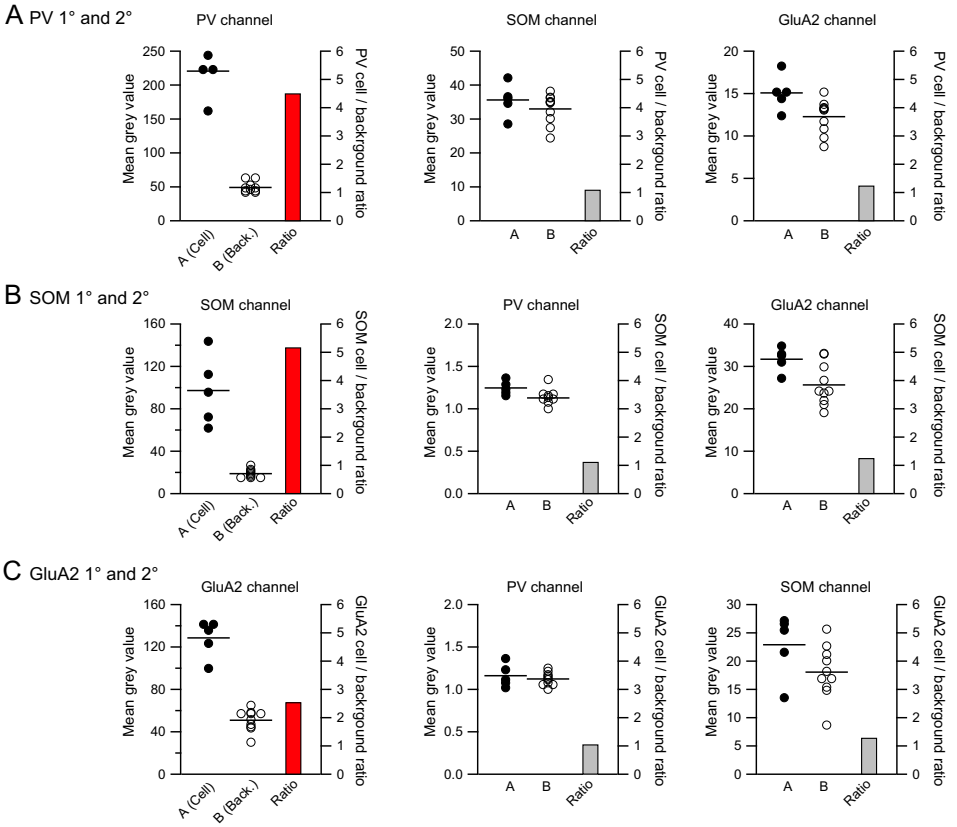

Figure 5.7: **Quantification of cell detection in appropriate channels only.** Filled circles denote mean grey values from randomly chosen cells (circular ROIs of ~7 μm diameter) and open circles denote mean grey values from randomly chosen background ROIs within each stack. For 'off-target' channels (excitation and detection wavelengths other than those appropriate for the relevant primary/secondary antibody combination) the ROIs were kept fixed at the location of the chosen cell bodies and background selections. The horizontal lines indicate the average values. The filled columns indicate the ratios of average mean grey values between the target cells and the background. (**A**) Measurements taken from slices incubated with anti-PV primary and corresponding secondary antibodies. (**B**) Measurements taken from slices incubated with anti-SOM primary and corresponding secondary antibodies. (**C**) Measurements taken from slices incubated with anti-GluA2 primary and corresponding secondary antibodies. In the appropriate channels (left column) the cell/background ratios (red fills) are 2.5 (GluA2), 4.5 (PV) and 5.2 (SOM). In the off-target channels the ratios (grey fills) are all ~1.

5.3.2 Tests of secondary antibodies

Secondary antibodies alone

To test for specificity of the secondary antibodies I applied each of them in the absence of primary antibodies. The residual staining was considered as being non-specific. For all three secondary antibodies, there was no cell labelling evident (Figure 5.8). With Alexa Fluor 555 Goat Anti-Rat IgG and Alexa Fluor 488 Goat Anti-Rabbit IgG there was some faint, largely diffuse labelling. In the case of Alexa Fluor 488 Goat Anti-Rabbit IgG (used to label the GluA2 primary) the mean grey values were less than seen in the backround of triply labelled sections (55.2 ± 4.3; see also Table 5.1).

Primary and all secondaries

Although the secondary antibodies I used are nominally selective, only one of these (the anti-guinea pig antibody used to label the PV primary) was cross-absorbed by the the manufacturer against rabbit and rat sera, the species of the other two primary antibodies used in the triple labelling. To test for cross-reactivity I incubated sections first with one primary antibody only and then with all secondary antibodies. All possible combinations were tested. As shown in Figure 5.9, when comparing GluA2 and SOM immunolabelling there was no evidence of cross-reactivity. Thus, the GluA2 secondary antibody labelled neurons in the presence of the GluA2 primary antibody and not in the presence of the SOM primary antibody alone. Conversely, the SOM secondary antibody labelled neurons in the presence of the SOM primary antibody and not in the presence of the GluA2 primary antibody alone.

However, as shown in Figure 5.10, when comparing GluA2 and PV immunolabelling there was clear evidence of cross-reactivity. Thus, the GluA2 secondary antibody labelled neurons in the presence of the GluA2 primary antibody and, unexpectedly, in the presence of the PV primary antibody alone. Conversely, the PV secondary antibody labelled neurons in the presence of the PV primary antibody but not in the presence of the GluA2 primary antibody alone. Thus, the seemingly greater expression of GluA2 in the neurons most heavily immunoreactive for PV (Figure 5.4) seems not

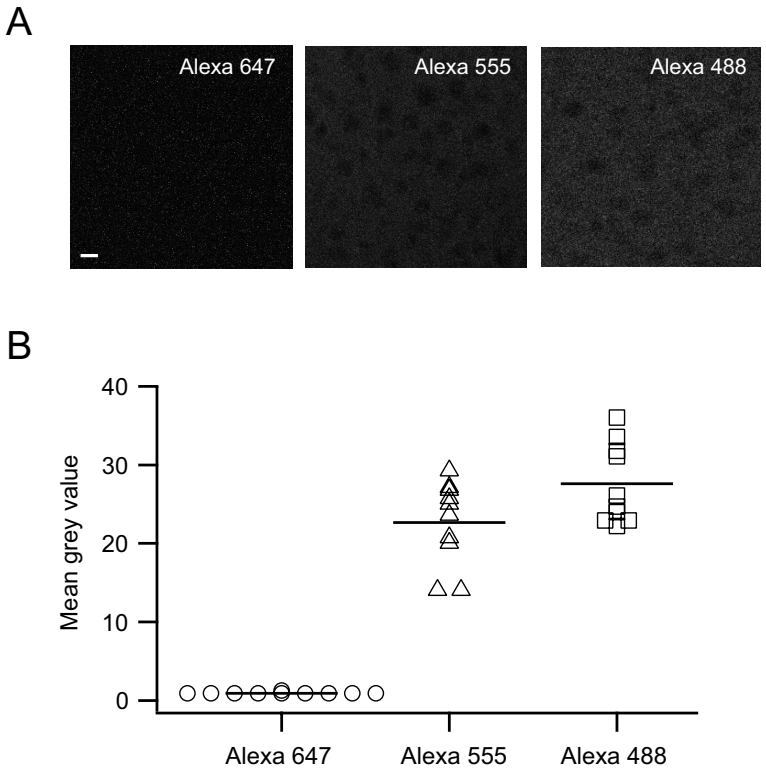

Figure 5.8: **Secondary antibodies alone.** Coronal sections of visual cortex from P21 WT mice obtained with a 20x objective. (**A**) Optical slices from L5 immunolabelled with Alexa Fluor 647 Goat Anti-Guinea Pig IgG, Alexa Fluor 555 Goat Anti-Rat IgG and Alexa Fluor 488 Goat Anti-Rabbit IgG. Scale bar 10μm. (**B**) Mean grey values determined from ten randomly chosen circular ROIs of ~3 μm diameter within each stack. Horizontal lines denote the mean values.

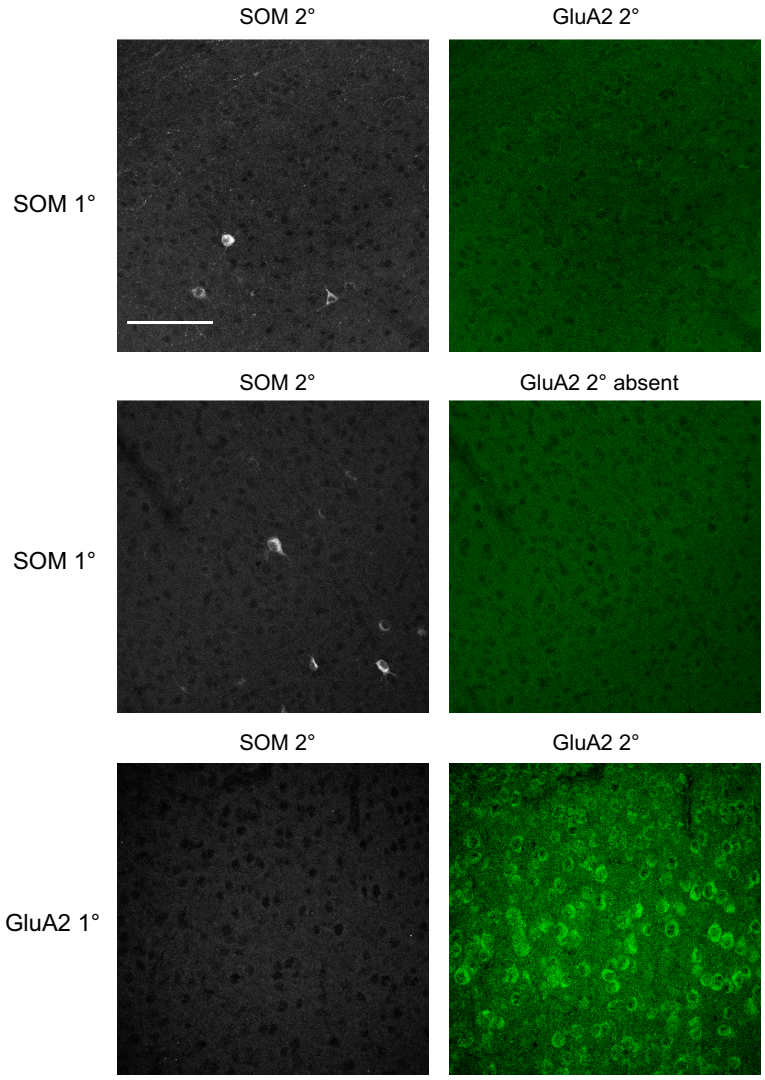

Figure 5.9: **GluA2 and SOM secondary antibody specificity.** Coronal sections of visual cortex from P21 WT mice obtained with a 20x objective. Left column shows images acquired in the SOM channel (see Figure 5.5). Right column shows images acquired in the GluA2 channel (see Figure 5.5). Upper row shows slice labelled with the anti-SOM primary antibody together with the SOM secondary antibody (left) and the GluA2 secondary antibody (right). Middle row shows slice labelled with the anti-SOM primary antibody together with the SOM secondary antibody (left) but no GluA2 secondary antibody (right). Bottom row shows slice labelled with the anti-GluA2 primary antibody together with the SOM secondary antibody (left) and the GluA2 secondary antibody (right). These results indicate no cross-reactivity of the secondary antibodies used for SOM and GluA2. Scale bar is 100 μm.

to reflect a developmental progression, but rather an unfortunate cross reaction of the goat anti-rabbit antibody with the guinea pig anti-PV primary antibody.

This apparent cross-reactivity means that my results regarding the extent of GluA2 expression in PV-positive INs cannot be interpreted. However, my data concerning GluA2 expression in SOM-positive INs are valid. I found that the somatic GluA2 content of SOM-positive INs was approximately half that of PCs (normalised ratio 0.56 ± 0.12; Table 5.1). This result was replicated in experiments involving double- rather than triple-labelling (SOM and GluA2 only), where mean ratio was 0.51 ± 0.03 (n = 3 slices).

5.4 Resolution of GluA2 expression in PV-positive INs

To address the problem with the combination of guinea-pig anti-PV and goat anti-rabbit antibodies, I tried a different set of antibodies. Specifically, I switched to a mouse anti-PV primary antibody (swant PV 235), an Alexa Fluor 488 goat anti-mouse antibody (Jackson ImmunoResearch Laboratories Inc. 115-545-062) and a Cy5 goat anti-rabbit antibody (Jackson ImmunoResearch Laboratories Inc. 111-175-144) (see Chapter 2 and Figure 5.11).

The anti-PV primary was from mouse – the same species as the tissue sections – increasing the likelihood of non-specific binding to epitopes exposed upon tissue damage or to extracellular matrix molecules (Fritschy, 2008). However, mouse anti-PV antibodies (including swant PV 235) have previously been successfully employed with mouse tissue (Gonchar et al., 2007) (Milenkovic et al., 2013). Of note, the Alexa Fluor 647 goat anti-rabbit secondary antibody was cross-absorbed by the the manufacturer against mouse sera. Nevertheless, to test for specificity of the secondary antibody I applied it in the absence of the anti-PV primary antibody. The residual staining was considered as being non-specific. Blood vessels were labelled (as expected when using a mouse antibody on mouse tissue) but there was no IN labelling evident (Figure 5.12 on page 141).

To test for cross-reactivity I also incubated sections first with one primary antibody

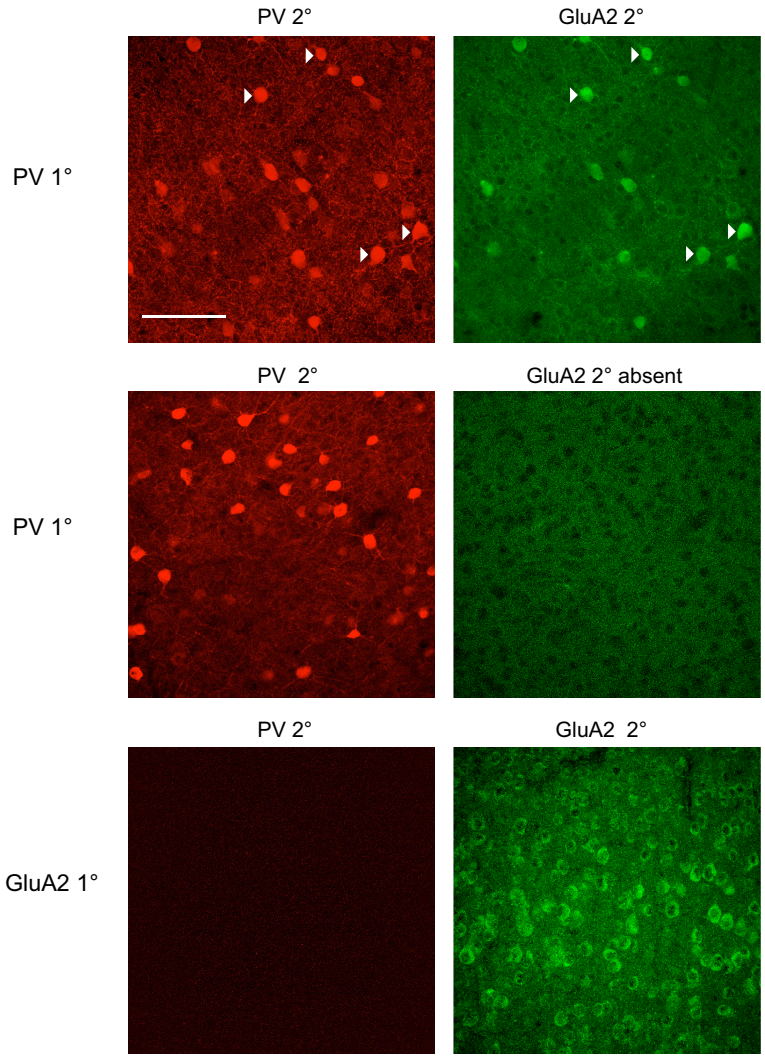

Figure 5.10: **GluA2 and PV secondary antibody specificity.** Coronal sections of visual cortex from P21 WT mice obtained with a 20x objective. Left column shows images acquired in the PV channel (see Figure 5.5). Right column shows images acquired in the GluA2 channel (see Figure 5.5). Upper row shows slice labelled with the anti-PV primary antibody together with the PV secondary antibody (left) and the GluA2 secondary antibody (right). Note the similar pattern of cell body labelling (arrowheads). Middle row shows slice labelled with the anti-PV primary antibody together with the PV secondary antibody (left) but no GluA2 secondary antibody (right). Bottom row shows slice labelled with the anti-GluA2 primary antibody together with the PV secondary antibody (left) and the GluA2 secondary antibody (right). These results indicate clear cross-reactivity of the secondary antibody used for GluA2. Scale bar is 100 μm.

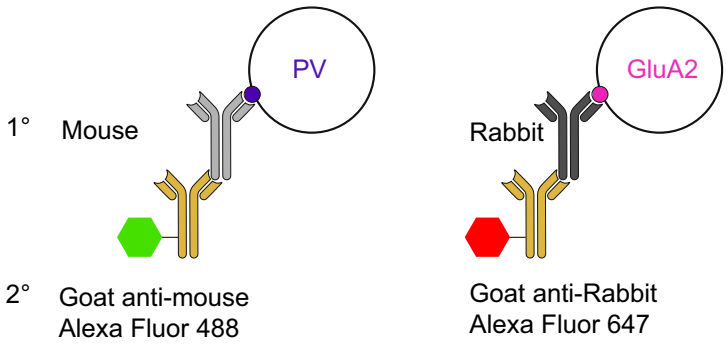

Figure 5.11: **Schematic diagram illustrating the origin (species) and selectivity of alternative primary (1°) and secondary (2°) antibodies used for double labelling of cortical sections for PV and GluA2**. See Figure 5.1 for comparison.

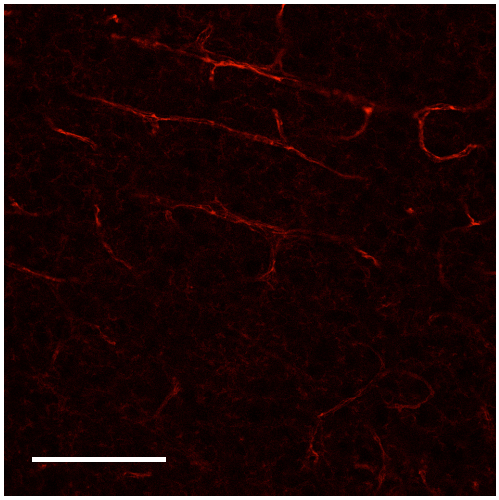

Figure 5.12: **PV secondary antibody alone.** Image of coronal section of visual cortex from P21 WT mouse obtained with a 20x objective. Image shows a single optical slice from L5 immunolabelled with Alexa Fluor 488 goat anti-mouse IgG. Scale bar 100μm. Note the non-specific labelling of blood vessels.

only and then with both secondary antibodies. Both combinations were tested. As shown in Figure 5.13, when comparing GluA2 and PV immunolabelling there was no evidence of cross-reactivity. Thus, the GluA2 secondary antibody labelled neurons in the presence of the GluA2 primary antibody and not in the presence of the PV primary antibody alone. As with the secondary antibody alone, I observed labelling of blood vessels but this did not interfere with the identification of PV-positive INs.

Double labelling for PV and GluA2 is shown together with DAPI staining in Figure 5.15 on page 145. This image shows a PV-positive IN (arrowhead) and three PV-negative PCs (asterisks). In marked contrast to the labelling shown in Figure 5.3 on page 127 only the PCs and not the PV-positive IN are immunoreactive for GluA2.

Unlike what was seen with the previous antibody combinations, there was no indication of the brightest GluA2 immunofluorescence coming from cells most strongly labelled for PV. This was clear from visual inspection of images and from plots relating the grey scale intensity of PV and GluA2 immunoreactivity (Figure 5.14). Thus, when multiple cells were examined in single slices, a uniformly low level of GluA2 labelling was seen irrespective of the intensity of PV labelling and there was no positive correlation between the two measures ($R_S < 0.2$ and $p > 0.6$).

As shown in Table 5.2, with the new antibody combination, while the PC labelling for GluA2 was comparable to that seen previously, the labelling of PV-positive INs was much less pronounced. When normalised to the mean grey value from PCs, the GluA2 labelling of the PV-positive INs was only ~11% of that seen with the previous antibody combination. Combining the earlier data for SOM-positive INs with the new data for PV-positive INs leads to the conclusion that the somatic GluA2 labelling follows the order PC (1) > SOM (0.56) > PV (0.14). Thus, the PV-positive INs show only one quater of the somatic GluA2 labelling of SOM-positive INs. These results are more in line with our electrophysiological observations (Lalanne et al., 2014) and strongly reinforce the necessity of carrying out appropriate control experiments when using antibodies.

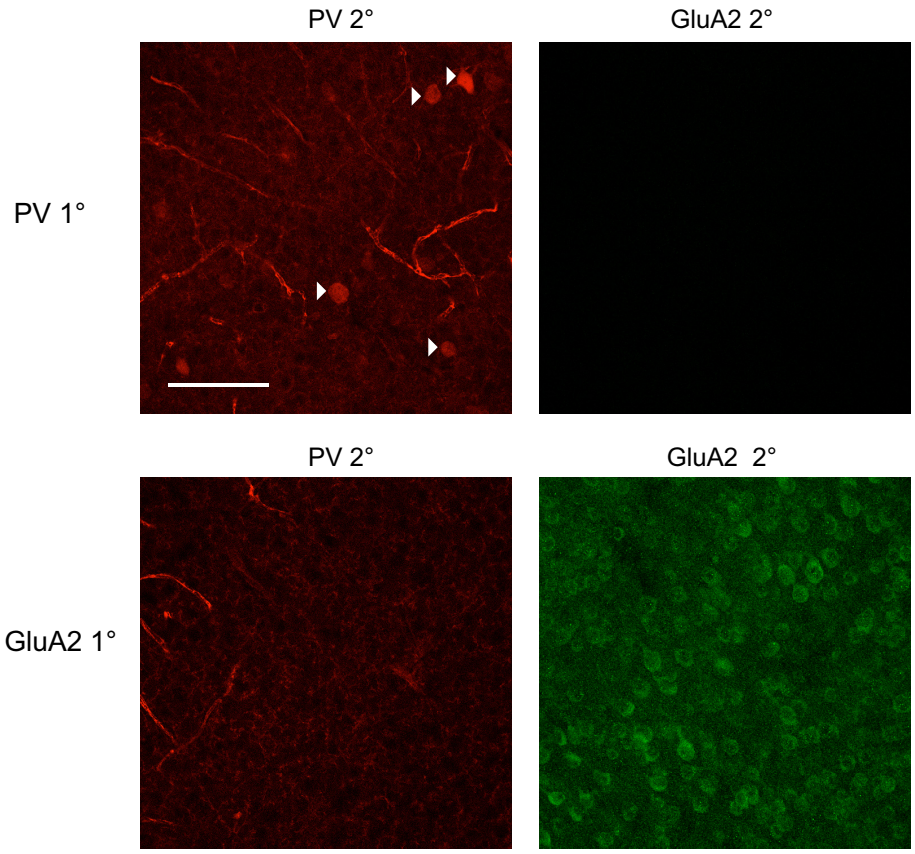

Figure 5.13: **Specificity of new GluA2 and PV secondary antibodies.** Coronal sections of visual cortex from P21 WT mice obtained with a 20x objective. Left column shows images acquired in the PV channel. Right column shows images acquired in the GluA2 channel. Upper row shows slice labelled with the mouse anti-PV primary antibody (swant PV 235) together with the PV secondary antibody (goat anti-mouse, left) and the GluA2 secondary antibody (goat anti-rabbit, right) (see Figure 5.11). In the top row, note the PV-positive cell body labelling (arrowheads) and the lack of labelling in the presence of the GluA2 secondary. Bottom row shows slice labelled with the anti-GluA2 primary antibody together with the PV secondary antibody (left) and the GluA2 secondary antibody (right). These results indicate a clear lack of cross-reactivity of the secondary antibody used for GluA2. In the left columns, in presence of the mouse PV secondary antibody, blood vessels are detected. Note, the pseudo-colour coding has been chosen for consistency with previous figures. For illustration purposes only, the brightness was slightly increased for all images. Scale bar is 100 μm.

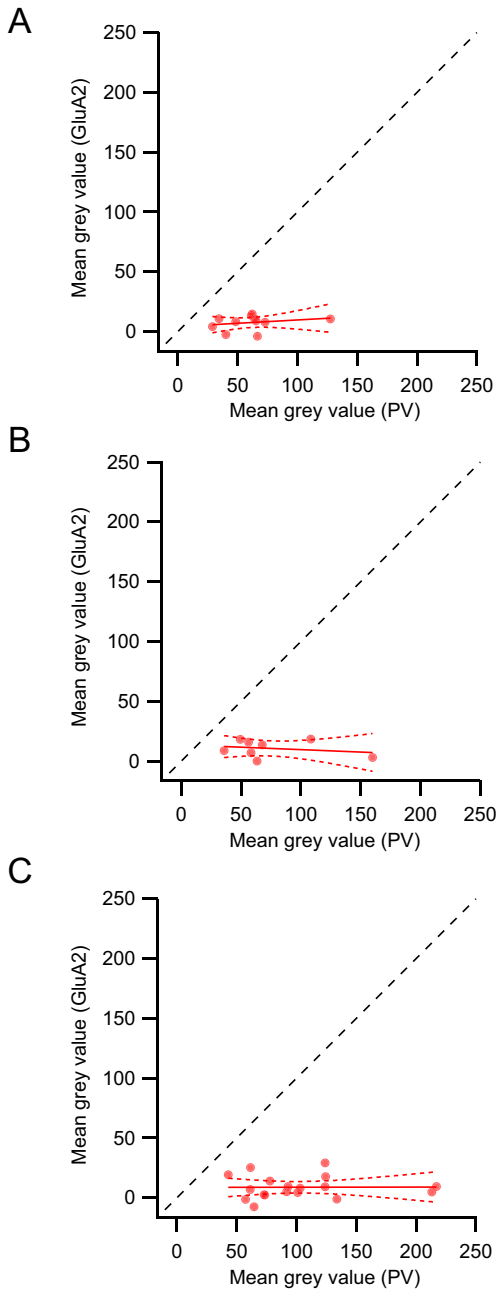

Figure 5.14: **Scatterplots illustrating the lack of relationship between GluA2 and PV somatic labelling seen with the alternative antibody combination**. The three plots (A, B and C) are from single slices from one P21 WT mouse. Symbols denote background subtracted grey values. Solid lines (red) are linear fits and curved dashed lines (red) indicate the 95% confidence interval of the fit. The straight dashed lines (black) are lines of identity. In each case the significance of the relationship was tested using a Spearman rank order correlation test. (**A**) $n = 11$, $R_S = 0.02$, $p = 0.97$. (**B**) $n = 8$, $R_S = -0.17$, $p = 0.70$ (**C**) $n = 18$, $R_S = 0.12$, $p = 0.64$.

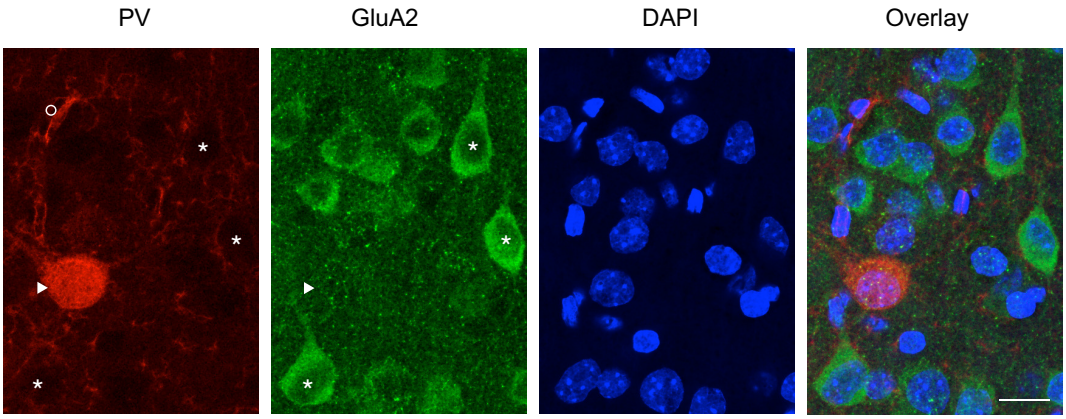

Figure 5.15: **Images of a coronal section of visual cortex from a P21 WT mouse obtained with a 40x objective**. Selected region of a maximum intensity projection (10 optical sections only) from L5 (stained with DAPI and immunolabelled with the alternative antibodies against PV and GluA2). The final image is an overlay of the previous three. The arowhead indicates a PV-positive IN. The asterisks mark the cell bodies of PV-negative, GluA2-positive PCs surrounded by PV-positive axons/puncta (less clear than with previous PV antibody; Figure 5.3 on page 127). The open circle indicates a blood vessel. Note, the pseudocolour coding has been chosen for consistency with previous figures. For illustration purposes only, the brightness was slightly increased for all images. Scale bar 15 μm.

	Mean grey value		Normalised to PC
	PC	PV	PV
Slice 1	74.3	10.7	0.14
Slice 2	57.4	7.7	0.13
Slice 3	61.9	8.8	0.14
Global average	64.5	9.1	0.14
SEM	5.0	0.9	0.003

Table 5.2: **GluA2 immunolabelling of PV interneurons identfied with mouse anti-PV primary antibody**. Values shown are the average measurements from three slices from a single animal, in which mean grey values were determined from a single optical section with circular ROIs of ~3 μm diameter located on the soma. The ROI was centred on the brightest region of PV labelling and the GluA2 intensity was taken from the same position. As before, the GluA2 labelling in PCs was used to normalise the GluA2 intensity accross slices. Here, GluA2 labelling was taken from the brightest region of the soma. Note, all measurements are background subtracted (average of at least 20 ROIs per stack).

5.5 Discussion

My experiments suggest the presence of contrasting GluA2 expression patterns in the two major IN subclasses of layer 5, characterized by the expression of PV or SOM. While the soma of PV-positive INs contained hardly any GluA2 immunoreactivity, the soma of SOM-positive INs were strongly labelled, but less so than PCs. This observation supports my own electrophysiological data (see Chapter 4) and that of my collaborators (Lalanne et al., 2014), which showed rectifying current-voltage relationships for AMPAR-mediated currents in BCs but not in MCs. Thus, my immunolabelling results, taken together with the electrophysiological results, are suggestive of the presence of CP-AMPARs in BCs but not in MCs. My immunolabelling results regarding SOM-positive INs were obtained from multiple triple- as well as double-labelling experiments using three different P21 animals. They can, therefore, been viewed as providing a robust conclusion regarding the level of GluA2 expression in these cells. By contrast, because of the initial difficulties with antibody cross-reactivity, my final conclusions regarding PV-positive INs come from only one animal and thus require additional verification. Nevertheless, together my immunolabelling data strongly suggest differences in GluA2 expression by PV- and SOM-positive INs.

Cell identification

For the correct interpretation of my data it is important to appreciate to what extent one can equate PV- and SOM-positive INs with BCs and MCs, respectively. As described in earlier chapters, many attempts have been made to link molecular expression with anatomical and electrophysiological features of INs. SOM is expressed in all MCs (Toledo-Rodriguez et al., 2005; Wang et al., 2004); this is true for assays of protein or mRNA and regardless of the anatomical and electrophysiological differences accross different layers and cortical regions (Wang et al., 2004; Kawaguchi and Kubota, 1996, 1998; Wahle, 1993; Toledo-Rodriguez et al., 2005). However, MCs are not the only IN subtypes that contain SOM (Ma et al., 2006; McGarry et al., 2010; Wang et al., 2004; Kawaguchi and Kubota, 1996). For example, SOM has been shown to be present occassionally in NBCs as well as small BCs (Wang et al., 2002). Additionally, certain

SOM-positive INs in the X94 line of transgenic mice (which like the GIN line have GFP expressed under the control of the GAD67 promoter) are thought to constitute a morphological subtype with quasi-fast-spiking properties (Ma et al., 2006). Similarly, more recent studies of the GIN line have also identified SOM-positive neurons with atypical non-MC morphological features (McGarry et al., 2010). Despite this, SOM is currently considered one of the most useful of the available molecular markers for INs (Toledo-Rodriguez et al., 2005), with relatively high specificity for MCs (Markram et al., 2004; McGarry et al., 2010; Toledo-Rodriguez et al., 2005).

After SOM, PV is considered the next most useful of the available molecular markers (Toledo-Rodriguez et al., 2005), being primarily associated with cells that display fast-spiking behaviour and anatomical features of BCs (Cauli et al., 1997; Dumitriu et al., 2007; Kawaguchi and Kubota, 1997; Woodruff et al., 2009). Although the much less numerous ChCs have long been thought to contain PV, a recent study suggests that this is true for only a varying subset of these cells – depending on cortical region (Taniguchi et al., 2013). Importantly, PV is not expressed in all BCs. On the basis of their morphological features, BCs have been classified into sub-groups: large-, nest- and small-BCs (LBC, NBC and SBCs) (Markram et al., 2004). LBCs and NBCs express PV but it is rarely found in SBCs (Wang et al., 2002; Toledo-Rodriguez et al., 2005). Overall, PV is considered a reliable marker for BCs (Ascoli, 2008; Markram et al., 2004; Toledo-Rodriguez et al., 2005; Woodruff et al., 2009).

Although PV and SOM are likely to identify predominantly BCs and MCs it is important to note that, as alluded to above, these cell types are not necessarily homogeneous. LBCs, NBCs and SBCs also differ in the expression of other molecular markers, with SBCs, but not LBCs or NBCs, expressing VIP. Conversely, LBCs and NBCs, but not SBCs, occasionally express CCK and all three subtypes occassionaly also express CB (Wang et al., 2002).

While a substantial number of SOM-positive MCs (more than 50%) express only this marker, the remaining cells (dependent to some extent on the cortical layer in which they are found) have been shown to also express CB, CR, NPY or CCK (Wang et al., 2002). Further variability within the SOM-positive MCs is suggested by the study of Ma et al. (2006), which introduced an additional potential subtype defined by the

coepxression of CB and NPY. Additionally, two classes of SOM-positive MCs have been suggested to occur in the mouse visual cortex, defined by the coexpression (or not) of CR (Xu et al., 2006). Even though these additional subdivisions could reflect functional heterogeneity among BCs and MCs, currently there is no real agreement on this point. Regarding putative molecular markers, while it is true that some markers are expressed only by certain IN types, no one marker unambiguously indentifies only a single anatomically or electrophysiologically defined IN type.

The use of neurochemical markers as a tool to distinguish different cell types has additional difficulty in that molecular expression need not be uniform across cortical layers or species. For example, SOM-positive cells have been described as showing differences in marker colocalization across layers in the somatosensory cortex of juvenile rats (Wang et al., 2004). In the rat cortex SOM, PV and CR have been shown to be distinct, non-overlapping molecular markers (Gonchar and Burkhalter, 1997; Kawaguchi and Kubota, 1997), By contrast, in the mouse CR is found together with SOM (Xu et al., 2006, 2010). Nevertheless, the current consensus, as set out in the molecular classification of the Petilla terminology1 (DeFelipe et al., 2013), is that cortical INs can be classified by their expression of specific molecular markers into five main groups of interneurons, defined by their expression of 1) PV (including ChCs and BCs), 2) SOM (MCs), 3) NPY but not SOM, 4) VIP, and 5) CCK but not SOM or VIP. Further, more refined, molecular classification is possible on the basis of expression profiles of transcription factors, enzymes, neurotransmitter receptors, structural proteins and ion channels, for example, and such profiling is likely to become more common in future work (DeFelipe et al., 2013; Toledo-Rodriguez et al., 2005).

Comparison with other studies

My findings differ from those reported for the rat somatosensory cortex, where the majority of PV-positive INs have been shown to be immunoreactive for GluA2 (Vissavajjhala et al., 1996). However, the same group subsequently found a subset of PV-positive INs in neocortex that lacked GluA2 labelling but had high immunoreactivy for GluA3 (Moga et al., 2002). While this might be seen as showing partial agreement with my results, it is of note that I found a relatively homogeneous (low) GluA2

labelling in PV-positive INs (see Figure 5.14). The discrepancies between our studies could result from technical differences or they could reflect differences in species, animal age, cortical area or cortical layer examined. Perhaps given this apparent difference between mice and rats, it is not surprising that my results are also strikingly different from those reported by Kooijmans et al. (2014) regarding the visual cortex of the monkey. These authors showed that the cell bodies of PV-positive INs were strongly immunolabelled for both GluA2 and GluA3, while SOM-positive INs (identified, in this case, by their expression of CB (Condé et al., 1994)) showed little or no labelling for GluA2 (Kooijmans et al., 2014). This is the exact opposite of my findings in the mouse. When comparing data from mouse and monkey, a distinction between species is perhaps to be expected as the IN classes are themselves defined by different molecular markers (Condé et al., 1994; Gonchar et al., 2007; Xu et al., 2010; Wahle, 1993). This could suggest genuine differences in CP-AMPAR expression, and thus IN function, accross species (see Chapter 6).

Alternative approaches and future studies

Due to restrictions imposed by excitation/emission wavelength considerations (the need to avoid overlap of emission spectra) and species limitations (secondary antibodies have to come from distinct species), only a limited number of proteins at a time can be detected with immunolabelling studies. However, as elaborated above, examining the expression of multiple genes is suggested to distinguish neuronal types better than the immunolabelling for one or two neurochemical markers. *In situ* hybridization combined with immunocytochemistry would provide an alternative approach (Cox and Racca, 2013; Keinänen et al., 1990; Petralia and Wenthold, 1992; Tölle et al., 1993). Combining single-cell RT-PCR (or RT multiplex PCR; RT-mPCR) (Rossi et al., 2008; Cauli et al., 1997) with electrophysiological and morphological analysis (Blatow et al., 2005; Toledo-Rodriguez et al., 2004) would also be an approach worth considering. This would address *a*) the issue of assaying only a limited number of markers by immunofluorescence, *b*) allow the examination of multiple GluA subunits, and *c*) overcome a major drawback of my labelling study, the separation of the labelling from any anlaysis of function or morphology.

Another major drawback to the approach I employed is that I was only able to examine somatic immunolabelling. Clearly, what is of most relevance is the synaptic expression of GluA subunits. When a gene is not expressed at all, then somatic labelling is informative, otherwise different aproaches to answer my question would perhaps have been better, if somewhat more demanding. Although potentially difficult in tissue sections, it may be possible to use light microscopic imaging of immunolabelled receptors in combination with labelling of recognised synaptic markers such as postsynaptic density protein 95 (PSD95) or the postsynaptic scaffolding protein homer1c. Potentially, similar approaches could be used together with super-resolution imaging techniques such as direct stochastic optical reconstruction microscopy (dSTORM), PALM or STED (Nair et al., 2013; Dani et al., 2010). Finally, postembedding electron microscopy (EM), immunogold labelling EM or freeze-fracture EM (Nusser et al., 1998; Petralia and Wenthold, 1992; Amiry-Moghaddam and Ottersen, 2013; Takumi et al., 1999; Tarusawa et al., 2009) could be used to definitively locate receptor subunits to synapses. However, in this case, correctly identifying the postsynaptic cell type would be problematic.

Chapter 6

Discussion

The results described in the preceding chapters – my own together with those of my collaborators – indicate that CP-AMPARs are found at excitatory synapses onto BCs, while CP-AMPARs appear to be absent from excitatory synapses onto MCs (Oyrer et al., 2013; Lalanne et al., 2014).

As discussed in Chapter 4, my findings in the visual cortex are in broad agreement with various functional studies that have identified the presence of CP-AMPARs in BCs of various brain regions, including the hippocampus, the prefrontal cortex and the barrel cortex. My functional data are also supported by the results of my immunolabelling studies (Chapter 5), which show stronger somatic GluA2 expression in SOM- versus PV-positive INs.

Potential functional implications

What might the significance be of having different IN classes recruited by inputs acting via AMPARs with different functional properties? To understand this it is necessary to appreciate the behaviour and targetting of BCs and MCs. As described in Chapter 1, while both BCs and MCs provide feed-forward and feed-back inhibition, they target different compartments of the PCs (BCs perisomatic locations and MCs distal dendrites). Also, excitatory inputs to BCs exhibit short-term depression while those to

MCs show short-term facilitation, giving rise to the so-called FIDI and FDDI microcircuits, respectively (Silberberg and Markram, 2007).

To provide insight into the contribution of differential CP-AMPAR expression to microcircuit function, my collaborator Rui Costa (Oxford) used a phenomenological local cortical network model (Buchanan et al., 2012). Specifically, he adjusted the parameters of equations describing short-term synaptic plasticity (Tsodyks and Markram, 1997; Markram et al., 1998) to replicate the effects of Naspm seen in paired recordings performed by Txomin Lalanne. As shown in in Figure 6.1, modelling of BC and MC feed-forward inhibition of a PC suggested that CP-AMPARs support early- (FIDI pathway) but not late inhibition (FDDI pathway). This result is complimentary to that which emerged from our study of presynaptic NMDARs in L5 (Buchanan et al., 2012); this suggested that late inhibition mediated by MCs (FDDI pathway) is facilitated by the selective presence of preynaptic NMDARs at PC synapses onto MCs but not BCs.

The phenomenological model, while illustrating the role of AMPARs in BCs, does not address features that might be dependent on the specific nature of the AMPARs (CP or CI). In relation to short-term plasticity, the presence of CP-AMPARs in BCs could endow them with a form of short-term facilitation that would tend to counteract the presynaptically determined short-term depression. This is because CP-AMPARs are influenced by endogenous intracellular polyamines that produce a voltage-insensitive closed-channel block that is relieved by cation influx; this results in an activity-dependent postsynaptic facilitation (or more generally a reduced depression) at physiologically relevant frequencies of activation (Bowie et al., 1998; Rozov et al., 1998; Rozov and Burnashev, 1999). Such polyamine-dependent short-term plasticity has been observed in FS basket-like INs in the prefrontal cortex (Wang and Gao, 2010). This phenomenological model is very similar to that proposed by Pouille and Scanziani (2004) for somatic and dendritic targeting hippocampal interneurons. These authors similarly concluded that somatic targeting INs, whose excitatory drive exhibited short-term depression ('onset-transient' INs), produced early onset inhibition of target PCs and that during a series of action potentials this inhibition rapidly shifts to that mediated by dendrite targeting INs ('late persistent' INs), whose excitatory input displayed short-term facilitation. Importantly, it should be noted that the model shown in Figure 6.1

is very simplistic; future work would need to address additional features, notably the presence of BC-MC inhibitory connections (reviewed in Lovett-Barron and Losonczy, 2014) and autapses (Deleuze et al., 2014).

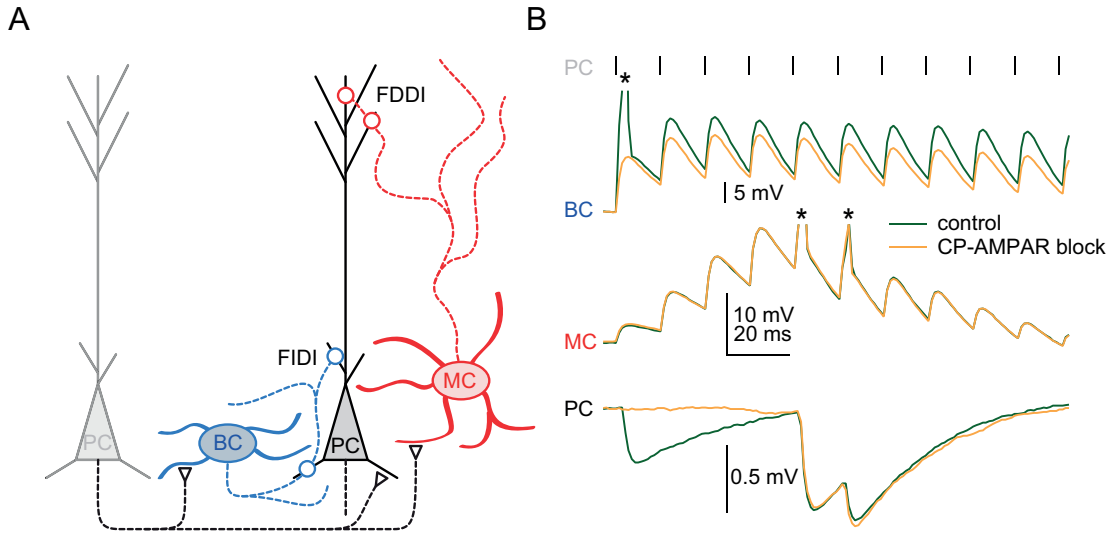

Figure 6.1: **A phenomenological model of the cannonical L5 cortical micro-circuit illustrating the projected effect of CP-AMPAR blockade.** (**A**) A schematic representing FIDI and FDDI micro-circuits formed from two PCs (grey), a BC (blue) and an MC (red). Triangles denote the excitatory connections from the first PC onto the INs, while circles denote the inhibitory connections provided by the INs to the second PC. (**B**) Results of a phenomenological model based on vesicle depletion (Tsodyks and Markram, 1997; Markram et al., 1998). The model was implemented in Matlab using integrate-and-fire neurons and paramaters adapted from Buchanan et al. (2012). A train of action potentials in the first PC (black vertical lines; 70 Hz) elicits depressing EPSPs in the BC (green trace) and but facilitating EPSPs in the MC (green trace). Asterisks denote triggered action potentials. The effect of Naspm is shown by the orange traces. Note, while Naspm application has a clear effect on the BC response train, the MC response is not affected. The IPSPs in the second PC show that Naspm blocks early- but not late inhibition.

A very recent study by Lu et al. (2014) also reported the presence of CP-AMPARs at local- but not at long-range inputs to PV-positive INs in mouse visual cortex (in this case L2/3). Interestingly, they observed a selective developmental decrease in short-term depression of these local inputs which correlated with a developmentally increased ratio of CP- to CI-AMPARs. Perhaps the most intriguing aspect of this study – echoing the findings of Tóth and McBain (1998) in the hippocampus – is the suggestion that different inputs to a single PV cell can activate different subtypes of AMPARs. This provides a plausible basis for my suggestion that BC mEPSCs may be heterogeneous, given the different estimates of RI obtained using different approaches (count-matching versus summmed mEPSC charge).

Long-term plasticity of excitatory inputs to GABAergic INs is heterogeneous. As discussed in Chapter 1, CP-AMPARs underlie the induction of NMDAR-independent anti-Hebbian LTP at excitatory inputs onto INs in the hippocampus (Lamsa et al., 2007; Oren et al., 2009; Szabo et al., 2012). In the cortex, having CP-AMPARs differentially expressed among distinct IN types (BCs and MCs) suggests that different rules of plasticity induction exist for these cells. Thus, it might be expected that PC-BC synapses would show non-Hebbian forms of plasticity while PC-MC synapses would show NMDAR-dependent Hebbian plasticity. If this were indeed the case, specific patterns of pre- and postsynaptic firing (as seen in different brain states) could evoke plasticity selectively in BCs or MCs. As MCs are involved in rate-dependent feedback inhibition (targetting apical and tuft dendrites of PCs to influence dendritic integration) while BCs provide an an immediate early inbitory input to perisomatic sites (and are critically implicated in the generation of gamma oscillations; Cardin et al. 2009; Traub et al. 1996, 1997), differential plasticity of their excitatory inputs could have important repercussions for the dynamics of the cortical network (Lamsa et al., 2010).

Open questions

Are the results I have described specific to a given develomental stage? All of my experiments, and those of my collaborators, were carried out using tissue from mice aged from P14-P21. In many cell types, the expression of CP-AMPARs (as judged by

immunolabelling, functional and/or pharmacological studies) has been found to vary with development. Unfortunately no clear stereotypical pattern emerges, with different cell types and different brain regions exhibiting different developmental profiles. Thus, although many studies have suggested developmental decreases in CP-AMPAR expression (Kumar et al., 2002; Osswald et al., 2007; Shin et al., 2005; Soto et al., 2007) others have shown fluctuating expression with age (Wang and Gao, 2010), while, most relevant to my work, CP-AMPAR expression in PV-positive L2/3 INs of mouse visual cortex has recently been show to be increased at P31-P34 compared to P17-19 (Lu et al., 2014). Clearly, further studies are required to resolve this issue.

Are my results specific to the mouse? As discussed in Chapter 5, immunolabelling studies would suggest that there may well be species differences in the pattern of GluA2 expression in cortical INs. Notably, the study by Kooijmans et al. (2014), reporting PV-positive INs strongly immunolabelled for GluA2 in the primate visual cortex, differs from my own findings and implies that PV-positive INs are excited through different AMPARs. It also suggests that the organization of inhibition in mice may not be a general principle that applies to primates.

What are the molecular details governing CP-AMPAR expression? My examination of GluA2 immunolabelling was restricted to the soma. As discussed in Chapter 5, it wouId would be of interest to examine this in greater spatial detail and determine synaptic expression patterns. Given the likely heterogeneity of synapse type discussed above, it would clearly be desirable to link this with a study of the distribution of other AMPAR subunits and their regulatory proteins. The subcellular targetting of different AMPAR subtypes is known to be influenced by the presence auxiliary subunits (Bats et al., 2012; Studniarczyk et al., 2013) which likely differ between IN types. Thus, it would be interesting to establish exactly which auxiliary subunit proteins are expressed in BCs and MCs. As discussed in Chapter 4, a recent study by Tao et al. (2013) showed that among γ-2–expressing cortical INs, ~60% were PV-positive, whereas ~30% were SOM-positive. Moreover, these authors found that erbin, an adaptor protein that interacts with γ-2 to regulate AMPAR surface expression, is selectively expressed in PV-positive INs.

How do my results relate to what is known about different routes of Ca^{2+} entry

into – and Ca^{2+} buffering capability of – different INs? Ca^{2+} influx can occur via NMDARs, CP-AMPARs or voltage-gated calcium channels (VGCCs). Synapses on INs that contain CP-AMPARs tend to express few NMDARs and exhibit EPSCs with small NMDAR-mediated components, while those on INs with non-rectifying EPSCs mediated by CI-AMPARs tend to exhibit substantial NMDAR-mediated currents (Angulo et al., 1999; Hull et al., 2009; Lamsa et al., 2007; Lei and McBain, 2002; Matta et al., 2013; Wang and Gao, 2010; Scheuss and Bonhoeffer, 2014). Although one might imagine that the differential prevalence of NMDARs and CP-AMPARs simply endows different cells with alternative routes of Ca^{2+} entry, it may not be as simple as this. For example, in supragranular FS PV-positive INs of the mouse Ca^{2+} may enter via both routes, with CP-AMPARs giving rise to a fast Ca^{2+} influx and causing depolarization that facilitates an additional, slower Ca^{2+} influx following NMDAR activation (Goldberg et al., 2003c). Of note, Goldberg et al. (2004) found that synaptically driven Ca^{2+} elevations in MCs in the visual and somatosensory cortex of mice – which, as our results suggest have few or no CP-AMPARs, might be expected to rely on NMDARs – were dependent on AMPAR-mediated depolarization and activation of T-type Ca^{2+} channels and did not result from activation of NMDARs. It is also interesting to note that MCs have dendritic spines that are long and occur at ~7-fold higher density than in BCs (Kawaguchi et al., 2006). Electrical attenuation of EPSPs as they spread to the parent dendrite could mean that EPSPs in the spines themselves are very large, activating VGCCs in the spine head (Spruston and Johnston, 2008; Spruston, 2008). However, the precise role of dendritic spines in MCs is unknown. It is possible that they provide electrical or biochemical compartmentalisation that is lacking, or of different origin, in aspiny INs. The presence of spines in MCs could be related to the existence of different excitatory inputs. However, there is little available information for L5 in this regard. Both MCs and BCs in L5 receive input from local PCs, but the extent of additional innervation is unclear. Of note, in L4 there is evidence for thalamo-cortical input to BCs and not to MCs (Cruikshank et al., 2007). While there is thalamo-cortical input to L5 PCs (Petreanu et al., 2009; Constantinople and Bruno, 2013), I am unaware of any study describing the differential innervation of INs in this layer. Finally, spines in MCs may allow specific morphological changes in response to activity or during LTP that reflect or mediate the specific form of plasticity induced

(Lisman and Harris, 1993). Interestingly it is known that the presence of different AMPAR subunit types or splice isoforms can have different effects on dendrite and spine growth (Hamad et al., 2011). Unlike MCs, BCs express the (slow) Ca^{2+} binding protein PV (Hof et al., 1999) which contributes to their high endogenous buffer capacity (Aponte et al., 2008; Goldberg et al., 2003a; Lee et al., 2000). In these cells that lack spines, this buffering is thought to play a role in the effective compartmentalisation of dendritic Ca^{2+} signals (particularly during trains of synaptic activation) (Goldberg et al., 2003a) but to minimally affect local fast Ca^{2+} transients triggered by synaptic CP-AMPARs (Aponte et al., 2008). Additionally, in PV-positive FS INs (unlike in MCs) action potential backpropagation is spatially controlled by 1a-type potassium channels (Goldberg et al., 2003b). Overall, BCs and MCs show very different spatio-temporal Ca^{2+} dynamics that must be considered when addressing the likely role of CP-AMPARs in the cortical microcircuit.

Bibliography

Abbott, L. and Regehr, W. G. (2004). Synaptic computation. Nature *431*, 796–803.

Adesnik, H. and Nicoll, R. A. (2007). Conservation of glutamate receptor 2-containing AMPA receptors during long-term potentiation. Journal of Neuroscience *27*, 4598–4602.

Ady, V., Perroy, J., Tricoire, L., Piochon, C., Dadak, S., Chen, X., Dusart, I., Fagni, L., Lambolez, B. and Levenes, C. (2014). Type 1 metabotropic glutamate receptors (mGlu1) trigger the gating of GluD2 delta glutamate receptors. EMBO Reports *15*, 103–109.

Aghajanian, G. K. and Rasmussen, K. (1989). Intracellular studies in the facial nucleus illustrating a simple new method for obtaining viable motoneurons in adult rat brain slices. Synapse *3*, 331–338.

Amiry-Moghaddam, M. and Ottersen, O. P. (2013). Immunogold cytochemistry in neuroscience. Nature Neuroscience *16*, 798–804.

Angulo, M. C., Lambolez, B., Audinat, E., Hestrin, S. and Rossier, J. (1997). Subunit composition, kinetic, and permeation properties of AMPA receptors in single neocortical nonpyramidal cells. Journal of Neuroscience *17*, 6685–6696.

Angulo, M. C., Rossier, J. and Audinat, E. (1999). Postsynaptic glutamate receptors and integrative properties of fast-spiking interneurons in the rat neocortex. Journal of Neurophysiology *82*, 1295–1302.

Antonucci, F., Alpár, A., Kacza, J., Caleo, M., Verderio, C., Giani, A., Martens, H., Chaudhry, F. A., Allegra, M., Grosche, J. et al. (2012). Cracking down on inhibition:

selective removal of GABAergic interneurons from hippocampal networks. The Journal of Neuroscience *32*, 1989–2001.

Aponte, Y., Bischofberger, J. and Jonas, P. (2008). Efficient Ca^{2+} buffering in fast-spiking basket cells of rat hippocampus. Journal of Physiology *586*, 2061–2075.

Ascher, P. and Nowak, L. (1988). The role of divalent cations in the N-methyl-D-aspartate responses of mouse central neurones in culture. Journal of Physiology *399*, 247–266.

Ascoli, G. A. (2008). Petilla terminology: nomenclature of features of GABAergic interneurons of the cerebral cortex. Nature Reviews Neuroscience *9*, 557–568.

Atallah, B. V., Bruns, W., Carandini, M. and Scanziani, M. (2012). Parvalbumin-expressing interneurons linearly transform cortical responses to visual stimuli. Neuron *73*, 159–170.

Atasoy, D., Ertunc, M., Moulder, K. L., Blackwell, J., Chung, C., Su, J. and Kavalali, E. T. (2008). Spontaneous and evoked glutamate release activates two populations of NMDA receptors with limited overlap. Journal of Neuroscience *28*, 10151–10166.

Ayalon, G. and Stern-Bach, Y. (2001). Functional assembly of AMPA and kainate receptors is mediated by several discrete protein-protein interactions. Neuron *31*, 103–113.

Barberis, A., Petrini, E. M. and Mozrzymas, J. W. (2011). Impact of synaptic neurotransmitter concentration time course on the kinetics and pharmacological modulation of inhibitory synaptic currents. Frontiers in Cellular Neuroscience *5*, 6.

Barbour, B. (2011). Electronics for electrophysiologists. http://www.biologie.ens.fr-/ barbour/.

Barbour, B. and Häusser, M. (1997). Intersynaptic diffusion of neurotransmitter. Trends in Neurosciences *20*, 377–384.

Barry, P. H. (1994). JPCalc, a software package for calculating liquid junction potential corrections in patch-clamp, intracellular, epithelial and bilayer measurements and

for correcting junction potential measurements. Journal of Neuroscience Methods *51*, 107–116.

Barry, P. H. and Lynch, J. W. (1991). Liquid junction potentials and small cell effects in patch-clamp analysis. Journal of Membrane Biology *121*, 101–117.

Bats, C., Soto, D., Studniarczyk, D., Farrant, M. and Cull-Candy, S. G. (2012). Channel properties reveal differential expression of TARPed and TARPless AMPARs in stargazer neurons. Nature Neuroscience *15*, 853–861.

Bekkers, J. M. and Clements, J. D. (1999). Quantal amplitude and quantal variance of strontium-induced asynchronous EPSCs in rat dentate granule neurons. Journal of Physiology *516*, 227–248.

Bekkers, J. M. and Stevens, C. F. (1996). Cable properties of cultured hippocampal neurons determined from sucrose-evoked miniature EPSCs. Journal of Neurophysiology *75*, 1250–1255.

Benke, T. A., Lüthi, A., Isaac, J. T. and Collingridge, G. L. (1998). Modulation of AMPA receptor unitary conductance by synaptic activity. Nature *393*, 793–797.

Bennett, M. R. (1999). The early history of the synapse: from Plato to Sherrington. Brain Research Bulletin *50*, 95–118.

Berger, T. K., Perin, R., Silberberg, G. and Markram, H. (2009). Frequency-dependent disynaptic inhibition in the pyramidal network: a ubiquitous pathway in the developing rat neocortex. Journal of Physiology *587*, 5411–5425.

Betzig, E., Patterson, G. H., Sougrat, R., Lindwasser, O. W., Olenych, S., Bonifacino, J. S., Davidson, M. W., Lippincott-Schwartz, J. and Hess, H. F. (2006). Imaging intracellular fluorescent proteins at nanometer resolution. Science *313*, 1642–1645.

Blackman, A. V., Grabuschnig, S., Legenstein, R. and Sjöström, P. J. (2014). A comparison of manual neuronal reconstruction from biocytin histology or 2-photon imaging: morphometry and computer modeling. Frontiers in Neuroanatomy *8*, 65.

Blaschke, M., Keller, B. U., Rivosecchi, R., Hollmann, M., Heinemann, S. and Konnerth, A. (1993). A single amino acid determines the subunit-specific spider toxin

block of alpha-amino-3-hydroxy-5-methylisoxazole-4-propionate/kainate receptor channels. Proceedings of the National Academy of Sciences of the United States of America *90*, 6528–6532.

Blatow, M., Caputi, A. and Monyer, H. (2005). Molecular diversity of neocortical GABAergic interneurones. Journal of Physiology *562*, 99–105.

Bliss, T. V., Collingridge, G. L. et al. (1993). A synaptic model of memory: long-term potentiation in the hippocampus. Nature *361*, 31–39.

Bliss, T. V. and Lomo, T. (1973). Long-lasting potentiation of synaptic transmission in the dentate area of the anaesthetized rabbit following stimulation of the perforant path. Journal of Physiology *232*, 331–356.

Borst, J. G., Helmchen, F. and Sakmann, B. (1995). Pre- and postsynaptic whole-cell recordings in the medial nucleus of the trapezoid body of the rat. Journal of Physiology *489*, 825–840.

Bortone, D. S., Olsen, S. R. and Scanziani, M. (2014). Translaminar inhibitory cells recruited by layer 6 corticothalamic neurons suppress visual cortex. Neuron *82*, 474–485.

Bourque, C. W. (2008). Central mechanisms of osmosensation and systemic osmoregulation. Nature Reviews. Neuroscience *9*, 519–531.

Bowie, D., Lange, G. D. and Mayer, M. L. (1998). Activity-dependent modulation of glutamate receptors by polyamines. Journal of Neuroscience *18*, 8175–8185.

Bowie, D. and Mayer, M. L. (1995). Inward rectification of both AMPA and kainate subtype glutamate receptors generated by polyamine-mediated ion channel block. Neuron *15*, 453–462.

Branco, T. and Häusser, M. (2011). Synaptic integration gradients in single cortical pyramidal cell dendrites. Neuron *69*, 885–892.

Briggman, K. L., Helmstaedter, M. and Denk, W. (2011). Wiring specificity in the direction-selectivity circuit of the retina. Nature *471*, 183–188.

Brown, K. M., Donohue, D. E., D'Alessandro, G. and Ascoli, G. A. (2005). A cross-platform freeware tool for digital reconstruction of neuronal arborizations from image stacks. Neuroinformatics *3*, 343–360.

Buchanan, K. A., Blackman, A. V., Moreau, A. W., Elgar, D., Costa, R. P., Lalanne, T., Tudor Jones, A. A., Oyrer, J. and Sjöström, P. J. (2012). Target-specific expression of presynaptic NMDA receptors in neocortical microcircuits. Neuron *75*, 451–466.

Burnashev, N., Schoepfer, R., Monyer, H., Ruppersberg, J. P., Gunther, W., Seeburg, P. H. and Sakmann, B. (1992). Control by asparagine residues of calcium permeability and magnesium blockade in the NMDA receptor. Science *257*, 1415–1419.

Burnashev, N., Zhou, Z., Neher, E. and Sakmann, B. (1995). Fractional calcium currents through recombinant GluR channels of the NMDA, AMPA and kainate receptor subtypes. Journal of Physiology *485*, 403–418.

Callaway, E. M. (2004). Feedforward, feedback and inhibitory connections in primate visual cortex. Neural Networks *17*, 625–632.

Cammalleri, M., Martini, D., Timperio, A. M. and Bagnoli, P. (2009). Functional effects of somatostatin receptor 1 activation on synaptic transmission in the mouse hippocampus. Journal of Neurochemistry *111*, 1466–1477.

Cardin, J. A., Carlén, M., Meletis, K., Knoblich, U., Zhang, F., Deisseroth, K., Tsai, L.-H. and Moore, C. I. (2009). Driving fast-spiking cells induces gamma rhythm and controls sensory responses. Nature *459*, 663–667.

Cauli, B., Audinat, E., Lambolez, B., Angulo, M. C., Ropert, N., Tsuzuki, K., Hestrin, S. and Rossier, J. (1997). Molecular and physiological diversity of cortical nonpyramidal cells. Journal of Neuroscience *17*, 3894–3906.

Cauli, B., Porter, J. T., Tsuzuki, K., Lambolez, B., Rossier, J., Quenet, B. and Audinat, E. (2000). Classification of fusiform neocortical interneurons based on unsupervised clustering. Proceedings of the National Academy of Sciences of the United States of America *97*, 6144–6149.

Chattopadhyaya, B., Di Cristo, G., Higashiyama, H., Knott, G. W., Kuhlman, S. J., Welker, E. and Huang, Z. J. (2004). Experience and activity-dependent maturation

of perisomatic GABAergic innervation in primary visual cortex during a postnatal critical period. Journal of Neuroscience *24*, 9598–9611.

Chen, L., Chetkovich, D. M., Petralia, R. S., Sweeney, N. T., Kawasaki, Y., Wenthold, R. J., Bredt, D. S. and Nicoll, R. A. (2000). Stargazin regulates synaptic targeting of AMPA receptors by two distinct mechanisms. Nature *408*, 936–943.

Clements, J. D. (1996). Transmitter timecourse in the synaptic cleft: its role in central synaptic function. Trends in Neurosciences *19*, 163–171.

Clements, J. D. and Bekkers, J. M. (1997). Detection of spontaneous synaptic events with an optimally scaled template. Biophysical Journal *73*, 220–229.

Collingridge, G., Kehl, S. and McLennan, H. t. (1983). Excitatory amino acids in synaptic transmission in the Schaffer collateral-commissural pathway of the rat hippocampus. Journal of Physiology *334*, 33–46.

Condé, F., Lund, J. S., Jacobowitz, D. M., Baimbridge, K. G. and Lewis, D. A. (1994). Local circuit neurons immunoreactive for calretinin, calbindin D-28k or parvalbumin in monkey prefrontal cortex: distribution and morphology. Journal of Comparative Neurology *341*, 95–116.

Constantinople, C. M. and Bruno, R. M. (2013). Deep cortical layers are activated directly by thalamus. Science *340*, 1591–1594.

Contractor, A., Mulle, C. and Swanson, G. T. (2011). Kainate receptors coming of age: milestones of two decades of research. Trends in Neurosciences *34*, 154–163.

Coombs, I. D., Soto, D., Zonouzi, M., Renzi, M., Shelley, C., Farrant, M. and Cull-Candy, S. G. (2012). Cornichons modify channel properties of recombinant and glial AMPA receptors. Journal of Neuroscience *32*, 9796–9804.

Corlew, R., Brasier, D. J., Feldman, D. E. and Philpot, B. D. (2008). Presynaptic NMDA receptors: newly appreciated roles in cortical synaptic function and plasticity. Neuroscientist *14*, 609–625.

Cox, D. J. and Racca, C. (2013). Differential dendritic targeting of AMPA receptor subunit mRNAs in adult rat hippocampal principal neurons and interneurons. Journal of Comparative Neurology *521*, 1954–2007.

Crasto, C. J. and Shepherd, G. M. (2007). Managing knowledge in neuroscience. Methods in Molecular Biology *401*, 3–21.

Cruikshank, S. J., Lewis, T. J. and Connors, B. W. (2007). Synaptic basis for intense thalamocortical activation of feedforward inhibitory cells in neocortex. Nature Neuroscience *10*, 462–468.

Cruikshank, S. J., Urabe, H., Nurmikko, A. V. and Connors, B. W. (2010). Pathway-specific feedforward circuits between thalamus and neocortex revealed by selective optical stimulation of axons. Neuron *65*, 230–245.

Cull-Candy, S., Kelly, L. and Farrant, M. (2006). Regulation of Ca^{2+}-permeable AMPA receptors: synaptic plasticity and beyond. Current Opinion in Neurobiology *16*, 288–297.

Dani, A., Huang, B., Bergan, J., Dulac, C. and Zhuang, X. (2010). Superresolution imaging of chemical synapses in the brain. Neuron *68*, 843–856.

DeFelipe, J. (1997). Types of neurons, synaptic connections and chemical characteristics of cells immunoreactive for calbindin-D28K, parvalbumin and calretinin in the neocortex. Journal of Chemical Neuroanatomy *14*, 1–19.

DeFelipe, J. (2002). Cortical interneurons: from Cajal to 2001. Progress in Brain Research *136*, 215–238.

DeFelipe, J., Alonso-Nanclares, L. and Arellano, J. I. (2002). Microstructure of the neocortex: comparative aspects. Journal of Neurocytology *31*, 299–316.

DeFelipe, J. and Fariñas, I. (1992). The pyramidal neuron of the cerebral cortex: morphological and chemical characteristics of the synaptic inputs. Progress in Neurobiology *39*, 563–607.

DeFelipe, J., López-Cruz, P. L., Benavides-Piccione, R., Bielza, C., Larrañaga, P., Anderson, S., Burkhalter, A., Cauli, B., Fairén, A., Feldmeyer, D., Fishell, G., Fitz-

patrick, D., Freund, T. F., González-Burgos, G., Hestrin, S., Hill, S., Hof, P. R., Huang, J., Jones, E. G., Kawaguchi, Y., Kisvárday, Z., Kubota, Y., Lewis, D. A., Marín, O., Markram, H., McBain, C. J., Meyer, H. S., Monyer, H., Nelson, S. B., Rockland, K., Rossier, J., Rubenstein, J. L. R., Rudy, B., Scanziani, M., Shepherd, G. M., Sherwood, C. C., Staiger, J. F., Tamás, G., Thomson, A., Wang, Y., Yuste, R. and Ascoli, G. A. (2013). New insights into the classification and nomenclature of cortical GABAergic interneurons. Nature Reviews. Neuroscience *14*, 202–216.

Deleuze, C., Pazienti, A. and Bacci, A. (2014). Autaptic self-inhibition of cortical GABAergic neurons: synaptic narcissism or useful introspection? Current Opinion in Neurobiology *26*, 64–71.

Demeulemeester, H., Arckens, L., Vandesande, F., Orban, G. A., Heizmann, C. W. and Pochet, R. (1991). Calcium binding proteins and neuropeptides as molecular markers of GABAergic interneurons in the cat visual cortex. Experimental Brain Research *84*, 538–544.

Denk, W., Delaney, K. R., Gelperin, A., Kleinfeld, D., Strowbridge, B. W., Tank, D. W. and Yuste, R. (1994). Anatomical and functional imaging of neurons using 2-photon laser scanning microscopy. Journal of Neuroscience Methods *54*, 151–162.

Denk, W., Strickler, J. H. and Webb, W. W. (1990). Two-photon laser scanning fluorescence microscopy. Science *248*, 73–76.

Denk, W. and Svoboda, K. (1997). Photon upmanship: why multiphoton imaging is more than a gimmick. Neuron *18*, 351–357.

Derkach, V., Barria, A. and Soderling, T. R. (1999). Ca^{2+}/calmodulin-kinase II enhances channel conductance of α-amino-3-hydroxy-5-methyl-4-isoxazolepropionate type glutamate receptors. Proceedings of the National Academy of Sciences of the United States of America *96*, 3269–3274.

Dingledine, R., Borges, K., Bowie, D. and Traynelis, S. F. (1999). The glutamate receptor ion channels. Pharmacological Reviews *51*, 7–62.

Dodt, H. U. and Zieglgänsberger, W. (1990). Visualizing unstained neurons in living brain slices by infrared DIC-videomicroscopy. Brain Research *537*, 333–336.

Donohue, D. E. and Ascoli, G. A. (2011). Automated reconstruction of neuronal morphology: an overview. Brain Research Reviews *67*, 94–102.

Douglas, R. J. and Martin, K. A. C. (2004). Neuronal circuits of the neocortex. Annual Review of Neuroscience *27*, 419–451.

Dugué, G. P., Dumoulin, A., Triller, A. and Dieudonné, S. (2005). Target-dependent use of co-released inhibitory transmitters at central synapses. Journal of Neuroscience *25*, 6490–6498.

Dumitriu, D., Cossart, R., Huang, J. and Yuste, R. (2007). Correlation between axonal morphologies and synaptic input kinetics of interneurons from mouse visual cortex. Cerebral Cortex *17*, 81–91.

Editors, E. J. N. (2011). Tips for immunohistochemistry.

Edwards, F. A., Konnerth, A., Sakmann, B. and Takahashi, T. (1989). A thin slice preparation for patch clamp recordings from neurones of the mammalian central nervous system. Pflugers Archiv (European Journal of Physiology) *414*, 600–612.

Farrant, M. and Kaila, K. (2007). The cellular, molecular and ionic basis of GABA(A) receptor signalling. Progress in Brain Research *160*, 59–87.

Fatt, P. and Katz, B. (1952). Spontaneous subthreshold activity at motor nerve endings. Journal of Physiology *117*, 109–128.

Feldmeyer, D. (2012). Excitatory neuronal connectivity in the barrel cortex. Frontiers in Neuroanatomy *6*, 24.

Ferreira, T. A., Blackman, A. V., Oyrer, J., Jayabal, S., Chung, A. J., Watt, A. J., Sjöström, P. J. and van Meyel, D. J. (2014). Neuronal morphometry directly from bitmap images. Nature Methods *11*, 982–984.

Fino, E. and Yuste, R. (2011). Dense inhibitory connectivity in neocortex. Neuron *69*, 1188–1203.

Fleming, J. J. and England, P. M. (2010). Developing a complete pharmacology for AMPA receptors: a perspective on subtype-selective ligands. Bioorganic & Medicinal Chemistry *18*, 1381–1387.

Fogarty, M., Grist, M., Gelman, D., Marín, O., Pachnis, V. and Kessaris, N. (2007). Spatial genetic patterning of the embryonic neuroepithelium generates GABAergic interneuron diversity in the adult cortex. Journal of Neuroscience *27*, 10935–10946.

Forsythe, I. D. (1994). Direct patch recording from identified presynaptic terminals mediating glutamatergic EPSCs in the rat CNS, in vitro. Journal of Physiology *479*, 381–387.

Frank, E. (1973). Matching of facilitation at the neuromuscular junction of the lobster: a possible case for influence of muscle on nerve. Journal of Physiology *233*, 635–658.

Fritschy, J.-M. (2008). Is my antibody-staining specific? How to deal with pitfalls of immunohistochemistry. European Journal of Neuroscience *28*, 2365–2370.

Fukaya, M., Tsujita, M., Yamazaki, M., Kushiya, E., Abe, M., Akashi, K., Natsume, R., Kano, M., Kamiya, H., Watanabe, M. and Sakimura, K. (2006). Abundant distribution of TARP gamma-8 in synaptic and extrasynaptic surface of hippocampal neurons and its major role in AMPA receptor expression on spines and dendrites. European Journal of Neuroscience *24*, 2177–2190.

Fukaya, M., Yamazaki, M., Sakimura, K. and Watanabe, M. (2005). Spatial diversity in gene expression for VDCC gamma subunit family in developing and adult mouse brains. Neuroscience Research *53*, 376–383.

Fukuda, T. and Kosaka, T. (2000). Gap junctions linking the dendritic network of GABAergic interneurons in the hippocampus. Journal of Neuroscience *20*, 1519–1528.

Gabbott, P. L. and Somogyi, P. (1986). Quantitative distribution of GABA-immunoreactive neurons in the visual cortex (area 17) of the cat. Experimental Brain Research *61*, 323–331.

Gabernet, L., Jadhav, S. P., Feldman, D. E., Carandini, M. and Scanziani, M. (2005). Somatosensory integration controlled by dynamic thalamocortical feed-forward inhibition. Neuron *48*, 315–327.

Galarreta, M. and Hestrin, S. (1999). A network of fast-spiking cells in the neocortex connected by electrical synapses. Nature *402*, 72–75.

Gardner, D., Akil, H., Ascoli, G. A., Bowden, D. M., Bug, W., Donohue, D. E., Goldberg, D. H., Grafstein, B., Grethe, J. S., Gupta, A. et al. (2008). The neuroscience information framework: a data and knowledge environment for neuroscience. Neuroinformatics *6*, 149–160.

Geiger, J. R. and Jonas, P. (2000). Dynamic control of presynaptic Ca^{2+} inflow by fast-inactivating K(+) channels in hippocampal mossy fiber boutons. Neuron *28*, 927–939.

Geiger, J. R., Lübke, J., Roth, A., Frotscher, M. and Jonas, P. (1997). Submillisecond AMPA receptor-mediated signaling at a principal neuron-interneuron synapse. Neuron *18*, 1009–1023.

Geiger, J. R., Melcher, T., Koh, D. S., Sakmann, B., Seeburg, P. H., Jonas, P. and Monyer, H. (1995). Relative abundance of subunit mRNAs determines gating and Ca^{2+} permeability of AMPA receptors in principal neurons and interneurons in rat CNS. Neuron *15*, 193–204.

Glaser, J. R. and Glaser, E. M. (1990). Neuron imaging with Neurolucida–a PC-based system for image combining microscopy. Computerized Medical Imaging and Graphics *14*, 307–317.

Glykys, J. and Mody, I. (2007). The main source of ambient GABA responsible for tonic inhibition in the mouse hippocampus. Journal of Physiology *582*, 1163–1178.

Goldberg, J. H., Lacefield, C. O. and Yuste, R. (2004). Global dendritic calcium spikes in mouse layer 5 low threshold spiking interneurones: implications for control of pyramidal cell bursting. Journal of Physiology *558*, 465–478.

Goldberg, J. H., Tamas, G., Aronov, D. and Yuste, R. (2003a). Calcium microdomains in aspiny dendrites. Neuron *40*, 807–821.

Goldberg, J. H., Tamas, G. and Yuste, R. (2003b). Ca^{2+} imaging of mouse neocortical interneurone dendrites: Ia-type K^+ channels control action potential backpropagation. Journal of Physiolgy *551*, 49–65.

Goldberg, J. H., Yuste, R. and Tamas, G. (2003c). Ca^{2+} imaging of mouse neocortical interneurone dendrites: contribution of Ca^{2+}-permeable AMPA and NMDA receptors to subthreshold Ca^{2+} dynamics. Journal of Physiology *551*, 67–78.

Gonchar, Y. and Burkhalter, A. (1997). Three distinct families of GABAergic neurons in rat visual cortex. Cerebral Cortex *7*, 347–358.

Gonchar, Y., Wang, Q. and Burkhalter, A. (2007). Multiple distinct subtypes of GABAergic neurons in mouse visual cortex identified by triple immunostaining. Frontiers in Neuroanatomy *1*, 3.

Greger, I. H., Khatri, L., Kong, X. and Ziff, E. B. (2003). AMPA receptor tetramerization is mediated by Q/R editing. Neuron *40*, 763–774.

Grillner, S., Markram, H., De Schutter, E., Silberberg, G. and LeBeau, F. E. N. (2005). Microcircuits in action–from CPGs to neocortex. Trends in Neurosciences *28*, 525–533.

Gulledge, A. T. and Stuart, G. J. (2003). Excitatory actions of GABA in the cortex. Neuron *37*, 299–309.

Gupta, A., Wang, Y. and Markram, H. (2000). Organizing principles for a diversity of GABAergic interneurons and synapses in the neocortex. Science *287*, 273–278.

Gustafsson, M. G. L. (2005). Nonlinear structured-illumination microscopy: wide-field fluorescence imaging with theoretically unlimited resolution. Proceedings of the National Academy of Sciences of the United States of America *102*, 13081–13086.

Halavi, M., Hamilton, K. A., Parekh, R. and Ascoli, G. A. (2012). Digital reconstructions of neuronal morphology: three decades of research trends. Frontiers in Neuroscience *6*, 49.

Hamad, M. I. K., Ma-Högemeier, Z.-L., Riedel, C., Conrads, C., Veitinger, T., Habijan, T., Schulz, J.-N., Krause, M., Wirth, M. J., Hollmann, M. and Wahle, P. (2011). Cell class-specific regulation of neocortical dendrite and spine growth by AMPA receptor splice and editing variants. Development *138*, 4301–4313.

Hamill, O. P., Marty, A., Neher, E., Sakmann, B. and Sigworth, F. J. (1981). Improved patch-clamp techniques for high-resolution current recording from cells and cell-free membrane patches. Pflugers Archiv (European Journal of Physiology) *391*, 85–100.

Harris, K. D. and Mrsic-Flogel, T. D. (2013). Cortical connectivity and sensory coding. Nature *503*, 51–58.

He, Y., Hof, P. R., Janssen, W. G., Vissavajjhala, P. and Morrison, J. H. (2001). AMPA GluR2 subunit is differentially distributed on GABAergic neurons and pyramidal cells in the macaque monkey visual cortex. Brain Research *921*, 60–67.

Helmstaedter, M., Sakmann, B. and Feldmeyer, D. (2009). Neuronal correlates of local, lateral, and translaminar inhibition with reference to cortical columns. Cerebral Cortex *19*, 926–937.

Hendry, S. H., Houser, C. R., Jones, E. G. and Vaughn, J. E. (1983). Synaptic organization of immunocytochemically identified GABA neurons in the monkey sensory-motor cortex. Journal of Neurocytology *12*, 639–660.

Hendry, S. H., Jones, E. G., Emson, P. C., Lawson, D. E., Heizmann, C. W. and Streit, P. (1989). Two classes of cortical GABA neurons defined by differential calcium binding protein immunoreactivities. Experimental Brain Research *76*, 467–472.

Hestrin, S. (1993). Different glutamate receptor channels mediate fast excitatory synaptic currents in inhibitory and excitatory cortical neurons. Neuron *11*, 1083–1091.

Hille, B. (2001). Ion Channels of Excitable Membranes. Sinauer Associates Inc.

Hof, P. R., Glezer, I. I., Condé, F., Flagg, R. A., Rubin, M. B., Nimchinsky, E. A. and Vogt Weisenhorn, D. M. (1999). Cellular distribution of the calcium-binding proteins parvalbumin, calbindin, and calretinin in the neocortex of mammals: phylogenetic and developmental patterns. Journal of Chemical Neuroanatomy *16*, 77–116.

Hofer, S. B., Ko, H., Pichler, B., Vogelstein, J., Ros, H., Zeng, H., Lein, E., Lesica, N. A. and Mrsic-Flogel, T. D. (2011). Differential connectivity and response dy-

namics of excitatory and inhibitory neurons in visual cortex. Nature Neuroscience *14*, 1045–1052.

Hofer, S. B., Mrsic-Flogel, T. D., Bonhoeffer, T. and Hübener, M. (2006). Lifelong learning: ocular dominance plasticity in mouse visual cortex. Current Opinion in Neurobiology *16*, 451–459.

Holderith, N., Lorincz, A., Katona, G., Rózsa, B., Kulik, A., Watanabe, M. and Nusser, Z. (2012). Release probability of hippocampal glutamatergic terminals scales with the size of the active zone. Nature Neuroscience *15*, 988–997.

Huang, L., Garcia, I., Jen, H.-I. and Arenkiel, B. R. (2013). Reciprocal connectivity between mitral cells and external plexiform layer interneurons in the mouse olfactory bulb. Frontiers in Neural Circuits *7*, 32.

Huang, S. and Uusisaari, M. Y. (2013). Physiological temperature during brain slicing enhances the quality of acute slice preparations. Frontier in Cellular Neuroscience *7*, 48.

Huang, Z., Di Cristo, G. and Ango, F. (2007). Development of GABA innervation in the cerebral and cerebellar cortices. Nature Reviews Neuroscience *8*, 673–686.

Hübener, M. (2003). Mouse visual cortex. Current Opinion in Neurobiology *13*, 413–420.

Huganir, R. L. and Nicoll, R. A. (2013). AMPARs and synaptic plasticity: the last 25 years. Neuron *80*, 704–717.

Hull, C., Isaacson, J. S. and Scanziani, M. (2009). Postsynaptic mechanisms govern the differential excitation of cortical neurons by thalamic inputs. Journal of Neuroscience *29*, 9127–9136.

Jackson, A. C., Milstein, A. D., Soto, D., Farrant, M., Cull-Candy, S. G. and Nicoll, R. A. (2011). Probing TARP modulation of AMPA receptor conductance with polyamine toxins. Journal of Neuroscience *31*, 7511–7520.

Jackson, A. C. and Nicoll, R. A. (2011). The expanding social network of ionotropic glutamate receptors: TARPs and other transmembrane auxiliary subunits. Neuron *70*, 178–199.

Jinno, S. and Kosaka, T. (2004). Parvalbumin is expressed in glutamatergic and GABAergic corticostriatal pathway in mice. Journal of Comparative Neurology *477*, 188–201.

Jonas, P. (2000). The time course of signalgnaling at central glutamatergic synapses. News in Physiological Sciences *15*, 83–89.

Jonas, P., Bischofberger, J., Fricker, D. and Miles, R. (2004). Interneuron Diversity series: Fast in, fast out–temporal and spatial signal processing in hippocampal interneurons. Trends in Neurosciences *27*, 30–40.

Jonas, P. and Burnashev, N. (1995). Molecular mechanisms controlling calcium entry through AMPA-type glutamate receptor channels. Neuron *15*, 987–990.

Jonas, P., Major, G. and Sakmann, B. (1993). Quantal components of unitary EPSCs at the mossy fibre synapse on CA3 pyramidal cells of rat hippocampus. Journal of Physiology *472*, 615–663.

Jonas, P., Racca, C., Sakmann, B., Seeburg, P. H. and Monyer, H. (1994). Differences in Ca^{2+} permeability of AMPA-type glutamate receptor channels in neocortical neurons caused by differential GluR-B subunit expression. Neuron *12*, 1281–1289.

Jonas, P. and Spruston, N. (1994). Mechanisms shaping glutamate-mediated excitatory postsynaptic currents in the CNS. Current Opinion in Neurobiology *4*, 366–372.

Jones, E. G. (1993). GABAergic neurons and their role in cortical plasticity in primates. Cerebral Cortex *3*, 361–372.

Kaeser, P. S. and Regehr, W. G. (2014). Molecular mechanisms for synchronous, asynchronous, and spontaneous neurotransmitter release. Annual Review of Physiology *76*, 333–363.

Kakegawa, W., Kohda, K. and Yuzaki, M. (2007). The delta2 ionotropic glutamate receptor functions as a non-ionotropic receptor to control cerebellar synaptic plasticity. The Journal of Physiology *584*, 89–96.

Kamboj, S. K., Swanson, G. T. and Cull-Candy, S. G. (1995). Intracellular spermine confers rectification on rat calcium-permeable AMPA and kainate receptors. Journal of Physiology *486*, 297–303.

Kapfer, C., Glickfeld, L. L., Atallah, B. V. and Scanziani, M. (2007). Supralinear increase of recurrent inhibition during sparse activity in the somatosensory cortex. Nature Neuroscience *10*, 743–753.

Karube, F., Kubota, Y. and Kawaguchi, Y. (2004). Axon branching and synaptic bouton phenotypes in GABAergic nonpyramidal cell subtypes. Journal of Neuroscience *24*, 2853–2865.

Kätzel, D., Zemelman, B. V., Buetfering, C., Wölfel, M. and Miesenböck, G. (2011). The columnar and laminar organization of inhibitory connections to neocortical excitatory cells. Nature Neuroscience *14*, 100–107.

Kawa, A., Stahlhut, M., Berezin, A., Bock, E. and Berezin, V. (1998). A simple procedure for morphometric analysis of processes and growth cones of neurons in culture using parameters derived from the contour and convex hull of the object. Journal of Neuroscience Methods *79*, 53–64.

Kawaguchi, Y., Karube, F. and Kubota, Y. (2006). Dendritic branch typing and spine expression patterns in cortical nonpyramidal cells. Cerebral Cortex *16*, 696–711.

Kawaguchi, Y. and Kubota, Y. (1996). Physiological and morphological identification of somatostatin- or vasoactive intestinal polypeptide-containing cells among GABAergic cell subtypes in rat frontal cortex. Journal of Neuroscience *16*, 2701–2715.

Kawaguchi, Y. and Kubota, Y. (1997). GABAergic cell subtypes and their synaptic connections in rat frontal cortex. Cerebral Cortex *7*, 476–486.

Kawaguchi, Y. and Kubota, Y. (1998). Neurochemical features and synaptic connections of large physiologically-identified GABAergic cells in the rat frontal cortex. Neuroscience *85*, 677–701.

Keinänen, K., Wisden, W., Sommer, B., Werner, P., Herb, A., Verdoorn, T. A., Sakmann, B. and Seeburg, P. H. (1990). A family of AMPA-selective glutamate receptors. Science *249*, 556–560.

Kessaris, N., Magno, L., Rubin, A. N. and Oliveira, M. G. (2014). Genetic programs controlling cortical interneuron fate. Current Opinion in Neurobiology *26*, 79–87.

Kisvárday, Z. F., Martin, K. A., Whitteridge, D. and Somogyi, P. (1985). Synaptic connections of intracellularly filled clutch cells: a type of small basket cell in the visual cortex of the cat. Journal of Comparative Neurology *241*, 111–137.

Klar, T. A. and Hell, S. W. (1999). Subdiffraction resolution in far-field fluorescence microscopy. Optics Letters *24*, 954–956.

Ko, H., Hofer, S. B., Pichler, B., Buchanan, K. A., Sjöström, P. J. and Mrsic-Flogel, T. D. (2011). Functional specificity of local synaptic connections in neocortical networks. Nature *473*, 87–91.

Kochubey, O., Lou, X. and Schneggenburger, R. (2011). Regulation of transmitter release by Ca^{2+} and synaptotagmin: insights from a large CNS synapse. Trends in Neurosciences *34*, 237–246.

Koh, D. S., Burnashev, N. and Jonas, P. (1995a). Block of native Ca^{2+}-permeable AMPA receptors in rat brain by intracellular polyamines generates double rectification. Journal of Physiology *486*, 305–312.

Koh, D. S., Geiger, J. R., Jonas, P. and Sakmann, B. (1995b). Ca^{2+}-permeable AMPA and NMDA receptor channels in basket cells of rat hippocampal dentate gyrus. Journal of Physiolgy *485*, 383–402.

Koike, M., Iino, M. and Ozawa, S. (1997). Blocking effect of 1-naphthyl acetyl spermine on Ca^{2+}-permeable AMPA receptors in cultured rat hippocampal neurons. Neuroscience Research *29*, 27–36.

Kooijmans, R. N., Self, M. W., Wouterlood, F. G., Beliën, J. A. M. and Roelfsema, P. R. (2014). Inhibitory interneuron classes express complementary AMPA-receptor patterns in macaque primary visual cortex. Journal of Neuroscience *34*, 6303–6315.

Kott, S., Sager, C., Tapken, D., Werner, M. and Hollmann, M. (2009). Comparative analysis of the pharmacology of GluR1 in complex with transmembrane AMPA receptor regulatory proteins $\gamma 2$, $\gamma 3$, $\gamma 4$, and $\gamma 8$. Neuroscience *158*, 78–88.

Kubota, Y., Hattori, R. and Yui, Y. (1994). Three distinct subpopulations of GABAergic neurons in rat frontal agranular cortex. Brain Research *649*, 159–173.

Kubota, Y., Karube, F., Nomura, M., Gulledge, A. T., Mochizuki, A., Schertel, A. and Kawaguchi, Y. (2011). Conserved properties of dendritic trees in four cortical interneuron subtypes. Scientific Reports *1*, 89.

Kudoh, S. N. and Taguchi, T. (2002). A simple exploratory algorithm for the accurate and fast detection of spontaneous synaptic events. Biosensors and Bioelectronics *17*, 773–782.

Kullmann, D. M. and Lamsa, K. P. (2007). Long-term synaptic plasticity in hippocampal interneurons. Nature Reviews. Neuroscience *8*, 687–699.

Kumar, S. S., Bacci, A., Kharazia, V. and Huguenard, J. R. (2002). A developmental switch of AMPA receptor subunits in neocortical pyramidal neurons. Journal of Neuroscience *22*, 3005–3015.

Lalanne, T., Oyrer, J., Costa, R. P., Chung, A. J., Farrant, M. and Sjostrom, P. J. (2014). Calcium-permeble AMPA receptors and synapse-specific plasticity in the neocortical layer-5 microcircuit. Proceedings of the Physiological Society *31*, PCB059.

Lambolez, B., Ropert, N., Perrais, D., Rossier, J. and Hestrin, S. (1996). Correlation between kinetics and RNA splicing of alpha-amino-3-hydroxy-5-methylisoxazole-4-propionic acid receptors in neocortical neurons. Proceedings of the National Academy of Sciences of the United States of America *93*, 1797–1802.

Lamsa, K., Heeroma, J. H. and Kullmann, D. M. (2005). Hebbian LTP in feed-forward inhibitory interneurons and the temporal fidelity of input discrimination. Nature Neuroscience *8*, 916–924.

Lamsa, K. P., Heeroma, J. H., Somogyi, P., Rusakov, D. A. and Kullmann, D. M. (2007). Anti-Hebbian long-term potentiation in the hippocampal feedback inhibitory circuit. Science *315*, 1262–1266.

Lamsa, K. P., Kullmann, D. M. and Woodin, M. A. (2010). Spike-timing dependent plasticity in inhibitory circuits. Frontiers in Synaptic Neuroscience *2*, 8.

Lee, S. H., Rosenmund, C., Schwaller, B. and Neher, E. (2000). Differences in Ca^{2+} buffering properties between excitatory and inhibitory hippocampal neurons from the rat. Journal of Physiology *525*, 405–418.

Lei, S. and McBain, C. J. (2002). Distinct NMDA receptors provide differential modes of transmission at mossy fiber-interneuron synapses. Neuron *33*, 921–933.

Lein, E. S., Hawrylycz, M. J., Ao, N., Ayres, M., Bensinger, A., Bernard, A., Boe, A. F., Boguski, M. S., Brockway, K. S., Byrnes, E. J. et al. (2006). Genome-wide atlas of gene expression in the adult mouse brain. Nature *445*, 168–176.

Leitch, B., Shevtsova, O. and Kerr, J. R. (2009). Selective reduction in synaptic proteins involved in vesicle docking and signalling at synapses in the ataxic mutant mouse stargazer. Journal of Comparative Neurology *512*, 52–73.

Lemmens, M. A. M., Steinbusch, H. W. M., Rutten, B. P. F. and Schmitz, C. (2010). Advanced microscopy techniques for quantitative analysis in neuromorphology and neuropathology research: current status and requirements for the future. Journal of Chemical Neuroanatomy *40*, 199–209.

León-Espinosa, G., DeFelipe, J. and Muñoz, A. (2012). Effects of amyloid-β plaque proximity on the axon initial segment of pyramidal cells. Journal of Alzheimer's Disease *29*, 841–852.

Lerma, J. (2006). Kainate receptor physiology. Current Opinion in Pharmacology *6*, 89–97.

Letts, V. A., Felix, R., Biddlecome, G. H., Arikkath, J., Mahaffey, C. L., Valenzuela, A., Bartlett, 2nd, F., Mori, Y., Campbell, K. P. and Frankel, W. N. (1998). The mouse stargazer gene encodes a neuronal Ca^{2+}-channel gamma subunit. Nature Genetics *19*, 340–347.

Lewis, D. A., Hashimoto, T. and Volk, D. W. (2005). Cortical inhibitory neurons and schizophrenia. Nature Reviews. Neuroscience *6*, 312–324.

Lisman, J. E. and Harris, K. M. (1993). Quantal analysis and synaptic anatomy–integrating two views of hippocampal plasticity. Trends in Neurosciences *16*, 141–147.

Lomeli, H., Mosbacher, J., Melcher, T., Hoger, T., Kuner, T., Monyer, H., Higuchi, M., Bach, A., Seeburg, P. et al. (1994). Control of kinetic properties of AMPA receptor channels by nuclear RNA editing. Science *266*, 1709–1713.

Lorincz, A. and Nusser, Z. (2008). Specificity of immunoreactions: the importance of testing specificity in each method. Journal of Neuroscience *28*, 9083–9086.

Lovett-Barron, M. and Losonczy, A. (2014). Behavioral consequences of GABAergic neuronal diversity. Current Opinion in Neurobiology *26*, 27–33.

Lu, J. (2011). Neuronal tracing for connectomic studies. Neuroinformatics *9*, 159–166.

Lu, J., Tucciarone, J., Lin, Y. and Huang, Z. J. (2014). Input-specific maturation of synaptic dynamics of parvalbumin interneurons in primary visual cortex. Proceedings of the National Academy of Sciences of the United States of America *111*, 16895–16900.

Lu, J.-t., Li, C.-y., Zhao, J.-P., Poo, M.-m. and Zhang, X.-h. (2007). Spike-timing-dependent plasticity of neocortical excitatory synapses on inhibitory interneurons depends on target cell type. Journal of Neuroscience *27*, 9711–9720.

Lüscher, C., Xia, H., Beattie, E. C., Carroll, R. C., von Zastrow, M., Malenka, R. C. and Nicoll, R. A. (1999). Role of AMPA receptor cycling in synaptic transmission and plasticity. Neuron *24*, 649–658.

Ma, Y., Hu, H., Berrebi, A. S., Mathers, P. H. and Agmon, A. (2006). Distinct subtypes of somatostatin-containing neocortical interneurons revealed in transgenic mice. Journal of Neuroscience *26*, 5069–5082.

MacVicar, B. A. and Dudek, F. E. (1980). Dye-coupling betwen CA3 pyramidal cells in slices of rat hippocampus. Brain Research *196*, 494–497.

Maheshwari, A., Nahm, W. K. and Noebels, J. L. (2013). Paradoxical proepileptic response to NMDA receptor blockade linked to cortical interneuron defect in stargazer mice. Frontiers in Cellular Neuroscience *7*, 156.

Markram, H. (2013). Seven challenges for neuroscience. Functional Neurology *28*, 145–151.

Markram, H., Lübke, J., Frotscher, M., Roth, A. and Sakmann, B. (1997a). Physiology and anatomy of synaptic connections between thick tufted pyramidal neurones in the developing rat neocortex. Journal of Physiology *500*, 409–440.

Markram, H., Lübke, J., Frotscher, M. and Sakmann, B. (1997b). Regulation of synaptic efficacy by coincidence of postsynaptic APs and EPSPs. Science *275*, 213–215.

Markram, H., Toledo-Rodriguez, M., Wang, Y., Gupta, A., Silberberg, G. and Wu, C. (2004). Interneurons of the neocortical inhibitory system. Nature Reviews. Neuroscience *5*, 793–807.

Markram, H., Wang, Y. and Tsodyks, M. (1998). Differential signaling via the same axon of neocortical pyramidal neurons. Proceedings of the National Academy of Sciences of the United States of America *95*, 5323–5328.

Martinotti, C. (1889). Contributo allo studio della corteccia cerebrale, ed all'origine central dei nervi. Ann Freniatr Sci Affini 1.

Massi, L., Lagler, M., Hartwich, K., Borhegyi, Z., Somogyi, P. and Klausberger, T. (2012). Temporal dynamics of parvalbumin-expressing axo-axonic and basket cells in the rat medial prefrontal cortex in vivo. Journal of Neuroscience *32*, 16496–16502.

Matta, J. A., Pelkey, K. A., Craig, M. T., Chittajallu, R., Jeffries, B. W. and McBain, C. J. (2013). Developmental origin dictates interneuron AMPA and NMDA receptor subunit composition and plasticity. Nature Neuroscience *16*, 1032–1041.

Mattison, H. A., Bagal, A. A., Mohammadi, M., Pulimood, N. S., Reich, C. G., Alger, B. E., Kao, J. P. Y. and Thompson, S. M. (2014). Evidence of calcium-permeable AMPA receptors in dendritic spines of CA1 pyramidal neurons. Journal of Neurophysiology *112*, 263–275.

Mayer, M. and Westbrook, G. (1987). Permeation and block of N-methyl-D-aspartic acid receptor channels by divalent cations in mouse cultured central neurones. Journal of Physiology *394*, 501–527.

McCormick, D. A., Connors, B. W., Lighthall, J. W. and Prince, D. A. (1985). Comparative electrophysiology of pyramidal and sparsely spiny stellate neurons of the neocortex. Journal of Neurophysiology *54*, 782–806.

McCormick, D. A. and Huguenard, J. R. (1992). A model of the electrophysiological properties of thalamocortical relay neurons. Journal of Neurophysiology *68*, PCB059.

McCormick, D. A. and Pape, H. C. (1990). Properties of a hyperpolarization-activated cation current and its role in rhythmic oscillation in thalamic relay neurones. Journal of Physiology *431*, 291–318.

McGarry, L. M., Packer, A. M., Fino, E., Nikolenko, V., Sippy, T. and Yuste, R. (2010). Quantitative classification of somatostatin-positive neocortical interneurons identifies three interneuron subtypes. Frontiers in Neural Circuits *4*, 12.

Meijering, E., Jacob, M., Sarria, J.-C. F., Steiner, P., Hirling, H. and Unser, M. (2004). Design and validation of a tool for neurite tracing and analysis in fluorescence microscopy images. Cytometry. Part A *58*, 167–176.

Meinecke, D. L. and Peters, A. (1987). GABA immunoreactive neurons in rat visual cortex. Journal of Comparative Neurology *261*, 388–404.

Menuz, K., O'Brien, J. L., Karmizadegan, S., Bredt, D. S. and Nicoll, R. A. (2008). TARP redundancy is critical for maintaining AMPA receptor function. Journal of Neuroscience *28*, 8740–8746.

Meyerson, J. R., Kumar, J., Chittori, S., Rao, P., Pierson, J., Bartesaghi, A., Mayer, M. L. and Subramaniam, S. (2014). Structural mechanism of glutamate receptor activation and desensitization. Nature *514*, 328–334.

Milenkovic, I., Vasiljevic, M., Maurer, D., Höger, H., Klausberger, T. and Sieghart, W. (2013). The parvalbumin-positive interneurons in the mouse dentate gyrus express $GABA_A$ receptor subunits alpha1, beta2, and delta along their extrasynaptic cell membrane. Neuroscience *254*, 80–96.

Moga, D., Hof, P. R., Vissavajjhala, P., Moran, T. M. and Morrison, J. H. (2002). Parvalbumin-containing interneurons in rat hippocampus have an AMPA receptor profile suggestive of vulnerability to excitotoxicity. Journal of Chemical Neuroanatomy *23*, 249–253.

Morris, R. G., Anderson, E., Lynch, G. S. and Baudry, M. (1986). Selective impairment of learning and blockade of long-term potentiation by an N-methyl-D-aspartate receptor antagonist, AP5. Nature *319*, 774–776.

Moyer, Jr, J. and Brown, T. H. (1998). Methods for whole-cell recording from visually preselected neurons of perirhinal cortex in brain slices from young and aging rats. Journal of Neuroscience Methods *86*, 35–54.

Myatt, D. R., Hadlington, T., Ascoli, G. A. and Nasuto, S. J. (2012). Neuromantic - from semi-manual to semi-automatic reconstruction of neuron morphology. Frontiers in Neuroinformatics *6*, 4.

Nair, D., Hosy, E., Petersen, J. D., Constals, A., Giannone, G., Choquet, D. and Sibarita, J.-B. (2013). Super-resolution imaging reveals that AMPA receptors inside synapses are dynamically organized in nanodomains regulated by PSD95. Journal of Neuroscience *33*, 13204–13224.

Nevian, T. (2003). Calcium dynamics in dendrites and spines of spiny neurons in the somatosensory barrel cortex of the rat. PhD thesis, Ruprecht-Karls-Universität Heidelberg.

Nicoll, R., Kauer, J. and Malenka, R. (1988). The current excitement in long term potentiation. Neuron *1*, 97–103.

Nicoll, R. A., Tomita, S. and Bredt, D. S. (2006). Auxiliary subunits assist AMPA-type glutamate receptors. Science *311*, 1253–1256.

Nissen, W., Szabo, A., Somogyi, J., Somogyi, P. and Lamsa, K. P. (2010). Cell type-specific long-term plasticity at glutamatergic synapses onto hippocampal interneurons expressing either parvalbumin or CB1 cannabinoid receptor. Journal of Neuroscience *30*, 1337–1347.

Noebels, J. L., Qiao, X., Bronson, R. T., Spencer, C. and Davisson, M. T. (1990). Stargazer: a new neurological mutant on chromosome 15 in the mouse with prolonged cortical seizures. Epilepsy Research *7*, 129–135.

Nowak, L., Bregestovski, P., Ascher, P., Herbet, A. and Prochiantz, A. (1984). Magnesium gates glutamate-activated channels in mouse central neurones. Nature *307*, 462–465.

Nusser, Z., Lujan, R., Laube, G., Roberts, J. D., Molnar, E. and Somogyi, P. (1998). Cell type and pathway dependence of synaptic AMPA receptor number and variability in the hippocampus. Neuron *21*, 545–559.

Oliva, Jr, A., Jiang, M., Lam, T., Smith, K. L. and Swann, J. W. (2000). Novel hippocampal interneuronal subtypes identified using transgenic mice that express green fluorescent protein in GABAergic interneurons. Journal of Neuroscience *20*, 3354–3368.

Oren, I., Nissen, W., Kullmann, D. M., Somogyi, P. and Lamsa, K. P. (2009). Role of ionotropic glutamate receptors in long-term potentiation in rat hippocampal CA1 oriens-lacunosum moleculare interneurons. Journal of Neuroscience *29*, 939–950.

Osswald, I. K., Galan, A. and Bowie, D. (2007). Light triggers expression of philanthotoxin-insensitive Ca^{2+}-permeable AMPA receptors in the developing rat retina. Journal of Physiology *582*, 95–111.

Otsuka, T. and Kawaguchi, Y. (2011). Cell diversity and connection specificity between callosal projection neurons in the frontal cortex. Journal of Neuroscience *31*, 3862–3870.

Overstreet, L. S., Kinney, G. A., Liu, Y. B., Billups, D. and Slater, N. T. (1999). Glutamate transporters contribute to the time course of synaptic transmission in cerebellar granule cells. Journal of Neuroscience *19*, 9663–9673.

Overstreet, L. S., Westbrook, G. L. and Jones, M. V. (2002). Measuring and modeling the spatiotemporal profile of GABA at the synapse,. Transmembrane Transporters, Quick, M W (Ed). Hoboken, NJ: Wiley-liss Inc.

Oyrer, J., Lalanne, T., Costa, R. P., Chung, A. J., Sjöström, P. J. and Farrant, M. (2013). Calcium-permeable AMPARs in local circuits of mouse visual cortex. Annual meeting of the Society for Neuroscience, San Diego CA. Nov., *9-13*, Poster 801.21/E3.

Packer, A. M. and Yuste, R. (2011). Dense, unspecific connectivity of neocortical parvalbumin-positive interneurons: a canonical microcircuit for inhibition? Journal of Neuroscience , *31*, 13260–13271.

Parekh, R. and Ascoli, G. A. (2013). Neuronal morphology goes digital: a research hub for cellular and system neuroscience. Neuron , *77*, 1017–1038.

Parra, P., Gulyás, A. I. and Miles, R. (1998). How many subtypes of inhibitory cells in the hippocampus? Neuron , *20*, 983–993.

Peled, E. S., Newman, Z. L. and Isacoff, E. Y. (2014). Evoked and spontaneous transmission favored by distinct sets of synapses. Current Biology , *24*, 484–493.

Perin, R., Berger, T. K. and Markram, H. (2011). A synaptic organizing principle for cortical neuronal groups. Proceedings of the National Academy of Sciences of the United States of America , *108*, 5419–5424.

Perrenoud, Q., Geoffroy, H., Gauthier, B., Rancillac, A., Alfonsi, F., Kessaris, N., Rossier, J., Vitalis, T. and Gallopin, T. (2012). Characterization of Type I and Type II nNOS-Expressing Interneurons in the Barrel Cortex of Mouse. Frontiers in Neural Circuits , *6*, 36.

Pesold, C., Liu, W. S., Guidotti, A., Costa, E. and Caruncho, H. J. (1999). Cortical bitufted, horizontal, and Martinotti cells preferentially express and secrete reelin into perineuronal nets, nonsynaptically modulating gene expression. Proceedings of the National Academy of Sciences of the United States of America , *96*, 3217–3222.

Petralia, R. S. and Wenthold, R. J. (1992). Light and electron immunocytochemical localization of AMPA-selective glutamate receptors in the rat brain. Journal of Comparative Neurology , *318*, 329–354.

Petreanu, L., Mao, T., Sternson, S. M. and Svoboda, K. (2009). The subcellular organization of neocortical excitatory connections. Nature , *457*, 1142–1145.

Pfeffer, C. K., Xue, M., He, M., Huang, Z. J. and Scanziani, M. (2013). Inhibition of inhibition in visual cortex: the logic of connections between molecularly distinct interneurons. Nature Neuroscience , *16*, 1068–1076.

Pi, H.-J., Hangya, B., Kvitsiani, D., Sanders, J. I., Huang, Z. J. and Kepecs, A. (2013). Cortical interneurons that specialize in disinhibitory control. Nature , *503*, 521–524.

Plant, K., Pelkey, K. A., Bortolotto, Z. A., Morita, D., Terashima, A., McBain, C. J., Collingridge, G. L. and Isaac, J. T. (2006). Transient incorporation of native GluR2-lacking AMPA receptors during hippocampal long-term potentiation. Nature Neuroscience , *9*, 602–604.

Pologruto, T. A., Sabatini, B. L. and Svoboda, K. (2003). ScanImage: flexible software for operating laser scanning microscopes. Biomedical Engineering Online , *2*, 13.

Pouille, F. and Scanziani, M. (2004). Routing of spike series by dynamic circuits in the hippocampus. Nature , *429*, 717–723.

Priel, A., Kolleker, A., Ayalon, G., Gillor, M., Osten, P. and Stern-Bach, Y. (2005). Stargazin reduces desensitization and slows deactivation of the AMPA-type glutamate receptors. Journal of Neuroscience , *25*, 2682–2686.

Purgianto, A., Scheyer, A. F., Loweth, J. A., Ford, K. A., Tseng, K. Y. and Wolf, M. E. (2013). Different adaptations in AMPA receptor transmission in the nucleus accumbens after short vs long access cocaine self-administration regimens. Neuropsychopharmacology , *38*, 1789–1797.

Qiao, X., Hefti, F., Knusel, B. and Noebels, J. L. (1996). Selective failure of brain-derived neurotrophic factor mRNA expression in the cerebellum of stargazer, a mutant mouse with ataxia. Journal of Neuroscience , *16*, 640–648.

Ramon y Cajal, S. (1911). Histologie de systeme nerveux de 1 Homme et des vertebres tomme II. Paris: Maloine.

Rhodes, K. J. and Trimmer, J. S. (2006). Antibodies as valuable neuroscience research tools versus reagents of mass distraction. Journal of Neuroscience *26*, 8017–8020.

Rice, M. E., Pérez-Pinzón, M. A. and Lee, E. J. (1994). Ascorbic acid, but not glutathione, is taken up by brain slices and preserves cell morphology. Journal of Neurophysiology *71*, 1591–1596.

Richardson, C. A. and Leitch, B. (2005). Phenotype of cerebellar glutamatergic neurons is altered in stargazer mutant mice lacking brain-derived neurotrophic factor mRNA expression. Journal of Comparative Neurology *481*, 145–159.

Rossi, B., Maton, G. and Collin, T. (2008). Calcium-permeable presynaptic AMPA receptors in cerebellar molecular layer interneurones. Journal of Physiology *586*, 5129–5145.

Rossignol, E., Kruglikov, I., van den Maagdenberg, A. M. J. M., Rudy, B. and Fishell, G. (2013). CaV 2.1 ablation in cortical interneurons selectively impairs fast-spiking basket cells and causes generalized seizures. Annals of Neurology *74*, 209–222.

Rozov, A. and Burnashev, N. (1999). Polyamine-dependent facilitation of postsynaptic AMPA receptors counteracts paired-pulse depression. Nature *401*, 594–598.

Rozov, A., Sprengel, R. and Seeburg, P. H. (2012). GluA2-lacking AMPA receptors in hippocampal CA1 cell synapses: evidence from gene-targeted mice. Frontiers in Molecular Neuroscience *5*, 22.

Rozov, A., Zilberter, Y., Wollmuth, L. P. and Burnashev, N. (1998). Facilitation of currents through rat Ca^{2+}-permeable AMPA receptor channels by activity-dependent relief from polyamine block. Journal of Physiology *511*, 361–377.

Runyan, C. A., Schummers, J., Van Wart, A., Kuhlman, S. J., Wilson, N. R., Huang, Z. J. and Sur, M. (2010). Response features of parvalbumin-expressing interneurons suggest precise roles for subtypes of inhibition in visual cortex. Neuron *67*, 847–857.

Rusakov, D. A., Savtchenko, L. P., Zheng, K. and Henley, J. M. (2011). Shaping the synaptic signal: molecular mobility inside and outside the cleft. Trends in Neurosciences *34*, 359–369.

Rust, M. J., Bates, M. and Zhuang, X. (2006). Sub-diffraction-limit imaging by stochastic optical reconstruction microscopy (STORM). Nature Methods *3*, 793–795.

Salussolia, C. L. and Wollmuth, L. P. (2012). Flip-flopping to the membrane. Neuron *76*, 463–465.

Sara, Y., Bal, M., Adachi, M., Monteggia, L. M. and Kavalali, E. T. (2011). Use-dependent AMPA receptor block reveals segregation of spontaneous and evoked glutamatergic neurotransmission. Journal of Neuroscience *31*, 5378–5382.

Scanziani, M., Gähwiler, B. H. and Charpak, S. (1998). Target cell-specific modulation of transmitter release at terminals from a single axon. Proceedings of the National Academy of Sciences of the United States of America *95*, 12004–12009.

Scheuss, V. and Bonhoeffer, T. (2014). Function of dendritic spines on hippocampal inhibitory neurons. Cerebral Cortex *24*, 3142–3153.

Schindelin, J., Arganda-Carreras, I., Frise, E., Kaynig, V., Longair, M., Pietzsch, T., Preibisch, S., Rueden, C., Saalfeld, S., Schmid, B., Tinevez, J.-Y., White, D. J., Hartenstein, V., Eliceiri, K., Tomancak, P. and Cardona, A. (2012). Fiji: an open-source platform for biological-image analysis. Nature Methods *9*, 676–682.

Schneggenburger, R. (1996). Simultaneous measurement of Ca^{2+} influx and reversal potentials in recombinant N-methyl-D-aspartate receptor channels. Biophysical Journal *70*, 2165–2174.

Schwenk, J., Baehrens, D., Haupt, A., Bildl, W., Boudkkazi, S., Roeper, J., Fakler, B. and Schulte, U. (2014). Regional Diversity and Developmental Dynamics of the AMPA-Receptor Proteome in the Mammalian Brain. Neuron *84*, 41–54.

Schwenk, J., Harmel, N., Brechet, A., Zolles, G., Berkefeld, H., Müller, C. S., Bildl, W., Baehrens, D., Hüber, B., Kulik, A. et al. (2012). High-resolution proteomics

unravel architecture and molecular diversity of native AMPA receptor complexes. Neuron *74*, 621–633.

Schwenk, J., Harmel, N., Zolles, G., Bildl, W., Kulik, A., Heimrich, B., Chisaka, O., Jonas, P., Schulte, U., Fakler, B. et al. (2009). Functional proteomics identify cornichon proteins as auxiliary subunits of AMPA receptors. Science *323*, 1313–1319.

Shanks, N. F., Savas, J. N., Maruo, T., Cais, O., Hirao, A., Oe, S., Ghosh, A., Noda, Y., Greger, I. H., Yates Iii, J. R. et al. (2012). Differences in AMPA and kainate receptor interactomes facilitate identification of AMPA receptor auxiliary subunit GSG1L. Cell reports *1*, 590–598.

Shigemoto, R., Kulik, A., Roberts, J. D., Ohishi, H., Nusser, Z., Kaneko, T. and Somogyi, P. (1996). Target-cell-specific concentration of a metabotropic glutamate receptor in the presynaptic active zone. Nature *381*, 523–525.

Shimuta, M., Yoshikawa, M., Fukaya, M., Watanabe, M., Takeshima, H. and Manabe, T. (2001). Postsynaptic modulation of AMPA receptor-mediated synaptic responses and LTP by the type 3 ryanodine receptor. Molecular and Cellular Neurosciences *17*, 921–930.

Shin, J., Shen, F. and Huguenard, J. R. (2005). Polyamines modulate AMPA receptor-dependent synaptic responses in immature layer v pyramidal neurons. Journal of Neurophysiology *93*, 2634–2643.

Sholl, D. A. (1953). Dendritic organization in the neurons of the visual and motor cortices of the cat. Journal of Anatomy *87*, 387–406.

Silberberg, G., Grillner, S., LeBeau, F. E. N., Maex, R. and Markram, H. (2005). Synaptic pathways in neural microcircuits. Trends in Neurosciences *28*, 541–551.

Silberberg, G. and Markram, H. (2007). Disynaptic inhibition between neocortical pyramidal cells mediated by Martinotti cells. Neuron *53*, 735–746.

Silver, R. A., Traynelis, S. F. and Cull-Candy, S. G. (1992). Rapid-time-course miniature and evoked excitatory currents at cerebellar synapses in situ. Nature *355*, 163–166.

Sjöström, P. J. and Nelson, S. B. (2002). Spike timing, calcium signals and synaptic plasticity. Current Opinion in Neurobiology *12*, 305–314.

Sjöström, P. J., Rancz, E. A., Roth, A. and Häusser, M. (2008). Dendritic excitability and synaptic plasticity. Physiological Reviews *88*, 769–840.

Sjöström, P. J., Turrigiano, G. G. and Nelson, S. B. (2001). Rate, timing, and cooperativity jointly determine cortical synaptic plasticity. Neuron *32*, 1149–1164.

Smart, T. G. and Paoletti, P. (2012). Synaptic neurotransmitter-gated receptors. Cold Spring Harbor Perspectives in Biology *4*, a009662.

Sobolevsky, A. I., Rosconi, M. P. and Gouaux, E. (2009). X-ray structure, symmetry and mechanism of an AMPA-subtype glutamate receptor. Nature *462*, 745–756.

Sommeijer, J.-P. and Levelt, C. N. (2012). Synaptotagmin-2 is a reliable marker for parvalbumin positive inhibitory boutons in the mouse visual cortex. PLoS One *7*, e35323.

Sommer, B., Köhler, M., Sprengel, R. and Seeburg, P. H. (1991). RNA editing in brain controls a determinant of ion flow in glutamate-gated channels. Cell *67*, 11–19.

Somogyi, P., Kisvárday, Z. F., Martin, K. A. and Whitteridge, D. (1983). Synaptic connections of morphologically identified and physiologically characterized large basket cells in the striate cortex of cat. Neuroscience *10*, 261–294.

Somogyi, P., Tamás, G., Lujan, R. and Buhl, E. H. (1998). Salient features of synaptic organisation in the cerebral cortex. Brain Research. Brain Research Reviews *26*, 113–135.

Song, S., Sjöström, P. J., Reigl, M., Nelson, S. and Chklovskii, D. B. (2005). Highly nonrandom features of synaptic connectivity in local cortical circuits. PLoS Biol *3*, e68.

Soto, D., Coombs, I. D., Kelly, L., Farrant, M. and Cull-Candy, S. G. (2007). Stargazin attenuates intracellular polyamine block of calcium-permeable AMPA receptors. Nature Neuroscience *10*, 1260–1267.

Spruston, N. (2008). Pyramidal neurons: dendritic structure and synaptic integration. Nature Reviews. Neuroscience *9*, 206–221.

Spruston, N., Jaffe, D. B., Williams, S. H. and Johnston, D. (1993). Voltage- and space-clamp errors associated with the measurement of electrotonically remote synaptic events. Journal of Neurophysiology *70*, 781–802.

Spruston, N. and Johnston, D. (2008). Out of control in the dendrites. Nature Neuroscience *11*, 733–734.

Spruston, N., Jonas, P. and Sakmann, B. (1995). Dendritic glutamate receptor channels in rat hippocampal CA3 and CA1 pyramidal neurons. Journal of Physiology *482*, 325–352.

Straub, C. and Tomita, S. (2012). The regulation of glutamate receptor trafficking and function by TARPs and other transmembrane auxiliary subunits. Current Opinion in Neurobiology *22*, 488–495.

Strømgaard, K. and Mellor, I. (2004). AMPA receptor ligands: synthetic and pharmacological studies of polyamines and polyamine toxins. Medicinal Research Reviews *24*, 589–620.

Stuart, G. J., Dodt, H. U. and Sakmann, B. (1993). Patch-clamp recordings from the soma and dendrites of neurons in brain slices using infrared video microscopy. Pflugers Archiv (European Journal of Physiology) *423*, 511–518.

Studniarczyk, D., Coombs, I., Cull-Candy, S. G. and Farrant, M. (2013). TARP γ-7 selectively enhances synaptic expression of calcium-permeable AMPARs. Nature Neuroscience *16*, 1266–1274.

Suchyna, T. M., Markin, V. S. and Sachs, F. (2009). Biophysics and structure of the patch and the gigaseal. Biophysical Journal *97*, 738–747.

Sukumaran, M., Penn, A. C. and Greger, I. H. (2012). AMPA receptor assembly: atomic determinants and built-in modulators. In Synaptic Plasticity pp. 241–264. Springer.

Sutton, M. A. and Schuman, E. M. (2009). Partitioning the synaptic landscape: distinct microdomains for spontaneous and spike-triggered neurotransmission. Science Signaling *2*, pe19.

Swanson, G. T., Kamboj, S. K. and Cull-Candy, S. G. (1997). Single-channel properties of recombinant AMPA receptors depend on RNA editing, splice variation, and subunit composition. Journal of Neuroscience *17*, 58–69.

Szabo, A., Somogyi, J., Cauli, B., Lambolez, B., Somogyi, P. and Lamsa, K. P. (2012). Calcium-permeable AMPA receptors provide a common mechanism for LTP in glutamatergic synapses of distinct hippocampal interneuron types. Journal of Neuroscience *32*, 6511–6516.

Takumi, Y., Ramírez-León, V., Laake, P., Rinvik, E. and Ottersen, O. P. (1999). Different modes of expression of AMPA and NMDA receptors in hippocampal synapses. Nature neuroscience *2*, 618–624.

Tanaka, Y., Tanaka, Y., Furuta, T., Yanagawa, Y. and Kaneko, T. (2008). The effects of cutting solutions on the viability of GABAergic interneurons in cerebral cortical slices of adult mice. Journal of Neuroscience Methods *171*, 118–125.

Taniguchi, H., Lu, J. and Huang, Z. J. (2013). The spatial and temporal origin of chandelier cells in mouse neocortex. Science *339*, 70–74.

Tao, Y., Chen, Y.-J., Shen, C., Luo, Z., Bates, C. R., Lee, D., Marchetto, S., Gao, T.-M., Borg, J.-P., Xiong, W.-C. and Mei, L. (2013). Erbin interacts with TARP γ-2 for surface expression of AMPA receptors in cortical interneurons. Nature Neuroscience *16*, 290–299.

Tarusawa, E., Matsui, K., Budisantoso, T., Molnár, E., Watanabe, M., Matsui, M., Fukazawa, Y. and Shigemoto, R. (2009). Input-specific intrasynaptic arrangements of ionotropic glutamate receptors and their impact on postsynaptic responses. Journal of Neuroscience *29*, 12896–12908.

Thomson, A. M. (1997). Activity-dependent properties of synaptic transmission at two classes of connections made by rat neocortical pyramidal axons in vitro. Journal of Physiology *502*, 131–147.

Thomson, A. M., Deuchars, J. and West, D. C. (1993). Large, deep layer pyramid-pyramid single axon EPSPs in slices of rat motor cortex display paired pulse and frequency-dependent depression, mediated presynaptically and self-facilitation, mediated postsynaptically. Journal of Neurophysiology *70*, 2354–2369.

Thomson, A. M. and Lamy, C. (2007). Functional maps of neocortical local circuitry. Frontiers in Neuroscience *1*, 19–42.

Toledo-Rodriguez, M., Blumenfeld, B., Wu, C., Luo, J., Attali, B., Goodman, P. and Markram, H. (2004). Correlation maps allow neuronal electrical properties to be predicted from single-cell gene expression profiles in rat neocortex. Cerebral Cortex *14*, 1310–1327.

Toledo-Rodriguez, M., Goodman, P., Illic, M., Wu, C. and Markram, H. (2005). Neuropeptide and calcium-binding protein gene expression profiles predict neuronal anatomical type in the juvenile rat. Journal of Physiology *567*, 401–413.

Tölle, T. R., Berthele, A., Zieglgänsberger, W., Seeburg, P. H. and Wisden, W. (1993). The differential expression of 16 NMDA and non-NMDA receptor subunits in the rat spinal cord and in periaqueductal gray. Journal of Neuroscience *13*, 5009–5028.

Tomita, S., Adesnik, H., Sekiguchi, M., Zhang, W., Wada, K., Howe, J. R., Nicoll, R. A. and Bredt, D. S. (2005). Stargazin modulates AMPA receptor gating and trafficking by distinct domains. Nature *435*, 1052–1058.

Tomita, S., Fukata, M., Nicoll, R. A. and Bredt, D. S. (2004). Dynamic interaction of stargazin-like TARPs with cycling AMPA receptors at synapses. Science *303*, 1508–1511.

Tóth, K. and McBain, C. J. (1998). Afferent-specific innervation of two distinct AMPA receptor subtypes on single hippocampal interneurons. Nature Neuroscience *1*, 572–578.

Tóth, K. and McBain, C. J. (2000). Target-specific expression of pre- and postsynaptic mechanisms. Journal of Physiology *525*, 41–51.

Traub, R. D., Jefferys, J. G. and Whittington, M. A. (1997). Simulation of gamma rhythms in networks of interneurons and pyramidal cells. Journal of Computational Neuroscience *4*, 141–150.

Traub, R. D., Whittington, M. A., Stanford, I. M. and Jefferys, J. G. (1996). A mechanism for generation of long-range synchronous fast oscillations in the cortex. Nature *383*, 621–624.

Traynelis, S. F., Wollmuth, L. P., McBain, C. J., Menniti, F. S., Vance, K. M., Ogden, K. K., Hansen, K. B., Yuan, H., Myers, S. J. and Dingledine, R. (2010). Glutamate receptor ion channels: structure, regulation, and function. Pharmacological Reviews *62*, 405–496.

Tsai, P. and Kleinfeld, D. (2009). In Vivo Two-Photon Laser Scanning Microscopy with Concurrent Plasma-Mediated Ablation Principles and Hardware Realization chapter 3, pp. 59–115. Boca Raton (FL): CRC Press.

Tsiola, A., Hamzei-Sichani, F., Peterlin, Z. and Yuste, R. (2003). Quantitative morphologic classification of layer 5 neurons from mouse primary visual cortex. Journal of Comparative Neurology , *461*, 415–428.

Tsodyks, M. V. and Markram, H. (1997). The neural code between neocortical pyramidal neurons depends on neurotransmitter release probability. Proceedings of the National Academy of Sciences of the United States of America , *94*, 719–723.

Vissavajjhala, P., Janssen, W. G., Hu, Y., Gazzaley, A. H., Moran, T., Hof, P. R. and Morrison, J. H. (1996). Synaptic distribution of the AMPA-GluR2 subunit and its colocalization with calcium-binding proteins in rat cerebral cortex: an immunohistochemical study using a GluR2-specific monoclonal antibody. Experimental Neurology , *142*, 296–312.

Von Engelhardt, J., Mack, V., Sprengel, R., Kavenstock, N., Li, K. W., Stern-Bach, Y., Smit, A. B., Seeburg, P. H. and Monyer, H. (2010). CKAMP44: a brain-specific protein attenuating short-term synaptic plasticity in the dentate gyrus. Science , *327*, 1518–1522.

Wahle, P. (1993). Differential regulation of substance P and somatostatin in Martinotti cells of the developing cat visual cortex. Journal of Comparative Neurology , *329*, 519–538.

Wang, H.-X. and Gao, W.-J. (2010). Development of calcium-permeable AMPA receptors and their correlation with NMDA receptors in fast-spiking interneurons of rat prefrontal cortex. Journal of Physiology , *588*, 2823–2838.

Wang, Y., Gupta, A., Toledo-Rodriguez, M., Wu, C. Z. and Markram, H. (2002). Anatomical, physiological, molecular and circuit properties of nest basket cells in the developing somatosensory cortex. Cerebral Cortex , *12*, 395–410.

Wang, Y., Toledo-Rodriguez, M., Gupta, A., Wu, C., Silberberg, G., Luo, J. and Markram, H. (2004). Anatomical, physiological and molecular properties of Martinotti cells in the somatosensory cortex of the juvenile rat. Journal of Physiology , *561*, 65–90.

Washburn, M. S. and Dingledine, R. (1996). Block of alpha-amino-3-hydroxy-5-methyl-4-isoxazolepropionic acid (AMPA) receptors by polyamines and polyamine toxins. Journal of Pharmacology and Experimental Therapeutics , *278*, 669–678.

Washburn, M. S., Numberger, M., Zhang, S. and Dingledine, R. (1997). Differential dependence on GluR2 expression of three characteristic features of AMPA receptors. Journal of Neuroscience , *17*, 9393–9406.

Williams, S. R. and Mitchell, S. J. (2008). Direct measurement of somatic voltage clamp errors in central neurons. Nature Neuroscience , *11*, 790–798.

Winterer, J., Stempel, A. V., Dugladze, T., Földy, C., Maziashvili, N., Zivkovic, A. R., Priller, J., Soltesz, I., Gloveli, T. and Schmitz, D. (2011). Cell-type-specific modulation of feedback inhibition by serotonin in the hippocampus. Journal of Neuroscience , *31*, 8464–8475.

Wonders, C. P. and Anderson, S. A. (2006). The origin and specification of cortical interneurons. Nature Reviews. Neuroscience , *7*, 687–696.

Wonders, C. P., Taylor, L., Welagen, J., Mbata, I. C., Xiang, J. Z. and Anderson, S. A. (2008). A spatial bias for the origins of interneuron subgroups within the medial ganglionic eminence. Developments in Biologicals , *314*, 127–136.

Woodruff, A., Xu, Q., Anderson, S. A. and Yuste, R. (2009). Depolarizing effect of neocortical chandelier neurons. Frontiers in Neural Circuits , *3*, 15.

Xu, X., Roby, K. D. and Callaway, E. M. (2006). Mouse cortical inhibitory neuron type that coexpresses somatostatin and calretinin. Journal of Comparative Neurology , *499*, 144–160.

Xu, X., Roby, K. D. and Callaway, E. M. (2010). Immunochemical characterization of inhibitory mouse cortical neurons: three chemically distinct classes of inhibitory cells. Journal of Comparative Neurology , *518*, 389–404.

Ye, J. H., Zhang, J., Xiao, C. and Kong, J.-Q. (2006). Patch-clamp studies in the CNS illustrate a simple new method for obtaining viable neurons in rat brain slices: glycerol replacement of NaCl protects CNS neurons. Journal of Neuroscience Methods , *158*, 251–259.

Yoshimura, Y. and Callaway, E. M. (2005). Fine-scale specificity of cortical networks depends on inhibitory cell type and connectivity. Nature Neuroscience , *8*, 1552–1559.

Yoshimura, Y., Dantzker, J. L. M. and Callaway, E. M. (2005). Excitatory cortical neurons form fine-scale functional networks. Nature , *433*, 868–873.

Zhao, S., Ting, J. T., Atallah, H. E., Qiu, L., Tan, J., Gloss, B., Augustine, G. J., Deisseroth, K., Luo, M., Graybiel, A. M. and Feng, G. (2011). Cell type–specific channelrhodopsin-2 transgenic mice for optogenetic dissection of neural circuitry function. Nature Methods , *8*, 745–752.

Zhou, F. M. and Hablitz, J. J. (1997). Rapid kinetics and inward rectification of miniature EPSCs in layer I neurons of rat neocortex. Journal of Neurophysiology , *77*, 2416–2426.

Zucker, R. S. and Regehr, W. G. (2002). Short-term synaptic plasticity. Annual Review of Physiology , *64*, 355–405.